2021

GENERATION, CHARACTERIZATION, AND C-H BOND ACTIVATION REACTIVITY BY MONONUCLEAR HIGH-VALENT COBALT(IV) AND NICKEL(IV) NON-OXO COMPLEXES

Yubin Maria Kwon

GENERATION, CHARACTERIZATION, AND C-H BOND ACTIVATION REACTIVITY BY MONONUCLEAR

HIGH-VALENT COBALT(IV) AND NICKEL(IV) NON-OXO COMPLEXES

By

YUBIN MARIA KWON

Bachelor of Science in Chemistry, Western Washington University, Bellingham, Washington, 2013
Master of Science in Chemistry, Western Washington University, Bellingham, Washington, 2016

Dissertation

presented in partial fulfillment of the requirements
for the degree of

Doctor of Philosophy
in Bioinorganic Chemistry

The University of Montana
Missoula, MT

December 2021

Approved by:
Scott Whittenburg, Ph.D., Dean of The Graduate School
Graduate School

Dong Wang, Ph. D., Advisor
Department of Chemistry and Biochemistry

Orion B. Berryman, Ph.D.
Department of Chemistry and Biochemistry

Bruce E. Bowler, Ph.D.
Department of Chemistry and Biochemistry

Christopher P. Palmer, Ph.D.
Department of Chemistry and Biochemistry

Stephen R. Sprang, Ph.D.
Division of Biological Sciences

Edward Rosenberg, Ph.D.
Department of Chemistry and Biochemistry

Kwon, Yubin, Ph.D., December 2021   Bioinorganic Chemistry

GENERATION, CHARACTERIZATION, AND C-H BOND ACTIVATION REACTIVITY BY MONONUCLEAR HIGH-VALENT COBALT(IV) AND NICKEL(IV) NON-OXO COMPLEXES

Advisor: Dong Wang

Chairperson: Bruce E. Bowler

Abstract

The study of terminal high-valent transition metal-oxo complexes has increased significantly over the years as it is believed that they are key reactive intermediates for a wide range of biological and industrial catalytic processes. These complexes are powerful oxidants for the activation of strong C-H bonds. The chemical and physical properties of these complexes remain elusive. It is therefore desirable to study the properties and function of these complexes through synthetic models. There have been many efforts and reports of synthetic high-valent metal-oxo complexes of early and middle transition metals (up to group 8 on the Periodic Table of Elements), but as we go beyond group 9, the generation of stable high-valent metal oxo complexes for these transition metals is challenging synthetically. This phenomenon is referred to as the "oxo-wall." There have been many efforts to break this "oxo-wall" and remains intact to this date. The focus of this research is to study a series of mononuclear cobalt and nickel complexes with oxidation states of +2, +3, and +4. These complexes are supported by a di-anionic, tridentate ligand system and were characterized using various spectroscopic methods such as X-ray crystallography, NMR, EPR, UV-Vis, and DFT computational methods. The generated complexes with an oxidation state of +4 can cleave strong sp^3 C-H bonds. This work will inspire to generate more reactive high-valent late transition metal-oxo and non-oxo complexes and understand C-H bond activation in high-valent metal chemistry.

Chapter 1 provides a background of synthetic chemistry, generation of high-valent metal-oxo complexes, and the "oxo-wall" theory. Chapter 2 describes the work of the early stages and development of this project leading to how we got to the point in our research currently. Chapter 3 examines and describes the generation, characterization, and reactivity studies of a novel Co(IV)-dinitrate complex. As well as providing preliminary data of a more reactive Co(IV) species. Chapter 4 introduces going beyond cobalt and conducting the similar chemistry with nickel resulting in a high-valent Ni(IV)-nitrate complex. Chapter 5 provides an overall summary and future perspective of the project.

Acknowledgements

I want like to thank my research advisor, Dong Wang, for his support, guidance, encouragement, and positive attitude every step of the way of my doctorate journey. As his first graduate student, I am very thankful that he took a chance on me when I joined the department at UM and his lab allowing me to work with and learn from. He has taught me to be patient, how to look and solve problems differently, communicate and collaborate effectively inside and outside of our lab, and push me to become a better chemist and person.

I am also thankful for everyone in the Wang lab (Yan Li, Garrett Evenson, Annie Schmautz, and Michael Kayne). We are small but mighty. I have learned and shared a lot of successes and learn from failures as well to support each other. I want to extend thanks to my committee members (Orion Berryman, Bruce Bowler, Chris Palmer, Steve Sprang, Ed Rosenberg) for also pushing me to become a better chemist and critical thinker, providing feedback and guidance, and support throughout this journey. I would also like to extend my thanks Dan Decato and the X-ray core facility for solving my crystal structures for this project as well as maintaining the NMR facility. Also to Earle Adams, prior to his departure, for fixing and maintaining the instruments in the department.

Moving to MT from WA knowing no one and being in new environment, I am thankful for all the friends I have made inside and outside of the department and make genuine connections. Truly grateful for them as they have supported, encouraged, and motivated me to stay strong and that everything will be okay. I really appreciate them for being there and without them I would not know where I would be. I would also like to thank my friends from back home in WA that have watched and supported me from afar on my doctorate degree.

Most importantly I would like to express my gratitude to my parents. They have always encouraged, supported, and inspired me to be the best I can be. I would also like to shout out to my grandparents who have been there to see me on this journey from a far and me knowing that they are proud of me and the successes that I have accomplished has kept me going. At most I would like to express my thanks and appreciation to my sister Soobin, who has been by my side understanding the struggle that I have gone through with my graduate career and providing the support and advice. I hope to return the support to her as she is going through her graduate career right now. Thank you to my family with all my love.

Finally, I would like to express my appreciation and gratitude to the Department of Chemistry and Biochemistry at the University of Montana.

Table of Contents

List of Figures

List of Tables

List of Schemes & Equations

List of Abbreviations

^{1}H NMR – Proton NMR
αKG - α-ketoglutarate
Å – Angstrom
$AgBF_4$ – Silver Tetrafluoroborate
Ar - Argon
atm - Atmosphere
BDE – Bond Dissociation Energy
CAN – Cerium(IV) Ammonium Nitrate
$CDCl_3$ – Deuterated Chloroform
CH_2Cl_2 – Dichloromethane (CD_2Cl_2 is the deuterated form)
CH_3CN – Acetonitrile (CD_3CN is the deuterated form)
c-C_6H_{10} - Cyclohexene
Co – Cobalt
Cu - Copper
CV – Cyclic Voltammetry
D/d - Deuterium
DCM – Dichloromethane
DFT – Density functional theory
DHA – 9,10-dihydroanthracene
Et_2o – Diethyl ether
Et_3N – Triethylamine
EPR – Electron Paramagentic Resonance Spectroscopy
eq - Equivalent
Fc/fc - Ferrocene
FTIR – Fourier Transform Infrared Spectroscopy
h – hour(s)
H – Hydrogen
HAT – Hydrogen atom transfer
k_2 – Second-order rate constant
k_{obs} – Pseudo-first-order rate constant
KIE – Kinetic isotope effect
M – Molar
MO – Molecular orbital
mM – millimolar
mmol - millimole
MeOH -Methanol
N_3 - Azide
NaOH – Sodium hydroxide
$NaSO_4$ – Sodium sulfate
NMR – Nuclear Magnetic Resonance Spectroscopy
Ni - Nickel

nm – nanometer
OH – Hydroxide
ONO_2/NO_3 – Nitrate
PhEt – Ethylbenzene
phIO - Iodosylbenzene
PhMe - Toluene
ppm - Parts per million
py - Pyridine
RT – Room temperature
s - seconds
SOMO – Singly occupied molecular orbital
T - Temperature
THF – Tetrahydrofuran
TMA – Trimethylaluminum
TMAOH – Tetramethylammonium hydroxide
$TMAN_3$ – Tetramethylammonium azide
TMS - (Trimethylsilyl)-methyllithium
UV-Vis – Ultraviolet-Visible Spectroscopy
XAS – X-ray Absorption Spectroscopy
XRD – X-ray Diffraction
π – pi
σ - sigma

Chapter 1: Introduction

1.1 C-H Bond Activation

In nature, metalloenzymes perform a wide array of biological processes with remarkable efficiency and selectivity such as bond cleavage, bond formation, electron transfer, atom transfer, etc.[1] These enzymes have control over both structural and electronic properties within their active site in order for these processes to take place.[2-4] One of the most challenging conversions is the activation of C-H bonds that has been studied in both biological and industrial catalytic processes. Alkanes are major constituents of natural gas and petroleum, but practical processes for directly converting them to more valuable products are scarce.[5] Conversion of these alkanes are difficult due to the strong C-H bonds having relatively large bond dissociation free energies (BDFE) that can approach 100 kcal/mol. Efforts to understand this phenomenon have been made through chemical synthesis and transition metal catalysis.[5-8] Therefore, the development of less toxic and inexpensive metal catalysts as agents for C-H bond activation continues to be an unsolved challenge.

Natural metalloenzymes have the capability to activate strong aliphatic C-H bonds by engaging terminal high-valent metal-oxo species in their catalytic cycles. These species are believed to be key intermediates and play an active role in many transformations such as dioxygen transport, dioxygen activation, etc.[9-11] The study of metal-oxo species began over half a century ago when Hayaishi and co-workers showed that an Fe-containing enzyme could mediate the incorporation of oxygen atoms derived from molecular oxygen into organic substrates in pyrocatchase[12] and the concept of "high-valent Fe(IV)-oxo

species" was proposed in the Fenton reaction system (Fe^{2+} + H_2O_2) as an alternative oxidant to interpret the regio- and stereo-selectivity for hydroxylation of cyclohexanol.[13,14] The study of mononuclear heme and nonheme Fe oxygenases initiating these chemical transformations have been heavily investigated.[11, 15-19]

High-valent Fe(IV)=O intermediates (with a terminal oxo ligand) have been identified as the key oxidants to initiate the activation of C-H bonds through an "oxygen rebound" mechanism reported by Groves and co-workers.[20,21] This finding now appears to be ubiquitous across many areas of chemistry. Examples of enzymes that undergoes this "oxygen rebound" mechanism are the nonheme monoiron α-ketoglutarate (αKG) dependent enzymes. They perform a wide variety of transformations including halogenation, hydroxylation, desaturation, etc.[22] The catalytic cycle shown below is thought to be similar for all αKG dependent enzymes (**Figure 1.1**).[23]
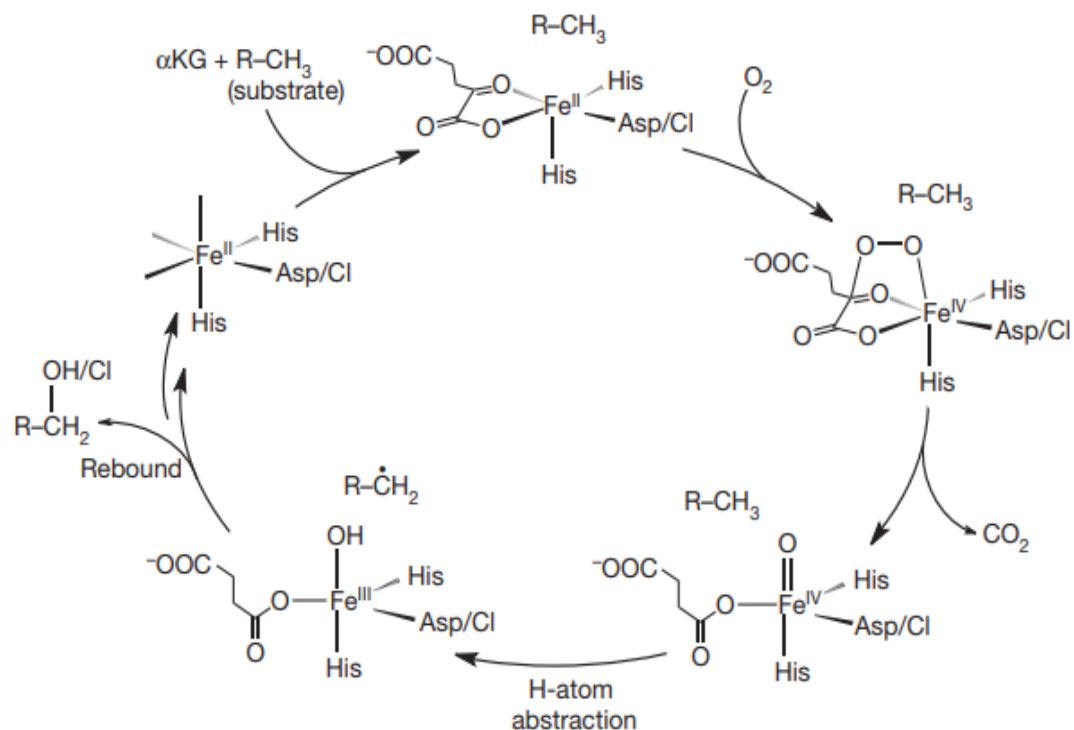
Figure 1.1 Catalytic cycle of αKG-dependent enzymes.[23]

The catalytic cycle of αKG-dependent oxygenases features three highlights: the generation of the Fe(IV)=O intermediate upon the activation of O_2, Fe(IV)=O intermediates abstract a hydrogen atom from the substrate to generate a Fe(III)-OH and a carbon radical, and the rebound of the hydroxyl group from Fe(III)-OH to the carbon radical to form the hydroxylated product.[19,23-25] In fact, when the "rebound" in the catalytic cycle of αKG-dependent enzymes occurs, it is not only limited to form the hydroxylated product but also has the ability to install non-hydroxyl functional groups.[23,26-28]

1.2 Synthetic Models

Due to the nature of these metal-oxo intermediates, the chemical and functional properties (e.g. structure, magnetic and electron structure, function, reactivity, chemical

mechanism, etc.) remain elusive. Through biomimetic and bio-inspired (synthetic) models supported by organic ligands, these properties can be clarified with detailed insight that cannot be easily attained from protein studies.[29] An inventory of synthetic high-valent metal-oxo complexes of early and middle transition metals (up to group 8 on the Periodic Table of Elements) has been reported.[11,21] First row transition metal ions, such as Fe, Mn, and Cu, often play a dominant role in metalloenzymes for the activation of O_2 to carry out biological processes such as C-H bond activation, C-X bond formation, etc.[30-32] Iron is the most common transition metal used for O_2 activation due to the its ability to access multiple redox states, as well as its bioavailability.[33] Examples of heme and nonheme synthetic metal-oxo intermediates modeling biological systems are shown in **Figure 1.2**.[33]
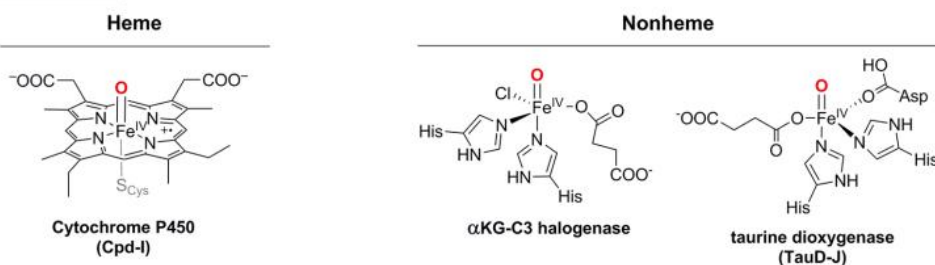
Figure 1.2. Examples of heme and nonheme M^{IV}=O intermediates in biological and synthetic model systems (M = Fe or Mn).[33]

It wasn't until the 1980s when Groves and co-workers reported the first synthetic model of a high-valent oxoiron porphyrin complex, [9TMP$^{+\bullet}$]Fe^{IV}(O)Cl] (model shown in **Figure 1.2**) identified to be similar in the catalytic cycles of horseradish and cytochrome *c* peroxidase.[34] Using X-ray absorption spectroscopy, the Fe^{IV}=O bond length of this complex was reported.[35-37] This discovery by Groves and co-workers laid the foundation for the development of many mononuclear, early and middle transition metal-oxo complexes to be reported synthetically and computationally[11,15-19,21,38-46] and present a better understanding of high-valent metal oxo species of its structure and function.

As we go beyond group 9 of the Periodic Table of Elements, the isolation of high-valent metal-oxo complexes for these late transition metals is rare and synthetically challenging.[47] This could be due to the increase of oxidation potential and the increase in the number of d-electrons as we go across the periodic table making it difficult to access high oxidation states of late transition metals.[48] It has been reported that high-valent Co^{IV}- and Ni^{IV}-oxo species are involved in the following reactions: water oxidation and C-H bond cleavage, but more importantly through computational studies that Ni^{IV}-oxo species are capable of activating the C-H bond of methane at room temperature.[47,49-53] Therefore, the research on the development of synthetic models for generating stable metal-oxo complexes of these late transition metals have been heavily investigated. To date, there have only been a handful of stable synthetic Co^{IV}-oxo and Ni^{IV}-oxo complexes and their isoelectronic analogs reported.[42-47,54-59] There have been no reports of Cu^{IV}-oxo complexes yet.

1.3 The "Oxo-Wall" Theory

The generation of synthetic late-transition metal-oxo species remains a challenge due to the combined requirements of a low number of d-electrons and limited oxidation states of the metal presenting an "*oxo wall*" between Fe-Ru-Os (group 8) and Co-Rh-Ir (group 9) (**Figure 1.3**).[60,61]

Figure 1.3. D-block of the Periodic Table with groups 8 and 9 separated by the oxo wall.[60]

The formation of a stable terminal metal-oxo bond can be done with an octahedral symmetry (**Figure 1.4 a**) from a simple ligand field theory that was initially predicted by Gray and Ballhausen and later expanded further by Gray and Wrinkler. [61-63] The perfect octahedral d-orbital splitting pattern: $d_{xy} = d_{xz} = d_{yz} < d_{x2-y2} = d_z$ was used as a guide (**Figure 1.4 b**). The theory was verified with a vanadyl ion (d^1 configuration) resulting a strong and stable $V \equiv O$ bond. They proposed that the metal-oxo complex must be in an octahedral symmetry (C_{4v}) where the perfect octahedral d-orbital splitting pattern will change the order of the d-orbitals to $d_{xy} < d_{xz} = d_{yz} < d_{x2-y2} < d_z$ (**Figure 1.4 c**) where the d_{xz}, d_{yz} orbitals (π^* orbitals) are above the d_{xy} orbital. This theory resulted that a stable M=O bond in a C_{4v} symmetry is only possible with a d-electron configuration of 4 or less. A high d-electron count of 5 or more and bond orders of < 2 leads to the further occupation of the d_{xz} and

d_{yz} orbitals with more than two electrons making the M-O bonding extremely unstable and very reactive.[62]
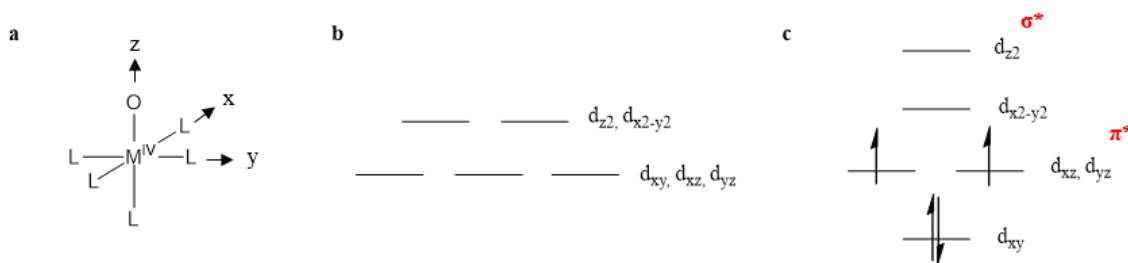
Figure 1.4. a) Terminal metal-oxo complex with an octahedral symmetry, **b)** Perfect octadedral d-orbital splitting diagram, **c)** shift in d-orbital splitting diagram to form a M-O bond (σ^* and π^* orbitals are shown in red) to with the occupation of d^4 electrons fully occupying the d_{xy} and half-filled d_{xz} and d_{yz} orbitals.

1.4 Generation of Late Transition Metal-Oxo Complexes

Breaking the "*oxo wall*" is a challenge. One group proposed to overcome this phenomenon but was proven incorrect.[60] One credible strategy to successfully generate stable high-valent late-transition metal-oxo complexes with an oxidation state of +4 complexes is to change the symmetry of the metal center by reducing the number of ligands. There have only been a few successful reported examples departing from the octahedral geometry.

In 2008, Milstein and co-workers reported the characterization of a d^6 Pt(IV)-oxo complex supported by a tridentate ligand with a distorted square planar geometry verified by XAS and computational studies (**Figure 1.5, left**).[54,65] This $Pt^{IV}=O$ species exhibits reactivity as an oxygen donor and an electrophile, but not as a C-H bond activation reagent. Through these analyses, Milstein and co-workers indicate that a four coordinated species with a square planar geometry might hold the key to successfully generate a stable high-valent oxo species. Recently, Anderson and co-workers reported a

structurally characterized d^6 terminal Co(III)-oxo supported by a monoanionic, tridentate ligand with a distorted tetrahedral geometry (**Figure 1.5, right**).[56,65] This Co[III] species exhibits reactivity as a slow oxidant in both oxygen atom transfer and C-H bond cleavage reactions. From these two complexes, this gives motivation to "break the oxo-wall" by developing new synthetic strategies to generate high-valent metal-oxo complexes enforcing a four-coordinate geometry.
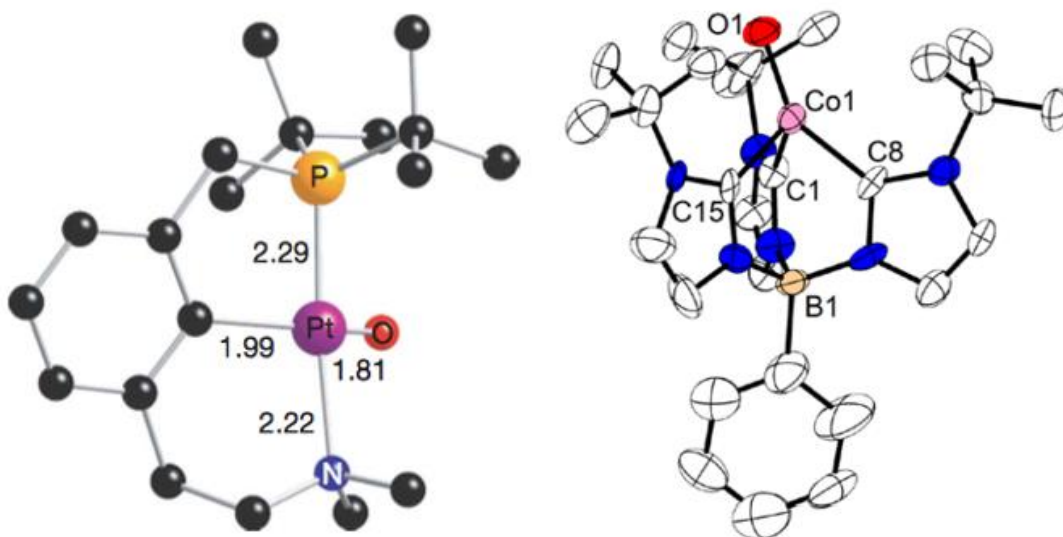
Figure 1.5. Left. Optimized structure of d^6 Pt(IV)-oxo complex reported by Milstein and co-workers.[54] **Right.** Crystal structure of d^6 Co(IV)-oxo complex reported by Anderson and co-workers.[56]

Most recently, Nam and co-workers reported a distorted Co(IV)-oxo complex with a tetragonal symmetry characterized by various spectroscopic techniques.[59] They reported another well-characterized Co(IV)-oxo species since their last reported Co(IV)-oxo complex.[55] They showed that their recent Co(IV) complex shows electrophilic reactivity in hydrogen atom transfer (HAT) and oxygen atom transfer (OAT) reactions. They also have found that secondary coordination sphere interactions can fine tune the

metal-oxo bonds. Even though their recently reported Co(IV) complex was found to have formal bond order of 2, they still report that the "oxo-wall" remains intact as their complex does not have a tetragonal structure. Even though, this recent report of a Co(IV)-oxo species didn't break the "oxo-wall" but changing the geometry and implementing other aspects into the complex can influence the reactivity and chemistry behind high-valent late transition metal-oxo complexes.

There have been recent developments of high-valent non-oxo metal species of late transition-metals of oxidation states of +3 or higher and most of these systems exhibit reactivity as an oxidant for C-H bond activation. [66-82]. All these systems are informative and inspiring. Selection of the coordinating ligand from oxo to non-oxo groups such as hydroxo, nitro, halides, etc. gives us more insight into understanding the high-valent metal chemistry. Not only do these complexes exhibit reactivity as an oxidant for C-H bond activation but also as a HAT reagent. In this inventory of high valent metal-oxo and non-oxo complexes, it is still surprising of the limited examples of high valent Co(IV) complexes reported and how there are no reports of complexes of Ni and Cu with the oxidation state of +4 available for the activation of sp^3 C-H bonds.

1.5 Research Objectives

Ultimately the goal of many research groups including ours is to obtain a synthetic high-valent terminal metal-oxo complex. There are many alternative approaches and strategies. The strategy that is usually thought of is to synthesize high-valent metal-non-oxo complexes. As written above, there has been much development on these complexes. These complexes could provide us information and results that can lead us to understand

the chemistry and achieve the goal to obtain a high-valent metal-oxo complex and to study its reactivity towards the activation of C-H bonds. At the beginning of this project, we did and still have the goal to hopefully achieve a high-valent metal-oxo complex, but results obtained led us to open a gateway that could help us get to the goal in the future.

The research described in this dissertation focuses on the chemistry of mononuclear high-valent metal-nonoxo complexes of Co and Ni. A series of Co and Ni complexes with oxidation states of +2, +3, and +4 supported by a di-anionic, tridentate ligand backbone were synthesized and characterized using various spectroscopic methods that will be described throughout the dissertation. We then studied the chemical reactivity of these complexes for the activation of C-H bonds. The results that will be discussed in this dissertation will advance the development of more reactive high-valent late transition metal complexes and will lead for a more in-depth understanding of the chemistry behind the catalytic C-H bond activation.

Chapter 2: Early Stages Development

2.1 Preface

This chapter will describe the early stages and the development of the mononuclear high-valent late-transition metal-oxo complex project in Dr. Dong Wang's research lab. This chapter will discuss the synthesis and characterization of the precursor Ni^{II}-OH complex in efforts of obtaining a high-valent Ni^{IV}-oxo complex to study its reactivity towards sp^3 C-H bonds.

2.2 Introduction

At the beginning of the project, we had similar views with other synthetic bioinorganic chemistry groups that the development of high-valent metal-oxo is a challenge. We hypothesized that we could generate high-valent metal-oxo complexes by employing a tridentate, di-anionic N,N'-disubstituted 2,6-pyridinedicarboxamidate pincer ligand scaffold (pyN$_2$^{Me2}, **Scheme 2.1**). This ligand scaffold and its derivatives supported the formation of Ni(II) complexes with a square planar geometry.[83,84] The electronic and structural properties of this scaffold were well characterized and studied. Incorporation of the anionic *N*-donor(s) into the design of ligand scaffold have been tested and successful for accessing and stabilizing high-valent species.[84-87] These features of the ligand made pyN$_2$^{Me2} an ideal ligand scaffold to stabilize a high-valent species.

There have been reports of Ni (II/III) and Cu (II/III) species of the pyN$_2$^{Me2} ligand.[68-78, 89] Parallel to our project at this time was the work that McDonald and co-workers reported: the synthesis and characterization of the corresponding Ni^{III} species of the pyN$_2$^{Me2} ligand, generated by one electron oxidation of the Ni^{II} precursor.[67,68] The work

provided persuasive precedents to jump start our project by reacting the Ni^{II} precursor

with an oxo, two electron oxidant to produce a $Ni^{IV}=O$ species.

2.3 Results and Discussion

2.3.1 Synthesis and Characterization of (pyN$_2$^{Me2})Ni(II)-OH

The main ligand scaffold, *N, N'*-Bis(2,6-dimethylphenyl)-2,6-pyridinedicarboxamide (H$_2$pyN$_2$^{Me2}) (**L1**), was synthesized following the experimental procedure (**Scheme 2.1**) reported by Holm and co-workers.[83] [1]H Nuclear Magnetic Resonance (NMR) analysis confirmed the identity of **L1** (**Figure S1**). The Ni(II)(pyN$_2$^{Me2})-OH complex (**1**) also reported by Holm and co-workers was synthesized using an alternative approach. This approach used acetonitrile as the solvent and a different base, tetramethylammonium hydroxide (TMAOH), to deprotonate the ligand (**Scheme 2.2**).
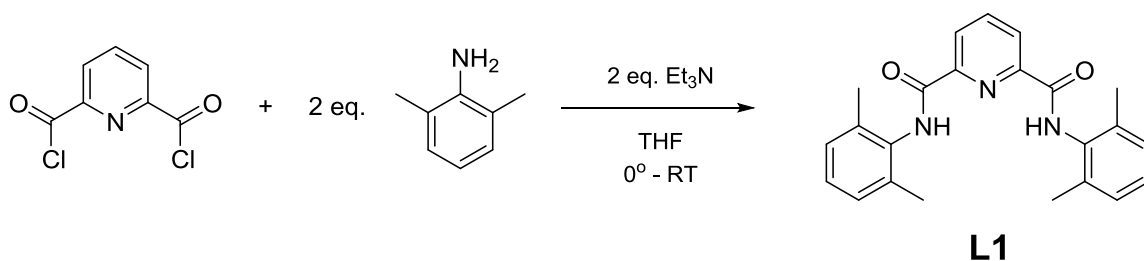
Scheme 2.1 Synthesis of *N, N'*-Bis(2,6-dimethylphenyl)-2,6-pyridinedicarboxamide
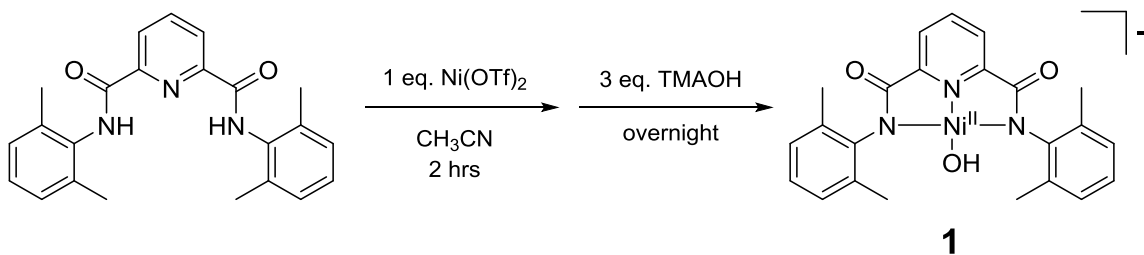
Scheme 2.2 Synthesis of (pyN$_2$^{Me2})Ni^{II}-OH (**1**)

Red-orange crystals of **1** were obtained by layering diethyl ether (Et_2o) onto a filtered solution of **1** in dichloromethane (DCM) over a two-day period. Crystallized sample of **1** was analyzed with X-ray crystallography shown in **Figure 2.1**. The results confirmed the mononuclear Ni center is four coordinated with a square planar geometry. The structure is enforced by the sterically bulky 2,6-dimethylphenyl groups and the fourth coordination site occupied by the hydroxide ligand. The Ni-O distance of 1.819 Å is similar to the distance reported by Holm and co-workers. Further characterization was done by ^{1}H NMR spectroscopy indicating **1** is a diamagnetic species (**Figure S2**). Due to its stable and diamagnetic nature, **1** was suitable as an outstanding precursor for the generation of a high-valent Ni(IV)=O species and to understand the chemistry.
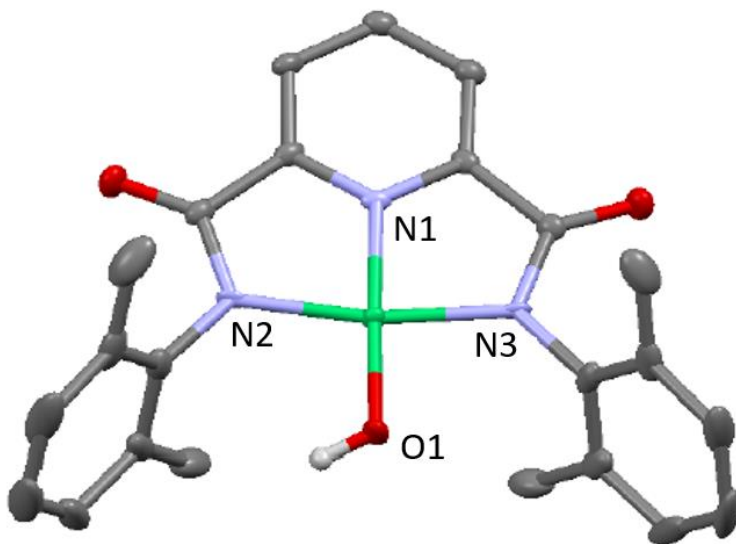
Figure 2.1. X-ray crystal structure of **1**. Hydrogen atoms (except the one on the hydroxyl group) have been omitted for clarity. Selected bond lengths for one independent molecule in the unit cell: Ni-N1 1.824 Å, Ni-N2 1.896 Å, Ni-N3 1.893 Å, Ni-O1 1.819 Å.

2.3.2 Generation and Reactivity of a Putative Ni(IV) Species

After the successful synthesis of the mononuclear Ni(II)-OH complex, the next step was to oxidize the Ni(II) center using a two-electron oxo-transfer oxidant, iodosylbenzene (PhIO) (**Scheme 2.3**). To an orange solution of **1** in acetonitrile (MeCN/CH$_3$CN), one equivalent of PhIO in methanol (MeOH) (PhIO has a low solubility in most organic solvents) was added into the solution, resulting in a formation of a new nickel species. In the UV-Vis spectra, we can immediately see a growth of strong band at 333 nm and a weak band at 443 nm (**Figure 2.2**). These features observed were different from the Ni^{III}(pyN$_2$^{Me2}) complexes reported by McDonald and co-workers[68,69] (absorption bands at 520 nm and 790 nm) and any other Ni^{II} species previously characterized by Holm and co-workers[82], indicating the nickel species generated is novel and has not been previously observed.
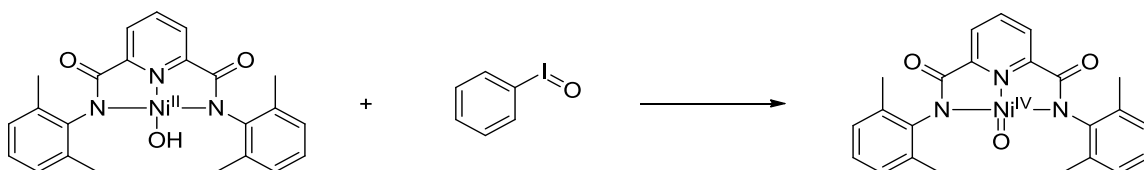
Scheme 2.3. Reaction of **1** with 1 equivalent of iodosylbenzene with desired product
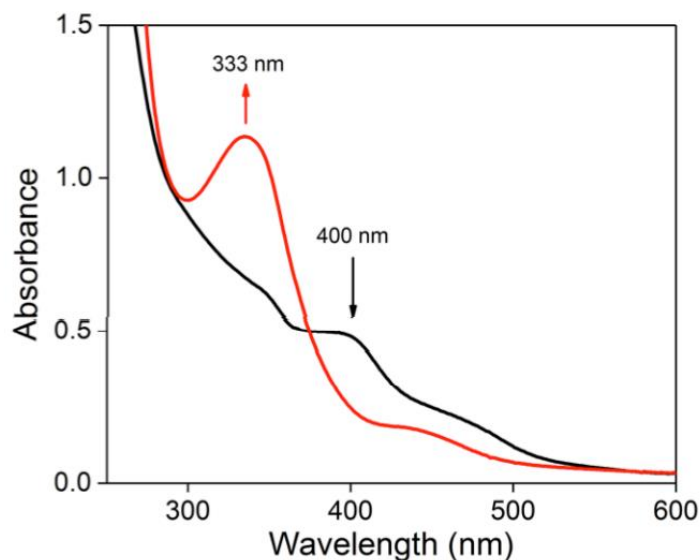
Figure 2.2. UV-Vis spectra for the conversion of 0.1 mM **1** (black) with one equivalent of iodosylbenzene to form product at 333 nm (red) in acetonitrile at room temperature.

Reaction of **1** with PhIO was fast in the entire temperature range tested from -40° C to 25° C with an isosbestic point at 375 nm. No other intermediate was detected. Attempts to obtain crystals suitable for x-ray crystallography of the novel nickel species were made in hopes to obtain structural information. Unfortunately, the crystals obtained after the reaction with PhIO resulted in a $Ni^{II}(pyN_2^{Me2})$-O_2CCH_3 complex (**Figure 2.3**). The bonds of $Ni^{II}(pyN_2^{Me2})$-O_2CCH_3 are similar to the bonds reported in **1**. We have investigated the chemistry behind the formation of this Ni(II) complex and have concluded that this is the decay product of a short-lived Ni(IV)=O species, which was not observed on the time scale of the UV-Vis experiment.
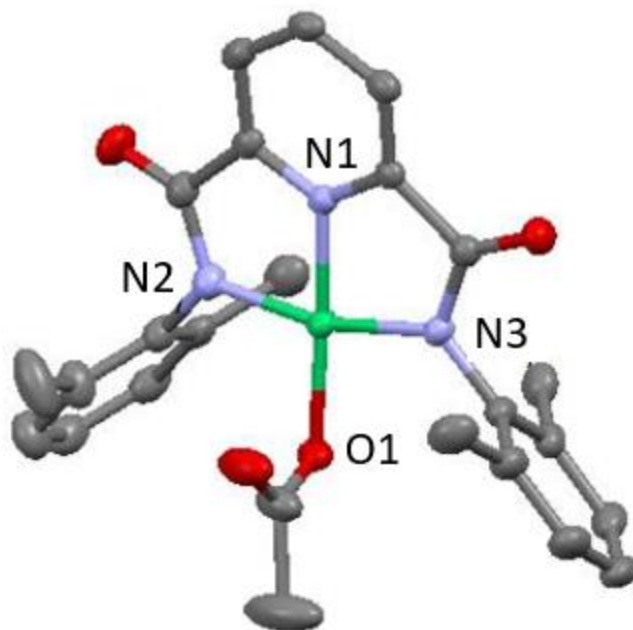
Figure 2.3. X-ray crystal structure of Ni(II)-O_2CCH_3 complex. Hydrogen atoms have been omitted for clarity. Selected bond lengths for one independent molecule in the unit cell: Ni-N1 1.823 Å, Ni-N2 1.907 Å, Ni-N3 1.907 Å, Ni-O1 1.895 Å.

As this novel nickel species is highly stable even at room temperature, we conducted experiments to observe the reactivity with external substrates such as 9,10-dihydroanthracene (DHA), triphenyphosphine (PPh$_3$), thioanisole (PhSMe), and ferrocene (Fc). These experiments were conducted through gas chromatography-mass spectroscopy (GC-MS) and Ultra-Violet Visible spectroscopy (UV-Vis). Unfortunately, there was no reactivity seen with these substrates before and after the addition of one equiv. of PhIO. This states that **1** is preferred over the substrate upon the reaction with PhIO. Due to the results obtained, we were eager to find evidence for the generation of this putative Ni^{IV}=O species and gain more insight of its formation and decay pathway(s) by modification and characterization.

2.3.3. Characterization of Putative Ni(IV) species

The first modification we made to hopefully trap an intermediate after the addition of PhIO to **1**, was to change the solvent was from CH_3CN to dichloromethane (CH_2Cl_2/DCM). The starting complex **1** showed an absorption maximum at 390 nm, similar to what was observed in CH_3CN. To a solution of 0.1 mM **1**, the addition of one equivalent of PhIO, we observed a shift in absorption from 396 nm to 375 nm. Over time, we then observed the shift in absorption from 375 nm to 343 nm. After it reached a max absorbance at 343 nm, the absorbance began to decrease reaching a 0-absorbance indication of product decomposition (**Figure 2.4**). This reaction was done at room temperature and was run for two hours. The stoichiometry of **1** and PhIO was determined by titration experiments and was found to be 1:1. These features differ and confirm that the initial reaction product is not stable and is possibly more reactive in DCM.
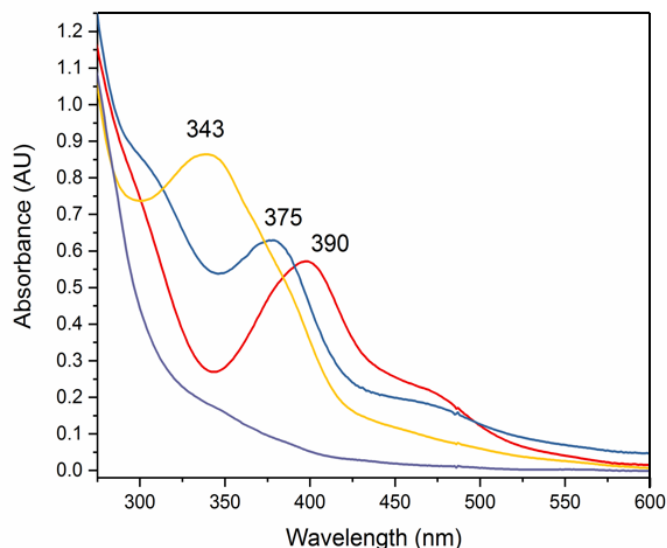
Figure 2.4. UV-Vis spectra for the conversion of 0.1 mM **1** (red) with one equivalent of iodosylbenzene to form initial products with spectra maxima at 375 nm (blue) to 343 nm (yellow) and decayed product (purple) in dichloromethane at room temperature.

These results indicate the formation of two species at absorbance maximums at peaks 375 and 343 nm. As this reaction was done on a scale for UV-Vis, the reaction was found to be photoactive in order to observe the shift in absorption from 375 to 343 nm. Both species are stable but too much UV light exposure to the solution will decompose the product at 343 nm. We hypothesized that upon the addition of PhIO, Ni^{II}-OH undergoes a ligand exchange replacing the hydroxide with PhIO and UV-light will push the Ni^{II}-O-IPh to generate Ni^{IV}=O.

We conducted reactivity studies by adding substrates: PPh_3 and DHA, and monitoring the reaction at 375 nm and 343 nm. We observed there was no oxo-transfer upon adding PPh_3 and DHA at peak 375 nm, but there was oxo-transfer between the substrate and the Ni complex at peak 343 nm. Products from these reactions at 343 nm were determined by GC-analysis. The yield of PPh_3O was ~94% after the addition of PPh_3 and the yield of anthracene was 60% after the addition of DHA. Another product that was found after the addition of these two substrates was iodobenzene (PhI) after the oxo transfer, the yield was 92% (after PPh_3 addition) and 40% (after DHA addition).

^{1}H NMR spectroscopy was undertaken to characterize the products at peaks 375 nm and 343 nm after the addition of PhIO. In comparison with the ^{1}H NMR spectra of Ni^{II}-OH (peak 390 nm), changes in the NMR spectra were observed in the aromatic region (6.5-8ppm) and the region where the dimethyl protons are (2.5 ppm) (**Figure 2.5**). From the ^{1}H NMR spectra at 343 nm, we were able to define the peaks corresponding to PhIO and PhI, indicating there was an oxo-transfer and a reaction did occur. Furthermore, the

data collected gave us more confidence and evidence that we have generated a putative

Ni^{IV}=O species.
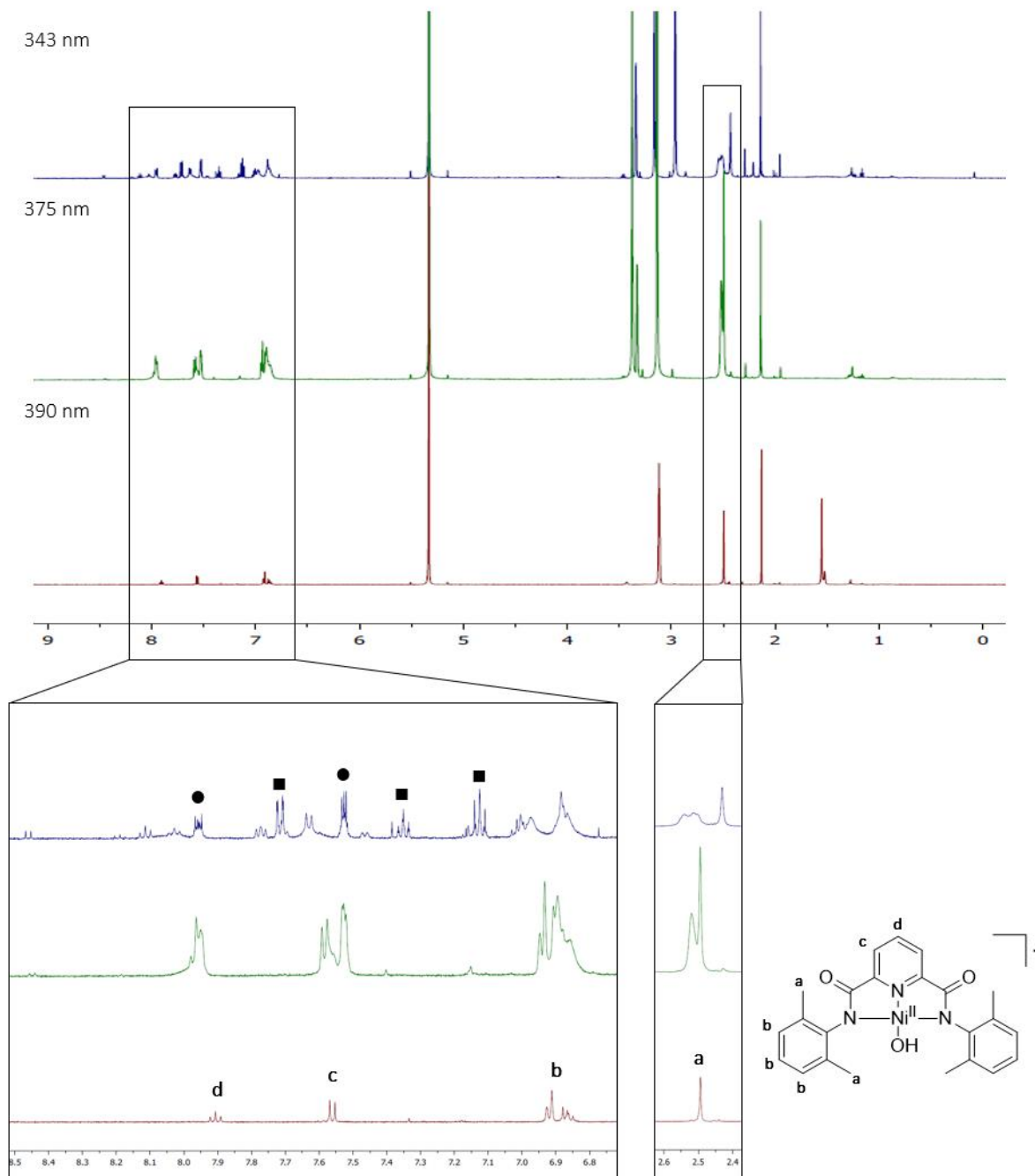
Figure 2.5 Stacked NMR spectra (CD$_2$Cl$_2$) upon the addition of 1 equiv. of phIO shown zoomed in aromatic region (6.5-8 ppm) and region of 2.5 ppm. **Bottom:** Ni^{II}-OH complex (CD$_3$CN) at 390 nm with structure shown on the right with corresponding protons; **Center:** Product at 373 nm; **Top**: Product at 343 nm with peaks of PhI (■) and PhIO (●) labeled.

2.4 Conclusions

We made efforts to obtain more structural information for the products with absorbance maximums at 375 and 343 nm by growing crystals suitable for x-ray crystallography, but unexpectedly obtained Ni^{II}-O_2CCH_3 complex. We conducted more ^1H NMR and ^{18}O labelling experiments but many efforts of trying to understand the mechanism of how the oxo-transfer occurred, the results obtained were unconvincing. During this investigation, after many experiments and inconclusive results, we decided that the key to generate a high-valent metal-oxo complex was to alter our ligand scaffold by removing the electron-withdrawing carbonyl (C=O) groups and replacing them with saturated aliphatic dimethyl groups. We hypothesized that the Co^{III}-OH complex reported by Lavoie and co-workers[90] would be an excellent precursor and candidate for us to obtain a high-valent Co^{IV} complex.

Chapter 3 focuses on our efforts to synthesize and characterize a series of Cobalt complexes supported by the new di-anionic, tridentate pincer ligand scaffold using various spectroscopic methods. Chapter 3 will also describe the generation of the first Co(IV)-O containing species that is structurally characterized by X-ray crystallography and is able to carry out C-H bond cleavage up to 87 kcal/mol.

Chapter 3: Generation, Characterization, and Reactivity of a Mononuclear Cobalt(IV)-dinitrate Complex

3.1 Preface

This chapter will describe the methods used for synthesis and characterization of a series of cobalt complexes with oxidation states of +2, +3, and +4 including reactivity studies of a mononuclear Co^{IV}-dinitrate complex. This chapter includes work that was published in the *Journal of the American Chemical Society* (2020, 142, 13435-13441) and was also featured in *JACS Spotlights* (2020, 142, 33, 14005–14006).[91] This publication was co-authored with Yuri Lee, Garrett E. Evenson, Prof. Dong Wang, and Prof. Timothy A. Jackson.

3.2 Introduction

After multiple experiments with fascinating results and unsolved mysteries described in Chapter 2. Our group hypothesized that the key to generate high-valent metal-oxo complexes was to modify the ligand scaffold, 2,6-pyridinedicarboxamidate ($H_2pyN_2^{Me2}$), **L1**. We will adapt the ligand scaffold that afforded a Co^{III}-OH complex reported by Lavoie and co-workers.[90] We will be using this Co(III) species as our starting complex to generate a high-valent Co(IV) species. This N3 ligand lacks the electron-withdrawing carbonyl groups making the anionic *N*-donors more electron-donating and could stabilize the high-valent oxidation state of +4 compared to the Ni(III) and Cu(III) complexes that were reported by McDonald, Tolman, and Zhang groups.[68-78]

The generation of high-valent metal-oxo complexes going past the "oxo wall" to understand the structural and electronic properties and substrate C-H bond reactivities

remains a challenge. There are only a few examples of high-valent late transition metals-oxo complexes (Co, Ni, and Cu) reported.[55,56,58,59, 65,82] To date, there is only one terminal Co^{III}=O complex characterized by X-ray crystallography reported.[56] Recently, Roithova and co-workers described the generation of Co^{III}-oxyl (equivalent to Co^{IV}-O) species that is capable of cleaving strong C-H bonds.[81] Herein, we report the first high-valent Co^{IV}-dinitrate complex that is both structurally characterized by X-ray crystallography and capable of activating strong C-H bonds in the condensed phase and preliminary data of another high-valent Co^{IV} species.

3.3 Results and Discussion

3.3.1 Synthesis and Characterization of Co(II) and (III) Complexes

The first step was to generate the precursor ligand scaffold (2,6-bis((1-[(2,6-dimethylphenyl)imino]ethyl)pyridine) (**L2**) (**Scheme 3.1**) reported by Brookhart and co-workers.[92] This precursor ligand was then used to generate the main ligand scaffold (2,6-bis((2-(2,6-dimethylphenylamino))isopropyl)pyridine) (**L3**) (**Scheme 3.2**) according to the synthetic procedure reported by Lavoie and co-workers.[90] Both **L2** and **L3** was purified and characterized by ^{1}H NMR spectroscopy (**Figure S3 & S4**) prior to metallation. All complexes discussed from now on are supported by this rigid, di-anionic, electron-donating tridentate N3 ligand (**L3**).
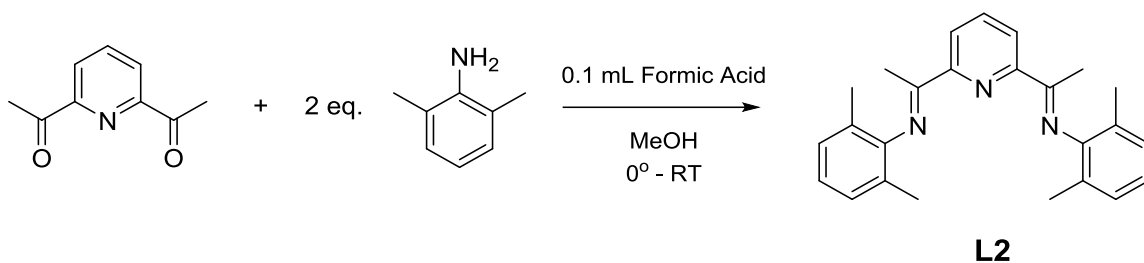
Scheme 3.1. Synthesis of [2,6-bis((1-[(2,6-dimethylphenyl)imino]ethyl)pyridine)
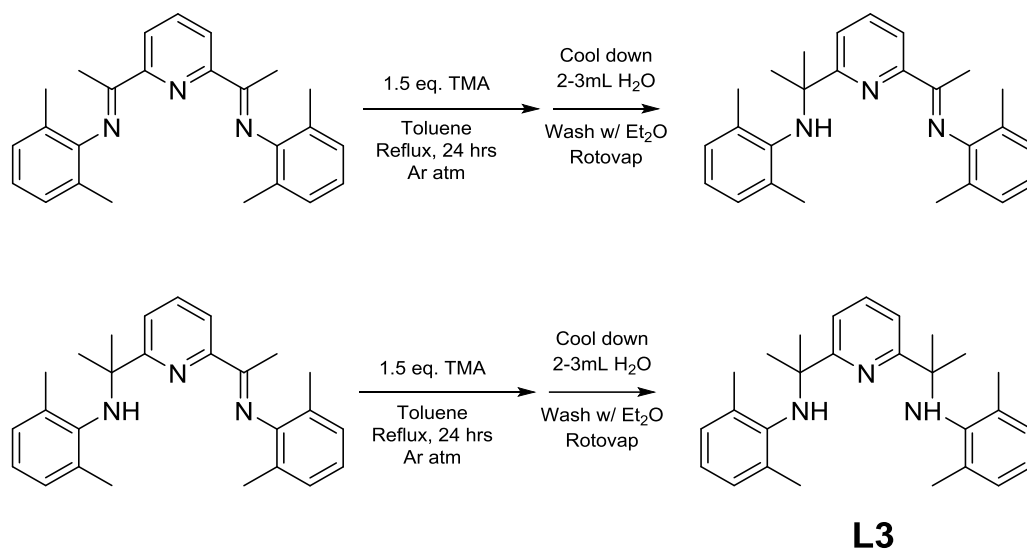
Scheme 3.2. Synthesis of [2,6-bis((2-(2,6)-dimethylphenylamino))isopropyl)pyridine]

Complexes Co^{II}-py (**2**), Co^{III}-py (**3**), and Co^{III}-OH (**4**) were synthesized according to the synthetic procedure reported by Lavoie and co-workers.[90] Complex **2** was synthesized and was immediately oxidized with silver tetrafluoroborate ($AgBF_4$) to generate **3** (**Scheme 3.3**). A ligand exchange of pyridine to hydroxide bound to the Co(III) center led to **4** (**Scheme 3.4**). There was no characterization of complexes **2** and **3** completed as they were immediately filtered and used to synthesize **4**.
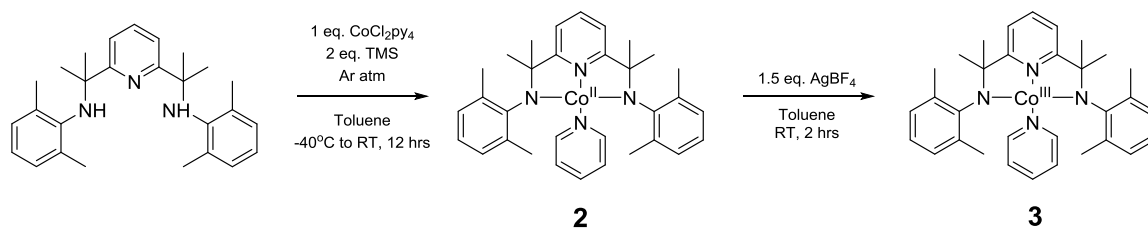
Scheme 3.3. Synthesis of Co^{II}-py (**2**) and Co^{III}-py (**3**)
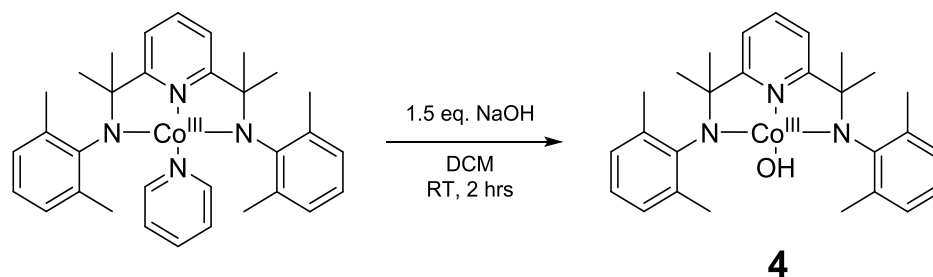
Scheme 3.4. Ligand exchange from pyridine to hydroxide bound to Co(III)

Purple crystals of **4** were produced by layering pentane onto a filtered solution of **4** in DCM and was set aside at room temperature. A crystallized sample of **4** was analyzed with X-ray crystallography. The X-ray crystal structure of **4** is shown in **Figure 3.1**. X-ray crystallographic analysis confirmed the Co(III) center is four coordinate with a slightly distorted square planar geometry. X-ray data analysis gave the Co-N$_{py}$ bond length of 1.862 Å, an average distance of 1.836 Å from the two Co-N$_{amine}$ bonds, and one Co-OH bond of 1.792 Å. The shorter Co-N$_{amine}$ bond length compared to the Co-N$_{py}$ bond indicates that the Co center interacts more strongly with the anionic N-donors from the amines than with the neutral pyridine ligand. The bonds in **4** are similar with the bond lengths and angles (not shown) reported by Lavoie and co-workers.[90]
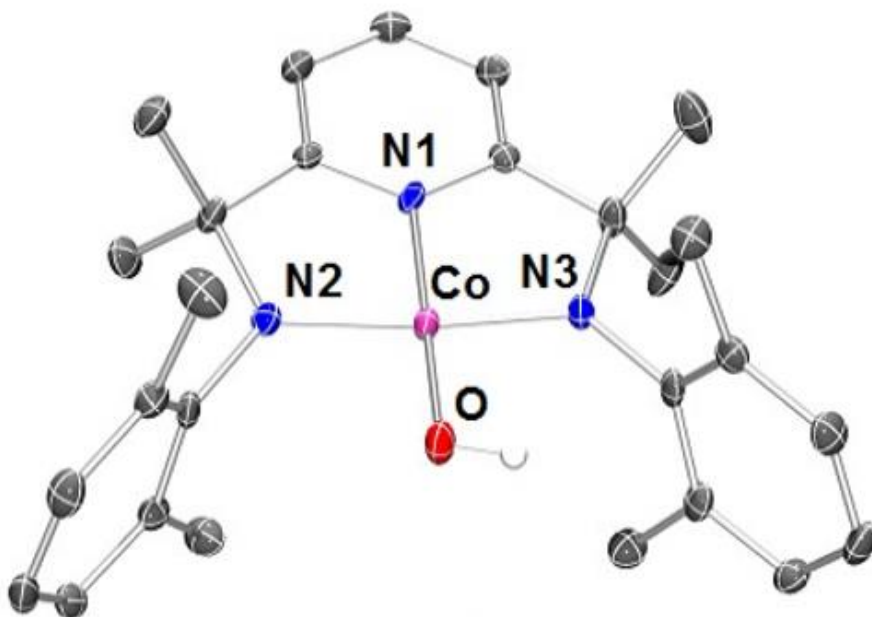
Figure 3.1. X-ray crystal structure of **4** with thermal ellipsoids drawn at 50% probability level. Hydrogen atoms (except the one on the hydroxyl group) have been omitted for clarity. Selected bond lengths for one independent molecule in the unit cell: Co-N1 1.862 Å; Co-N2 1.833 Å; Co-N3 1.840 Å; Co-O 1.792 Å.

The UV-Vis spectrum of **4** in acetonitrile exhibits a strong absorption at 570 nm (ε = 7300 M^{-1} cm^{-1}) (**Figure 3.2**). Further characterization of **4** was done using ^{1}H NMR (**Figure S5**) and electron paramagnetic resonance spectroscopies (EPR) confirming that **4** is a diamagnetic and an EPR-silent species. This data was found to be consistent with the assignment of having a low-spin d^6 Co(III) center.
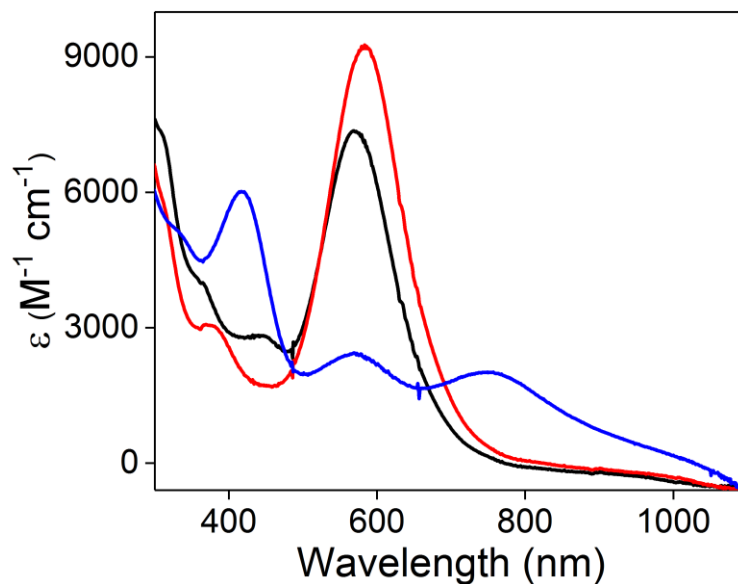
Figure 3.2. UV-Vis spectra of **4** (black), **5** (blue), and **6** (red) obtained in acetonitrile at room temperature.

3.3.2 Generation and Characterization of Mononuclear Co(IV)-Dinitrate Complex

The next step after synthesizing the starting complex, **4**, was to oxidize the Co(III) center using a one-electron oxidant: cerium(IV) ammonium nitrate ($(NH_4)_2Ce(NO_3)_6$, CAN) (**Scheme 3.5**). To a purple solution of **4** in CH_3CN, one equivalent of CAN in CH_3CN was injected into the solution at room temperature (RT) resulting in the generation of a new cobalt species, **5** (**Figure 3.2**). In the UV-Vis spectra, we can immediately see there was a decrease of the band at 570 nm and the appearance of a new intense band at 420 nm (ε = 5900 M^{-1} cm^{-1}) and two weaker bands at 565 nm (ε = 2400 M^{-1} cm^{-1}) and 750 nm (ε = 2000 M^{-1} cm^{-1}) (**Figure 3.3**). Two isosbestic points at 486 and 682 nm were observed suggesting that there was no intermediate involved in the conversion. The stoichiometry of **4** and CAN was determined by titration experiments and was found to be a 1:1 (**Figure 3.3, inset**). From these titration experiments, the addition of excess CAN did not cause a higher formation yield of **5**, verifying that **5** is a Co(IV) species.

27
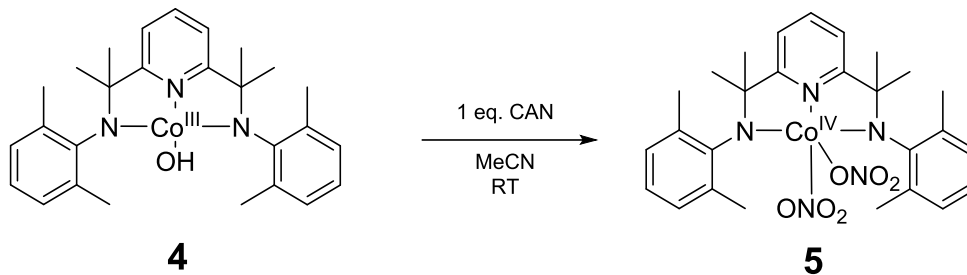
Scheme 3.5. Reaction of **4** with 1 equivalent of CAN to generate **5**
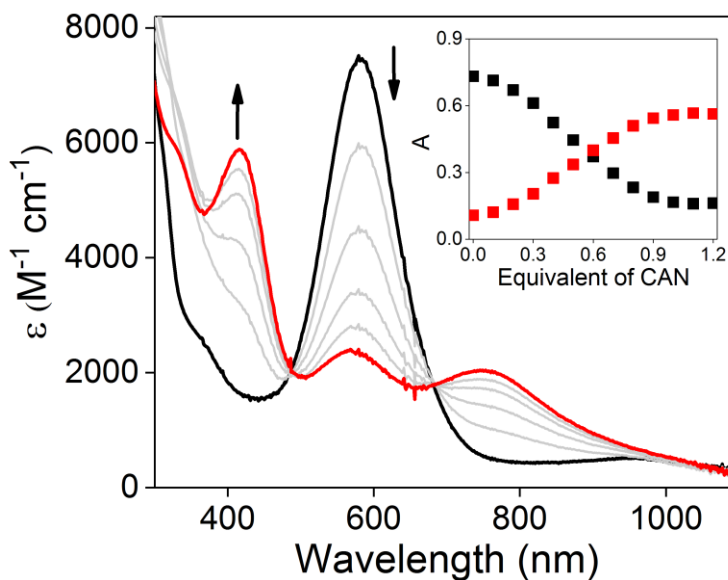
Figure 3.3. UV-Vis spectra for the conversion of **4** (black) to **5** (red) by one equivalent of CAN in acetonitrile at room temperature. Inset: titration of CAN monitored at 570 nm (black) and 420 nm (red).

We found that **5** had lifetime of several hours at RT and is stable at cryogenic temperatures. This gave us motivation to grow crystals suitable for X-ray crystallography to obtain structural information. In the process of synthesizing **5** on a bigger scale, we observed a color change in solution from purple to a dark green. Dark crystals of **5** were obtained by layering pentane onto a filtered solution of **5** in DCM set in a -30° C freezer for over a week. A crystallized sample of **5** was analyzed by X-ray crystallography. The X-ray crystal structure of **5** is shown as a Co(IV)-(ONO$_2$)$_2$ complex in **Figure 3.4**.

Figure 3.4. X-ray crystal structure of **5** with thermal ellipsoids drawn at 50% probability level. Hydrogen atoms have been omitted for clarity. Selected bond lengths and angles for one independent molecule in the unit cell: Co-N1 1.863 Å; Co-N2 1.831 Å; Co-N3 1.834 Å; Co-O1 2.100 Å; Co-O2 1.927 Å; O1-Co-O2 81.96°.

X-ray crystallographic analysis confirmed the Co(IV) center is a neutral mononuclear five coordinate species with a pseudo-square pyramidal geometry and a N3O2 donor set. The source of nitrate ligands in **5** appears to be from CAN. The Co(IV)-ONO$_2$ bond length in the axial position is 2.100 Å, which is 0.17 Å longer than the nitrate ligand in the equatorial position. This is an indication that the axial nitrate ligand interacts less strongly with the Co(IV) center compared to the nitrate ligand in the equatorial position. This feature was observed in two other reported square pyramidal Co(IV) complexes characterized by X-ray crystallography exhibiting a longer bond length between the Co center and the axial ligand.[93,94] Comparison of the Co-N$_{py/amine}$ bond lengths and selected carbon-carbon and carbon-nitrogen bond lengths of the N3 ligand in

5 are similar to the bond lengths reported for **4** (**Table S8**), indicating that the oxidation is a metal-centered instead of ligand-based process.

After the generation of **5**, we conducted an experiment to reduce **5** by ferrocene to regenerate a Co(III) species. To a solution of **5** in CH_3CN, one equivalent of Fc in CH_3CN was added to the solution generating **6**. Complex **6** exhibited an absorption band at 585 nm ($\varepsilon = 9200$ M^{-1} cm^{-1}) (**Figure 3.2 and 3.5**). Titration of ferrocene to the solution of **5** (**Figure 3.5, inset**) revealed the formation yield of **5** to be 90%. We see the absorption band shift ~15 nm compared to **4** (570 nm), we hypothesized that this Co(III) species is bound to a nitrate ligand. We verified this hypothesis when we performed a ligand exchange monitored by UV-Vis spectroscopy when excess tetrabutylammonium nitrate reacted with **4** resulted in the generation of **6** (**Figure 3.6**). An oxidation experiment was conducted when **6** reacted with CAN resulting in the generation of **5** (**Figure 3.7**). We see a similar observation when the conversion of **4** to **6** was complete therefore, the conversion seen from **6** to **5** is chemically reversible.
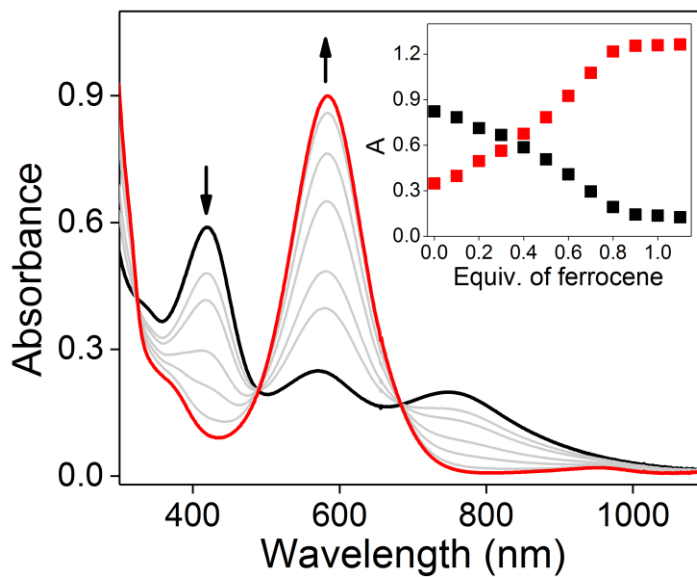
Figure 3.5. UV-Vis spectra for the reduction of 0.1 mM of **5** (black) by ferrocene in CH₃CN at room temperature, showing the formation of **6** at 585 nm. Inset: titration of ferrocene monitored at 420 nm (black) and 585 nm (red).
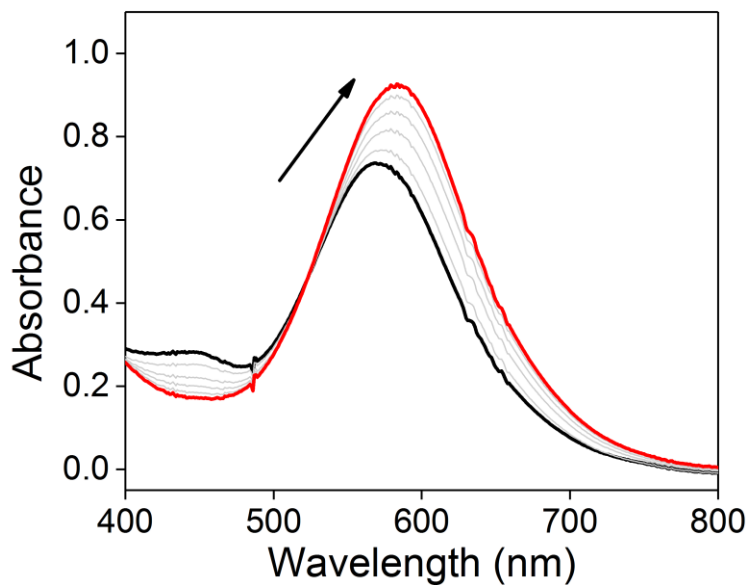
Figure 3.6. UV-Vis spectra for the conversion of 0.1 mM of **4** (black) with tetrabutylammonium nitrate to form **6** (red) in CH₃CN at room temperature.
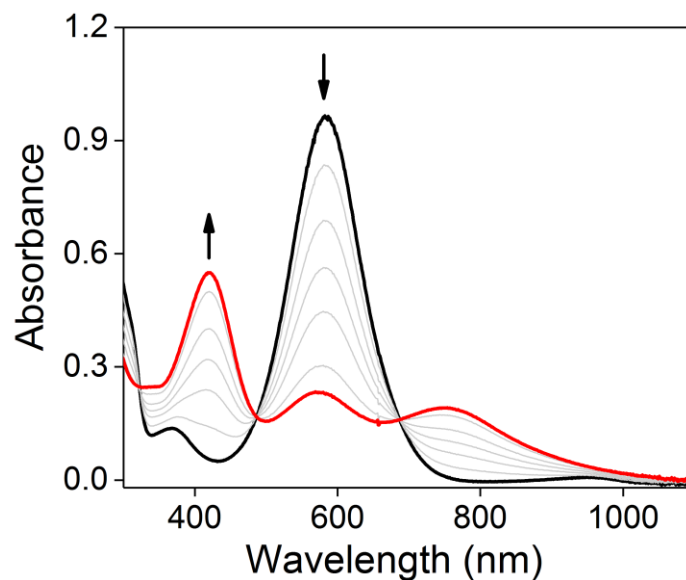
Figure 3.7. UV-Vis spectra for the oxidation of 0.1 mM **6** (black) to **5** (red) by 1 equivalent of CAN in CH$_3$CN at room temperature.

Complex **6** was synthesized when **4** reacted with 5 equivalent of sodium nitrate or tetrabutylammonium nitrate (TBANO$_3$) in DCM over a 3 h period (**Scheme 3.6**). We observed a color change of solution from a purple to a blue. Blue crystals of **6** were produced by layering pentane onto a filtered solution of **6** in DCM set aside in the refrigerator. A crystallized sample of **6** was analyzed with X-ray crystallography. The x-ray crystal structure of **6** is shown in **Figure 3.8**. X-ray crystallography analysis confirmed the Co(III) center in **6** is also a four coordinate with a similar square planar geometry as **4** with one nitrate ligand bound. The bonds in **6** are similar with bond lengths and angles found in **4**. From this analysis, the nitrate ligand bound in the axial position in **5** must dissociate from the cobalt center during the reduction reaction.

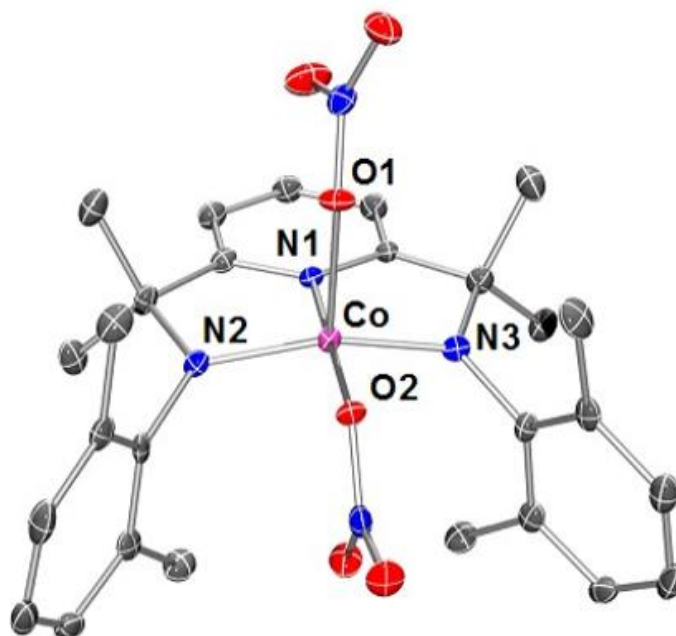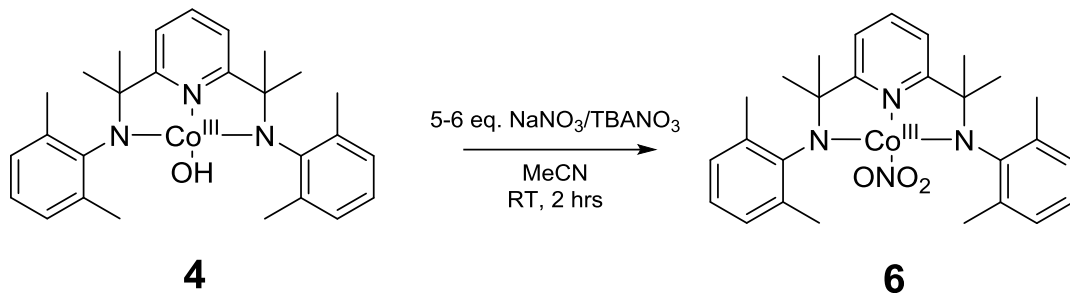**Scheme 3.6**. Ligand exchange of hydroxide to nitrate to generate **6**
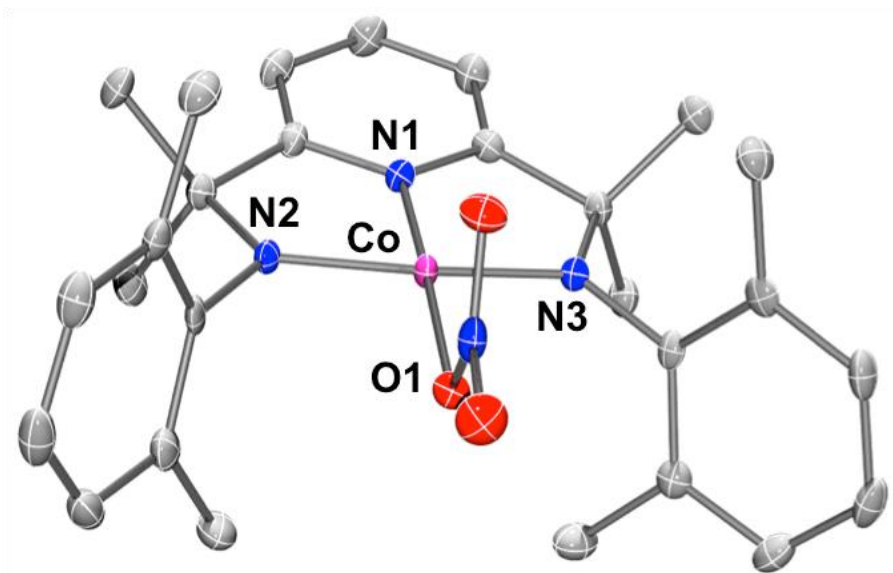
Figure 3.8. X-ray crystal structure of **6** with thermal ellipsoids drawn at 50% probability level. Hydrogen atoms have been omitted for clarity. Selected bond lengths and angles for one independent molecule in the unit cell: Co-N1 1.824 Å; Co-N2 1.788 Å; Co-N3 1.790 Å; Co-O1 1.929 Å.

To probe the electronic structure of **5**, further characterization was completed using EPR spectroscopy and DFT/CASSCF calculations. This data was collected by our collaborators at the University of Kansas by Yuri Lee and Prof. Timothy A. Jackson. The X-band EPR spectrum of **5** displayed a broad S = ½ signal at $g \approx 2.2$ (320 mT) at 30 K showing seven resolved hyperfine lines originating from the coupling of the unpaired electron spin with the ^{59}Co (I = 7/2) nucleus (**Figure 3.9**). The EPR spectrum of **5** was simulated using g_1

= 2.23, g_2 = 2.08, and g_3 = 2.00 and the hyperfine coupling constants A(^{59}Co) is simulated

with A_1 = 135, A_2 = 165, and A_3 = 320 MHz (**Figure 3.9**). The EPR signal observed for **5** does

not resemble any EPR signals when compared to the few reported examples of low-spin

d^5 Co(IV) complexes with a square pyramidal geometry.[82,93-96] This could be due to higher

spin density on the Co(IV) center in **5**.
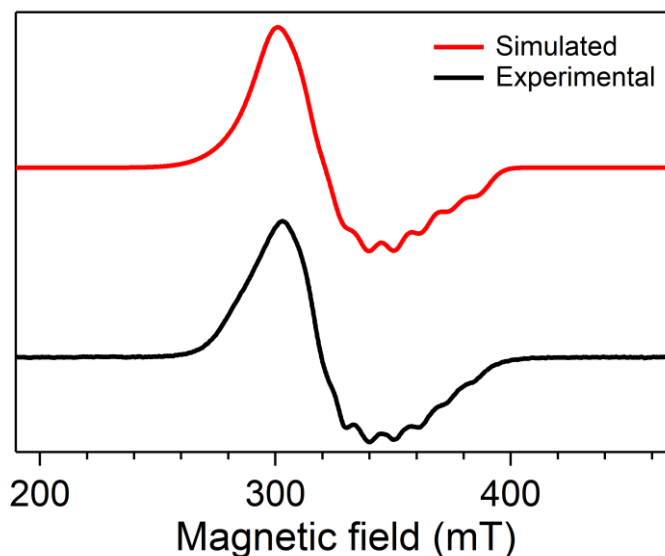
Figure 3.9. Perpendicular-mode X-band EPR spectrum of a 5 mM frozen solution of **5** in acetonitrile at 30 K (black) and simulation (red).

The electronic structure of **5** was examined using both DFT and CASSCF/NEVPT2

computations. Overall, the computational results found showed the DFT-optimized

structure (**Figure 3.10**) of **5** was in excellent agreement with the X-ray crystal structure of

5 (**Figure 3.4**).

	XRD	DFT
Co - O1	2.10	2.08
Co - O2	1.93	1.94
Co - N1	1.86	1.86
Co - N2	1.83	1.83
Co - N3	1.83	1.83
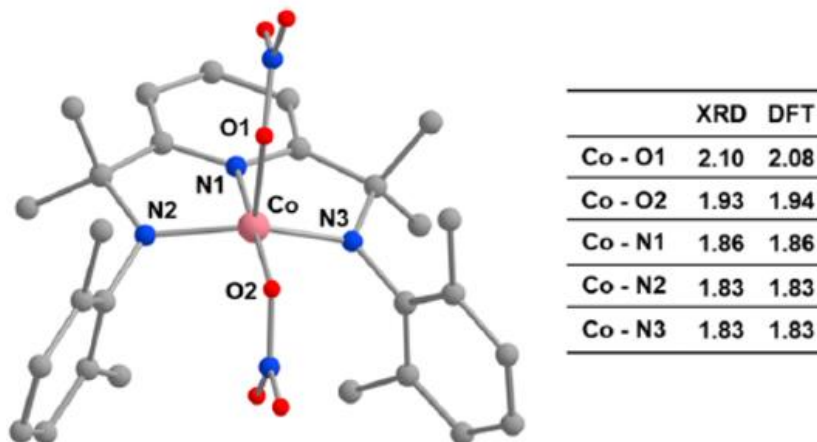
Figure 3.10. DFT-calculated structure of **5** with the corresponding bond distances (Å) compared to XRD bond distances (Å).

From DFT calculations, the d-orbital splitting pattern for complex **5** reflects the covalent interaction between the Co(IV) center and the N3 ligand (**Figure 3.11**). Following the conventional coordinate system, the z axis is along the axial Co-ONO$_2$ bond and the x and y axes lie along the equatorial Co-ligand bonds. The d_{xy}, d_{xz}, and d_{yz} orbitals are of π-type and the d_{z2} and d_{x2-y2} orbitals are of σ-type. The d_{xy} and d_{xz} orbitals have the weakest interactions with the ligand and minor interaction with the nitrate ligand. They are of lowest energy and doubly occupied. The d_{yz} orbital has strong π interactions with the anionic *N*-donors of the N3 ligand coupled with the weak nitrate ligand in the axial position placing them at a higher energy than the d_{z2} orbital. The d_{z2} orbital is the singly occupied molecular orbital (SOMO) and d_{x2-y2} orbital is at the highest energy which is σ-antibonding with the N3 ligand and the nitrate ligand in the equatorial position.
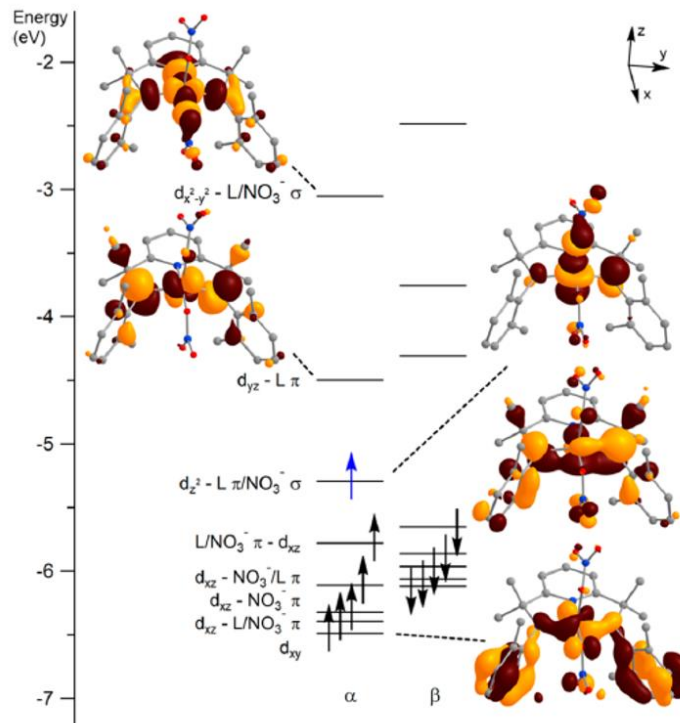
Figure 3.11. Co(IV) d-orbital splitting pattern for **5** from DFT computations. Surface contour plots of quasi-restricted orbitals are shown for each d-orbital.
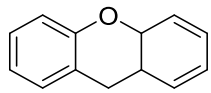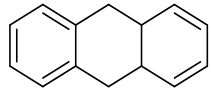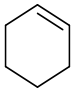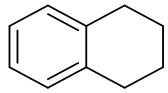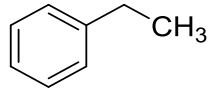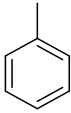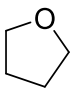
The computations offered more insight into the reactivity of **5** implying that the axial nitrate ligand will likely serve as the electron acceptor and the proton acceptor in the course of a hydrogen atom transfer (HAT) reaction. EPR and computational studies can be read more in depth in the literature.[91] After the spectroscopic and computational characterization of **5** was complete, we pursued to investigate the reactivity of its ability to activate sp^3 C-H bonds.

3.3.3 C-H Bond Cleavage Reactivity of Co(IV)-(ONO$_2$)$_2$ Complex

After structural information was obtained of **5**, the next step was to study how reactive the Co(IV) complex was towards C-H bonds. The first substrate that we studied was DHA with a bond dissociation energy (BDE) of 78 kcal/mol (**Table 3.2**). The addition of 250 mM DHA in DCM to a solution of 0.1 mM **5** in MeCN resulted in the disappearance

36

of the absorption band at 420 nm within a few minutes shown in **Figure 3.12**.

Simultaneously, the appearance of 585 nm band indicated that the reaction cobalt

product is Co^{III}-ONO_2, **6**. The recovery yield of **6** is 70-80% and is independent of O_2

present in the reaction. Another observation made is the sharp fine optical feature from

300-400 nm indicating the formation of anthracene as the oxidation product of DHA. The

formation yield of anthracene is 35% determined by GC-analysis, accounting for ~70% of

the oxidizing produced used. The formation yield of anthracene is also independent of

the amount of O_2 present in the solution. From the GC data collection, there were small

traces of anthrone and anthraquinone. These results suggest that **5** is a one-electron

oxidant.

Table 3.1 List of Substrates with BDE and their Structures

Substrate	BDE (kcal/mol)	Structure
Xanthene	76	
9,10-dihydroanthracene	78	
Cyclohexene	82	
1,2,3,4-tetrahydronaphthelene	85	
Ethylbenzene	87	
Toluene	90	
THF	92	
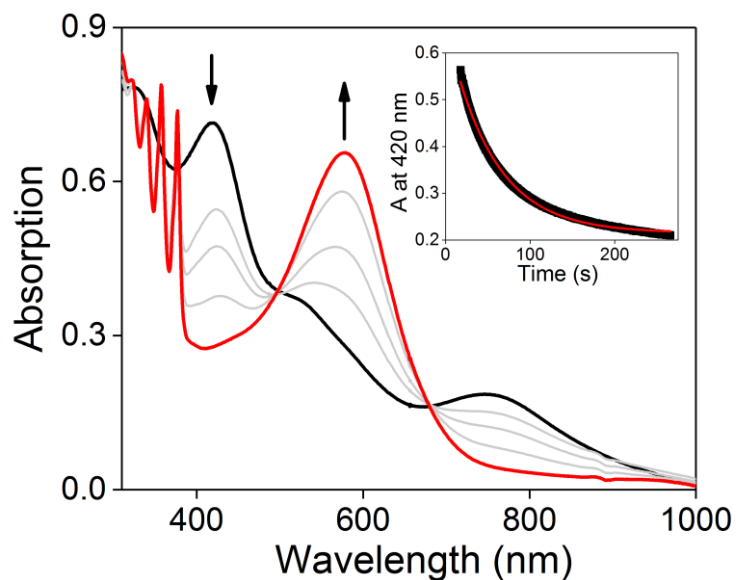
Figure 3.12. UV-Vis spectra of 0.1 mM of **5** (black) in the reaction with 250 mM DHA at RT. Inset: time trace of the absorption maximum at 420 nm, best fitted to a first-order exponential decay (red curve).

The kinetic trace at 420 nm for DHA oxidation was monitored and fitted using the first-order mode to obtain the pseudo-first-order rate constant (k_{obs}) at RT (**Figure 3.12, inset**). More oxidation experiments were conducted to obtain k_{obs} at various concentrations of DHA. The k_{obs} values obtained correlated linearly with the concentration of DHA allowing us to determine the second-order rate constant (k_2) of 0.079(3) $M^{-1}s^{-1}$ (**Figure 3.13**). We then conducted the experiment with DHA-d_4 as the substrate and a slower reaction was observed affording a k_2 of 0.034(2) $M^{-1} s^{-1}$. The H/D kinetic isotope effect (KIE) of 2.3 indicated that the cleavage of C-H bond by **5** is the rate-determining step for DHA oxidation.
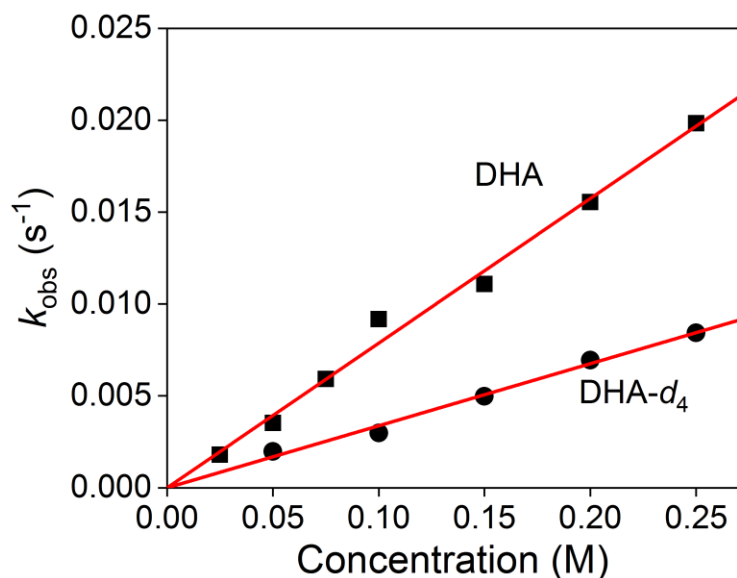
Figure 3.13. Plots of k_{obs} as a function of the concentration of (■) DHA and (●) DHA-d_4 obtained in MeCN/DCM at room temperature, fitted linearly.

We then extended our reactivity studies with other substrates with BDE values ranging from 76-87 kcal/mol. The substrates we studied include xanthene, cyclohexene (c-C_6H_{10}) , 1,2,3,4-tetrahydronaphthelene (tetralin), and ethylbenzene (PhEt) (**Table 3.1**). We conducted these oxidation experiments under similar conditions as we did for DHA and determined the k_2 values (**Table 3.2**). We observed that the rate constant becomes slower as the C-H bond being cleaved becomes stronger (**Figure 3.14**).

Table 3.2 Kinetic results for the reaction of **5** with substrates

Substrate	k_2 (M^{-1} s^{-1})	KIE
Xanthene	0.15(5)	3.3
Xanthene-d_2	0.047(6)	
DHA	0.079(3)	2.3
DHA-d_4	0.034(2)	
Cyclohexene	0.047(3)	Not determined
Tetralin	0.018(1)	Not determined
PhEt	0.0033(1)	5.4
PhEt-d_2	0.00061(1)	
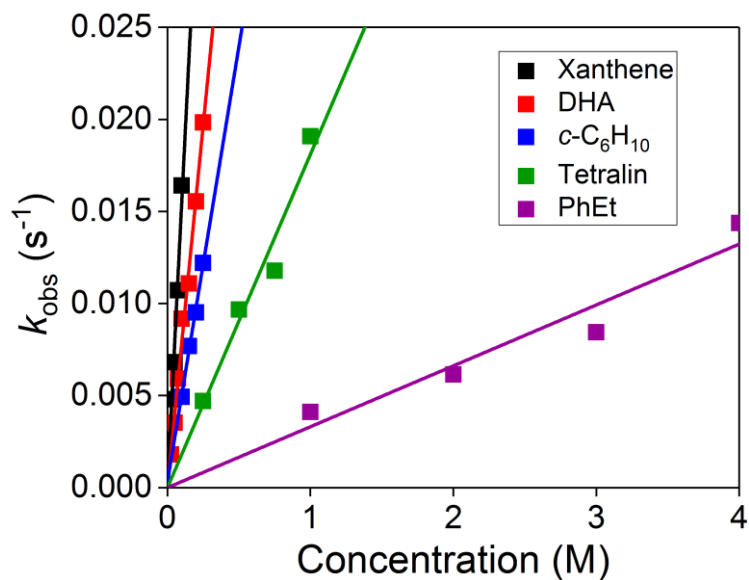
Figure 3.14. Plots of k_{obs} as a function of the substrate concentration for xanthene, DHA, cyclohexene, tetralin and ethylbenzene obtained in MeCN at room temperature, fitted linearly.

Additional experiments were conducted to determine the KIE for xanthene and ethylbenzene. Reacting xanthene with **5** afforded a k_2 of 0.15(5) $M^{-1}s^{-1}$ and a KIE of 3.3 on the left of **Figure 3.15**. The benzylic C-H bond of ethylbenzene represents the strongest bond that **5** can cleave with a BDE value of 87 kcal, affording a k_2 of 0.0033(1) $M^{-1}s^{-1}$ and a KIE of 5.4 on the right of **Figure 3.15.** From these additional experiments, H/D KIE values calculated provided more evidence that the cleavage of the C-H bond is the rate-determining step. Oxidation products of ethylbenzene include styrene and acetophenone determined through GC-analysis.
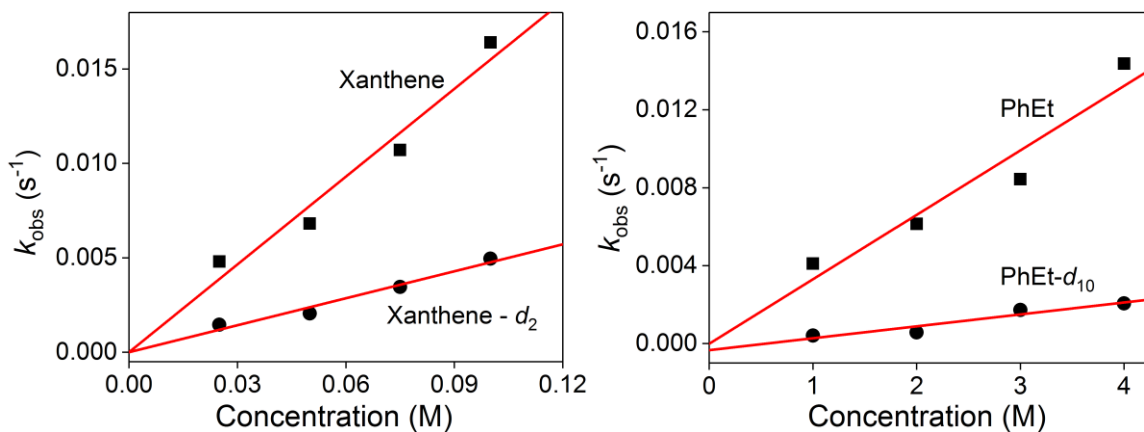
Figure 3.15. Left: Plots of k_{obs} as a function of the concentration of (■) xanthene and (●) xanthene-d_2 obtained in MeCN/DCM at room temperature, fitted linearly. **Right:** Plots of k_{obs} as a function of the concentration of (■) PhET and (●) PhEt-d_2 obtained in MeCN at room temperature, fitted linearly.

Eyring analyses were completed with DHA and ethylbenzene. DHA oxidation has a small activation enthalpy $\Delta H^{\neq}$ = 3.3 kcal/mol but a large activation entropy $\Delta S^{\neq}$ = -52.5 cal/mol●K (**Figure 3.16, left**). Whereas ethylbenzene oxidation has a big activation enthalpy $\Delta H^{\neq}$ = 15.1 kcal/mol but a small activation entropy $\Delta S^{\neq}$ = -22.3 cal/mol●K (**Figure 3.16, right**). We see the pattern where the oxidation for a substrate with a strong C-H bond has a larger activation enthalpy compared to a substrate with a weak C-H bond whereas we see the opposite in the overall activation free energy. We are unclear and are actively investigating, but we hypothesize that these analyses are consistent that the substrate oxidation is a bimolecular reaction.
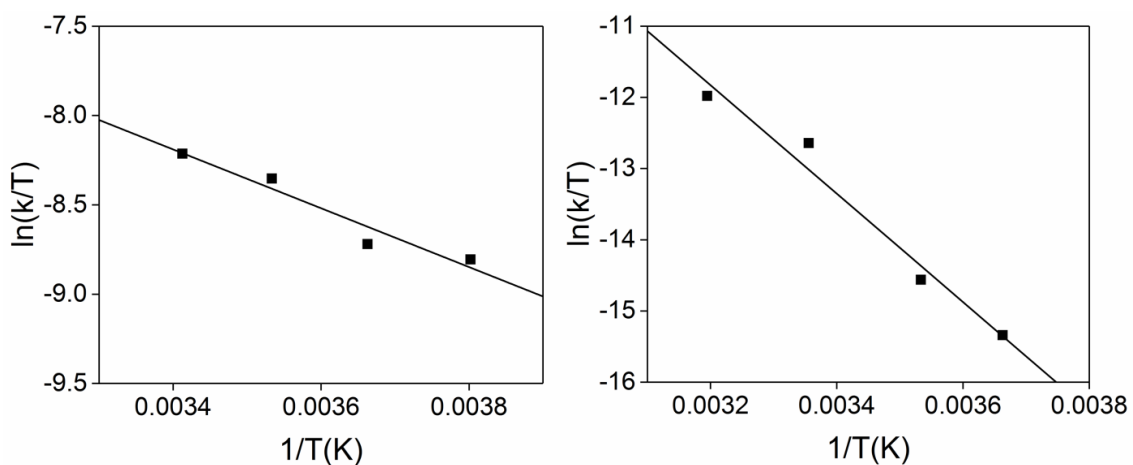
Figure 3.16. Left: Eyring plot of the reaction of **5** with DHA. **Right**: Eyring plot of the reaction of **5** with PhEt. The black line shows the linear fit of the data.

After all oxidation and Eyring experiments were completed, the log k_2' (k_2' is the normalized k_2 on a per hydrogen basis) correlates linearly with the strength of the C-H bond being cleaved with a slope of -0.13 (**Figure 3.17**). The slope that we defined of our Co(IV)-dinitrate species is less negative compared to the (13-TMC)Co^{IV}-O complex reported by Nam and co-workers, where their complex can cleave C-H bonds up to 80 kcal/mol (red) and their slope of -0.31.[55] Furthermore, comparison of slopes of BDE plots for a variety of metal-oxo and metal-nonoxo complexes (not just Co, but other late transition metals such as Mn, Fe, Ru, Ni, and Cu with oxidation states of +3 or +4) revealed that **5** is less sensitive to the C-H bond strength of the substrate where a typical slope ranges from -0.2 to -0.5 (**Table S9**).[55,66, 69,76,82,97-110]
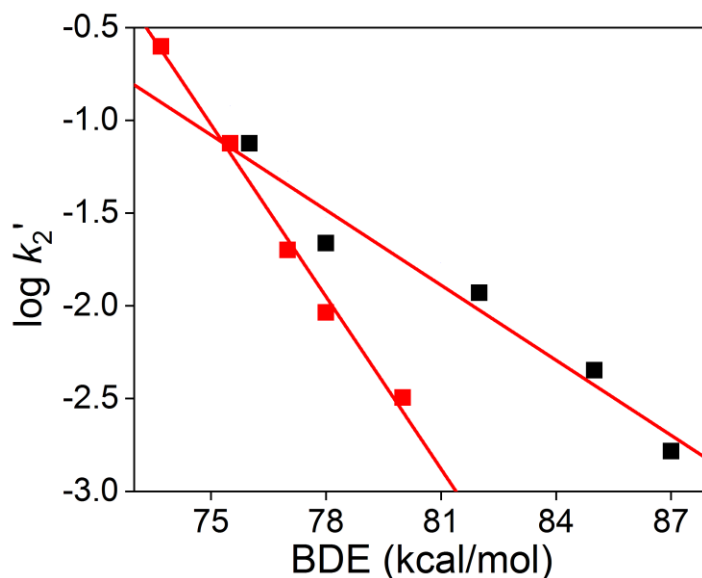
Figure 3.17. Plots of log k_2' as a function of C-H bond strength for substrate oxidation by **5** in acetonitrile at room temperature (black) and (13-TMC)Co^{IV}-O at -40° C (red, data from ref. 55) Lines represent the best linear fittings.

We observed another behavior when plotting the log k_2' as a function of C-H bond strength is the weaker substrates (73-80 kcal/mol) don't correlate linearly **(Figure 3.18, left).** 1,3-cyclohexadiene (1,3-c-C$_6$H$_8$), 1,4 cyclohexadiene (1,4-c-C$_6$H$_8$), and fluorene data points were omitted from **Figure 3.17**. We were interested in why this occurred with weaker C-H substrates compared to strong C-H substrates. Anderson and co-workers observed a similar behavior where their terminal Co(III)-O complex showed no linear correlation when plotting the log k_{obs} vs. BDE after conducting substrate oxidation experiments.[65] They did notice a linear correlation when plotting k_{obs} vs. pK_a concluding that their reaction is pK_a driven for the mechanism of proton transfer.[65] We took this observation and applied it to our data and noticed there is a definitive linear correlation between the rate of the C-H activation and the pK_a of weak substrates (**Figure 3.18, right**).

We are still currently investigating into this observation that could possibly help us understand more into the mechanism of proton transfer for our system.
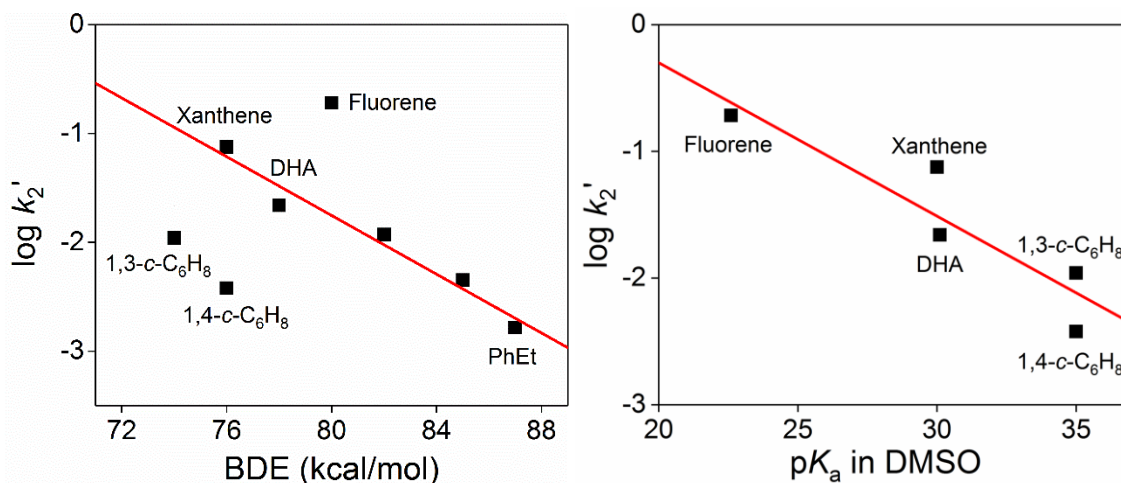
Figure 3.18. **Left.** Plots of log k_2' as a function of C-H bond strength for substrate oxidation by **5** in acetonitrile at room temperature. **Right.** Plots of log k_2' based on pK_a of substrates in DMSO. Lines represent the best linear fittings.

To gain more insight about the C-H bond reactivity of **5**, we ran electrochemical studies on **6**. As shown in **Figure 3.19**, the cyclic voltammogram (CV) of **6** exhibits an anodic peak at 0.67 V vs Fc with the cathodic peak at 0.43 V. The peak separation between the anodic and cathodic peaks of 0.24 V is much larger than 0.06 V which was expected for a reversible electron transfer. This phenomenon observed indicates that the redox process is coupled to the chemical reaction. This reaction is most likely the coordination/dissociation of the nitrate ligand in the axial position during the conversion of **6** to **5**. We assigned the mid-point potential (0.55 V vs. Fc) to be the Co(IV/III) couple.
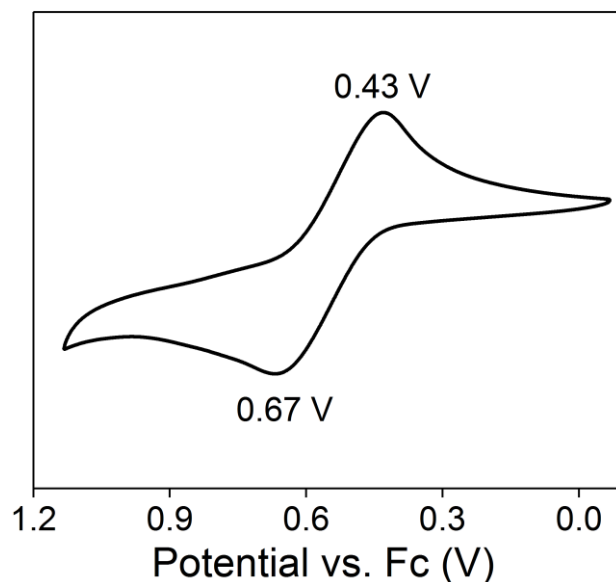
Figure 3.19. Cyclic voltammogram of **6** obtained in acetonitrile at room temperature with a scan rate of 0.1 V/s.

Further analysis was attempted to measure the pK_as of the nitrate ligands in **5**, but was unsuccessful. We used the pK_a value reported in literature of free nitrate anion in acetonitrile estimated roughly around 8.8.[111, 112] This value is considered to be on the upper end of the pK_a, as the coordination of the nitrate ligand to the Co(IV) center lowers the pK_a making it less basic. We have followed the protocol of Mayer in applying the Bordwell-Polanyi relationship to C-H bond oxidations by a set of metal-oxo complexes (**Eq. 3.1**),[113,114] we were able to estimate the $Co^{III}(OH)NO_2$ bond strength of the bound nitrate ligand that is protonated after the hydrogen-atom abstraction by **5** to be <84 kcal/mol. This value is consistent with our observation that **5** is able to cleave C-H bonds up to 87 kcal/mol.

$$D_{O\text{-}H} = 23.06E + 1.37\ pK_a + C \qquad (\textbf{Eq. 3.1})$$

Overall, we summarized the experimental and computational data collected by a proposed mechanism to clarify **5** and its reactivity towards C-H bonds (**Scheme 3.7**). The oxidation of **4** using a one-electron oxidant, CAN, generated **5** with the substitution of hydroxide by nitrate and the coordination of the second nitrate ligand. After the addition of a DHA (or any substrate), **5** cleaves the C-H bond of the substrate by hydrogen-atom transfer to generate a carbon radical and **6**. When Co(IV) is reduced to Co(III), one nitrate ligand must get protonated and dissociate from the cobalt center. The nitrate ligand in the axial position plays a role in the C-H bond cleavage process. As **5** is a one-electron oxidant, the classic radical rebound does not occur after the cleavage of the C-H bond. We hypothesized that the radical is likely oxidized by another molecule of **5** to generate the desaturated product or is trapped by O_2 in the solvent to form the oxygenated product(s).
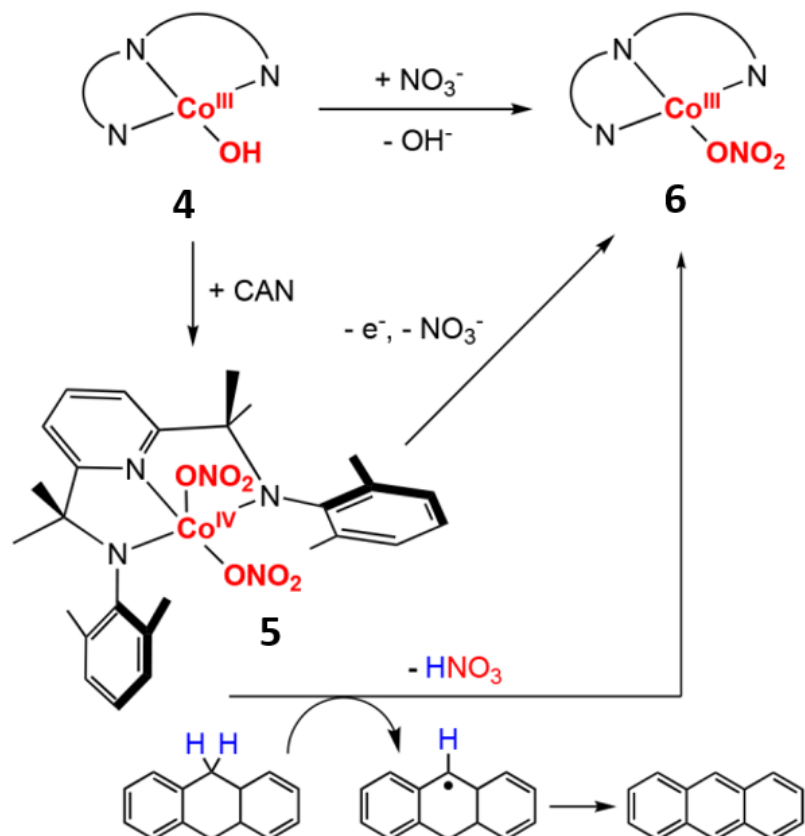
Scheme 3.7. Schematic illustration of the generation of **5** and its reactivity towards C-H bonds.

3.4 Preliminary Data on the Generation of a Co(IV)-Diazide Complex

After the generation of the Co(IV)-dinitrate species (**5**) and study of its reactivity

to cleave C-H bonds up to 87 kcal/mol, we wanted to investigate if a more reactive Co(IV)

species could be produced. From the X-ray crystal structure of **5**, the axial Co-ONO$_2$ bond

distance of 2.10 Å indicates a weak interaction between the cobalt center and the axial

ligand giving us motivation to replace the axial nitrate ligand with a more basic

coordinating anion (such as F$^-$ and N$_3^-$) to enhance the C-H bond activation reactivity. We

hypothesize that due to the weak interaction between the axial nitrate ligand and Co(IV)

center, that we can substitute that nitrate ligand with a more basic anion. Overall, we

expect to obtain a more reactive Co(IV) species. There have only been a few examples reported where a basic coordinating anion has the ability for radical rebound.[78, 115, 116]

To a solution of 0.1 mM **5** in MeCN, three equivalents of tetrabutylammonium azide (TBAN$_3$) was added into the solution at -40 °C, resulting in a new cobalt species, **7** (**Scheme 3.8**). We did attempt this reaction at RT, but it was too fast to obtain any spectra change. In **Figure 3.20**, we can see a shift of the 750 nm absorption band to 635 nm with the disappearance of the 420 nm absorption band. Titration of TBAN$_3$ into the solution of **5** suggested that two equivalents of TBAN$_3$ is sufficient to generate the new cobalt species, but three equivalents of TBAN$_3$ will fully convert this reaction. This observation indicates that not just one but maybe both nitrate ligands of **5** are replaced by azide. We hypothesize that the assignment of **7** to be a Co(IV)-diazide complex.
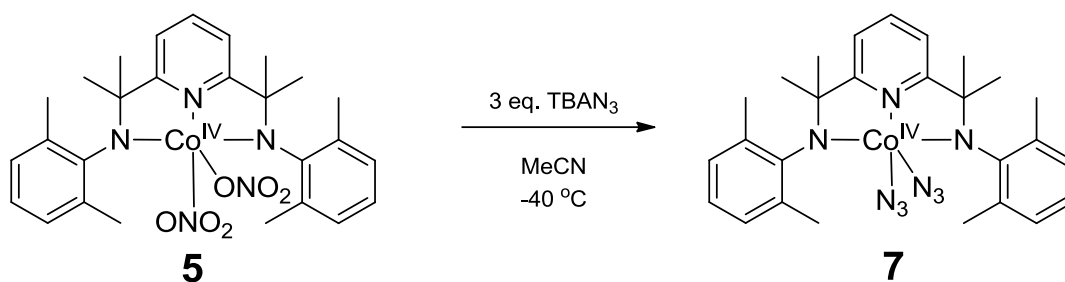
Scheme 3.8. Reaction of **5** with 3 equivalent of TBAN$_3$ to generate **7**
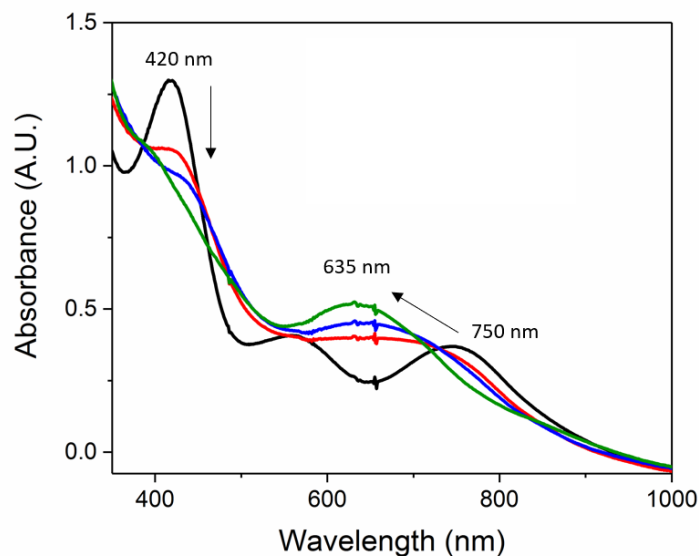
Figure 3.20. UV-Vis spectra of 0.1 mM **5** (black) after the addition of one (red), two (blue), and three (green) equivalents of tetrabutylammonium azide in acetonitrile at -40 °C.

Further characterization of **7** was obtained by EPR spectroscopy collected by our collaborators at the University of Kansas. Comparison of the hyperfine splittings in X-band EPR spectra of **7,** displaying a $S = \frac{1}{2}$ signal at $g \approx 2.0$ (~345 mT) and the EPR signal that **5** displayed at $g \approx 2.2$ (~325 mT) (**Figure 3.21**) show that they are distinct. Currently, simulation of **5** and more data collection are underway by our collaborators to obtain its g values and $A(^{59}\text{Co})$ hyperfine coupling constants.
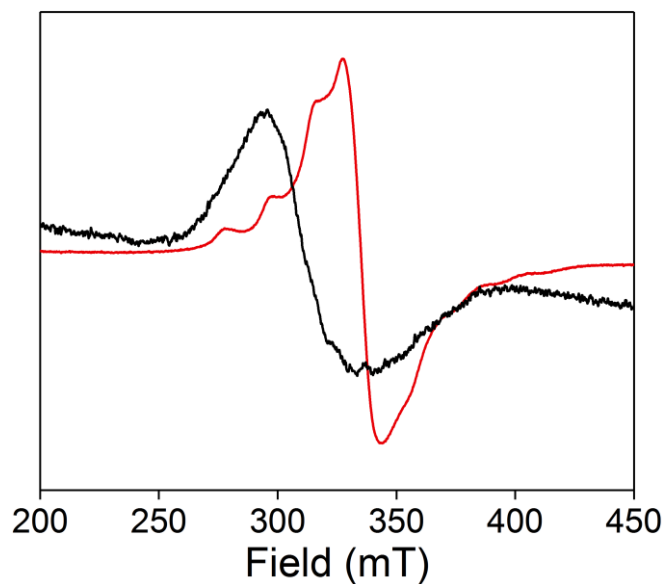
Figure 3.21. X-band EPR spectra of **5** (black) and **7** (red).

Compound **7** is only stable at cryogenic temperatures and decomposes rapidly at room temperature to Co(III) species. Due to the lower stability of **7**, we hypothesized that **7** is more reactive with C-H bonds than **5**. Indeed, at -10 °C, we were able to conduct DHA oxidation reactivity studies affording a k_2 of 0.17 $M^{-1} s^{-1}$ (**Figure 3.22**) which is higher than the k_2 of **5** (0.079 $M^{-1} s^{-1}$ at room temperature). These preliminary results provide strong support that replacing the nitrate ligand(s) with a more basic ligand will generate a more reactive Co(IV) species to promote C-H bond activation.
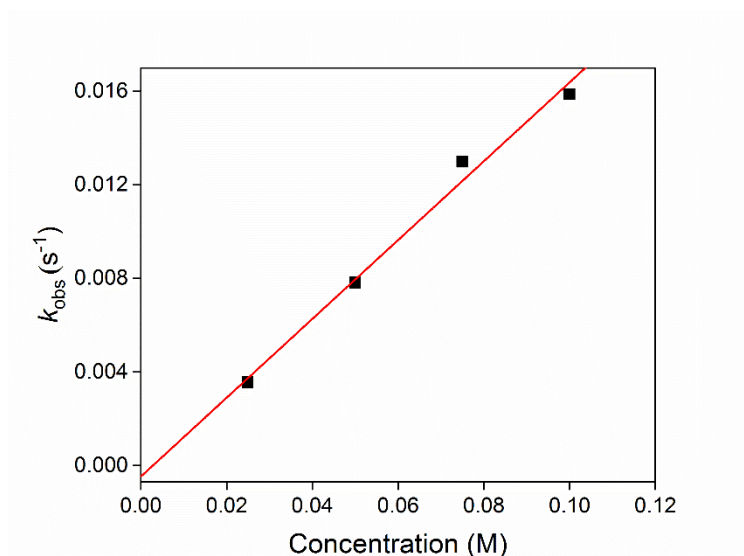
Figure 3.22. Plots of k_{obs} as a function of the concentration of DHA obtained in MeCN/DCM at -10 °C, fitted linearly.

3.5 Conclusions

In summary, we have successfully generated a novel, stable, mononuclear Co^{IV}-dinitrate complex supported by a di-anionic, tridentate ligand upon one-electron oxidation of the Co^{III}-OH starting complex. All complexes were fully characterized using spectroscopic and computational methods including X-ray crystallography, UV-Vis, EPR, and DFT and CASSCF calculations. Most importantly, our Co^{IV}-dinitrate complex is reactive to cleave sp^3 C-H bonds up to 87 kcal/mol in the condensed phase. We have also provided preliminary data that the replacement of the nitrate ligand(s) on the Co^{IV}-dinitrate complex with a more basic coordinating anion can afford a more reactive Co^{IV} species. Future work will continue to fully characterize this newly generate Co^{IV} species and study its reactivities with other substrates, and most importantly to determine if a radical rebound will occur.

During the investigation presented in Chapter 3, we recognized the nature of the N3 ligand scaffold to afford a high-valent Co^{IV} species. We were curious if we can apply the same application to generate a series of Nickel complexes. Chapter 4 will discuss the synthesis, characterization and the reactivity studies of a high-valent Ni(IV) species.

Chapter 4: Generation, Characterization, and Reactivity of a Mononuclear Nickel(IV)-Nitrate Complex

4.1 Preface

This chapter will describe the methods used for synthesis, characterization, and reactivity studies of a mononuclear Ni^{IV}-nitrate complex. This chapter includes work that is an unpublished, in progress manuscript. This manuscript is co-authored with Yuri Lee, Annie K. Schmautz, Prof. Dong Wang, and Prof. Timothy A. Jackson.

4.2 Introduction

Going beyond group 9, current examples of Ni or Cu complexes having an oxidation state of +4 are rare. For Ni and Cu complexes having an oxidation state of +3 is considered as "high-valent". Ni and Cu complexes of oxidations states +3 and higher are rare due to their thermal instability, challenging characterization, and unique reactivity compared to lower oxidation state species. There have been only been a handful of Ni^{III} and Cu^{III}- oxo and non-oxo complexes that exhibited reactivity as strong oxidants and hydrogen atom transfer agents.[66,68-71,74-78] It was reported that Ni(IV)-oxo complexes are involved in water oxidation and C-H bond cleavage.[50,52,53] To date, most Ni(IV) complexes reported are organometallic complexes.[117-120] There has been a rise in interest to generate high-valent Ni and Cu complexes. Herein, we report a rare and novel example of a high-valent Ni(IV) complex supported by the same N3 ligand of our recently reported Co(IV)-dinitrate analogue. This Ni(IV) complex was also capable of cleaving strong C-H bonds.

4.3 Results and Discussion

4.3.1 Synthesis and Characterization of Ni(II) and Ni(III) Complexes

We followed the procedure that was described in Chapter 3 when we synthesized

Co(II) and Co(III) complexes using the rigid, di-anionic, tridentate N3 ligand **L3** (**L3** = 2,6-

bis((2-2,6-dimethylphenylamino))isopropyl)pyridine).[90] We first synthesized Ni^{II}-py (**8**)

and Ni^{III}-py (**9**) complexes (**Scheme 4.1**). No characterization of complexes **8** and **9** were

completed as they were used immediately to synthesize starting complexes, Ni(III)-OH

(**10**) and Ni(III)-ONO$_2$ (**11**) (**Scheme 4.2**).
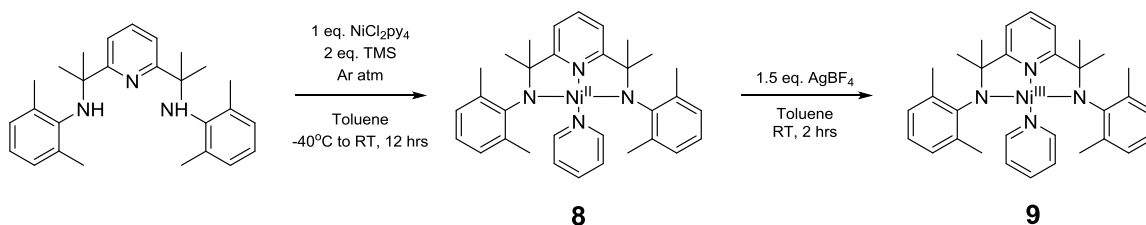
Scheme 4.1. Synthesis of Ni^{II}-py (**8**) and Ni^{III}-py (**9**)
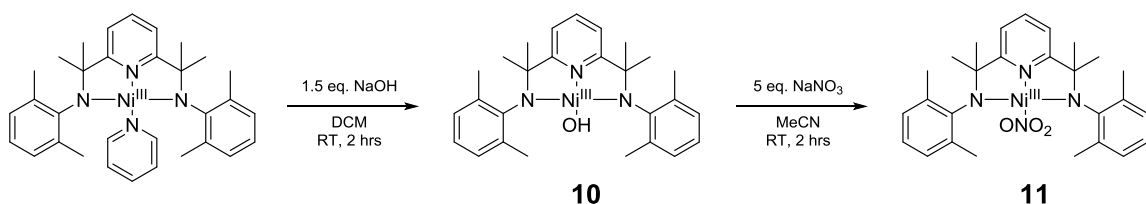
Scheme 4.2. Ligand exchange to generate Ni^{III}-OH (**10**) and Ni^{III}-ONO$_2$ (**11**)

Green crystals of **10** were obtained by layering pentane onto a filtered solution of

10 in DCM and set aside at room temperature. A crystallized sample of **10** was analyzed

with X-ray crystallography. The x-ray crystal structure of **10** is shown in **Figure 4.1**. The x-

ray crystal structure of **10** confirmed the Ni(III) center is four coordinate with a N3O ligand

set with a slightly distorted square planar geometry. The bonds of **10** are close to the bond lengths reported by the Co(III) analogues supported by the same N3 ligand.
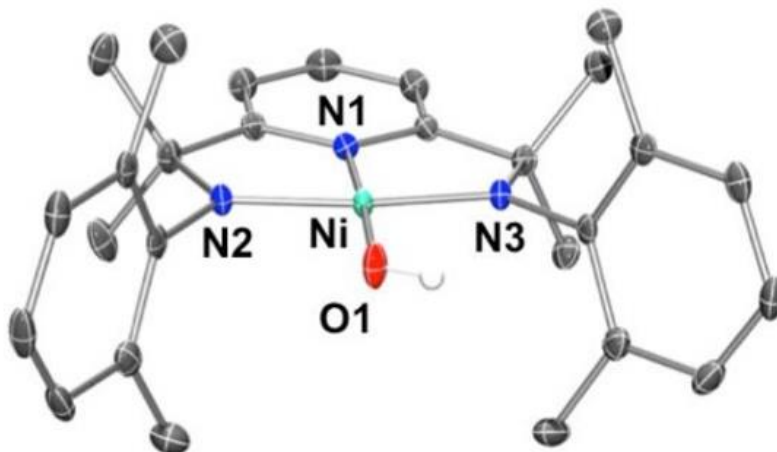
Figure 4.1. X-ray crystal structure of **10** with thermal ellipsoids drawn at 50% probability level. Hydrogen atoms (except the one on the hydroxyl group) have been omitted for clarity. Selected bond lengths for one independent molecule in the unit cell: Ni-N1 1.829 Å; Ni-N2 1.817 Å; Ni-N3 1.817 Å; Ni-O 1.829 Å.

There was no color change seen when hydroxide was substituted with nitrate to synthesize **11**. Green crystals of **11** were obtained by layering pentane onto a filtered solution of **11** in DCM and set aside in the refrigerator. A crystallized sample of **11** was analyzed with X-ray crystallography. The x-ray crystal structure of **11** is shown in **Figure 4.2**. The x-ray crystal structure of **11** confirmed the Ni(III) center is also a four coordinate with a slightly distorted square planar geometry, like **10** and the Co(III) analogues. The Ni-$O(NO_2)$ bond length is 1.889 Å, which is ~0.06 Å longer than the Ni-O(H) bond length in **10**. This is consistent with the hydroxide ligand having a stronger interaction with the Ni(III) center than the nitrate ligand due to its higher basicity. This observation is similar to our Co(III) complexes, **4** and **6**, where the Co-$O(NO_2)$ bond length is 1.929 Å, which is almost 0.14 Å longer than the Co-O(H) bond length.
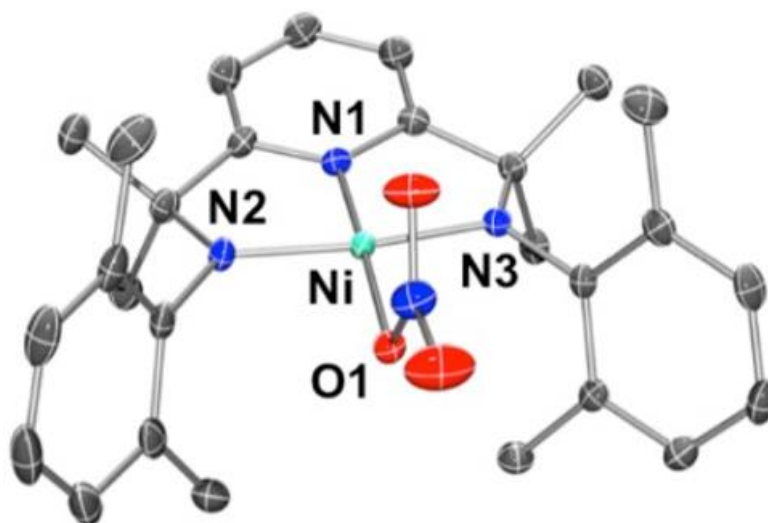
Figure 4.2. X-ray crystal structure of **11** with thermal ellipsoids drawn at 50% probability level. Hydrogen atoms have been omitted for clarity. Selected bond lengths of one independent molecule in the unit cell: Ni-N1 1.817 Å; Ni-N2 1.815 Å; Ni-N3 1.823 Å; Ni-O1 1.889 Å.

The UV-Vis spectra of **10** and **11** in CH_3CN were taken at room temperature exhibiting a strong absorption at 750 nm (ε = 4600 M^{-1} cm^{-1}) and 945 nm (ε = 5400 M^{-1} cm^{-1}), respectively (Figure 4.3). Compared to the Co(III) analogues, **4** and **6**, where there was a ~15 nm difference[91], the Ni(III) complexes, **10** and **11**, have a distinct difference of ~195 nm due to the higher sensitivity of the nickel center when bound to the hydroxide or nitrate ligand. Comparison of the Ni-$N_{py/amine}$ bond lengths, selected carbon-carbon and carbon-nitrogen of the N3 ligand bond lengths in **10** and **11** are similar to the bond lengths reported in the cobalt complexes from Chapter 3 (**Table S8**).
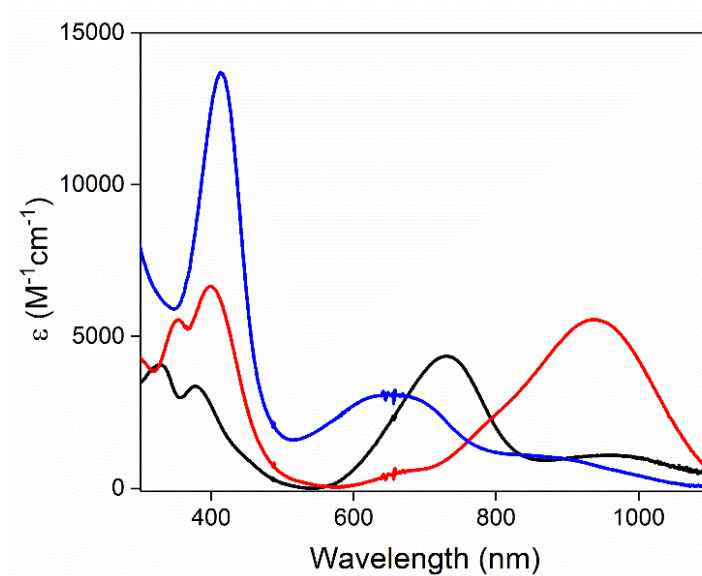
Figure 4.3. UV-Vis spectra of **10** (black), **11** (red), and **12** (blue) obtained in acetonitrile.

The absorption band at 945 nm for **11** resembles the absorption band of the Ni^{III}-ONO_2 complex (890 nm, ε = 4600 M^{-1} cm^{-1}) reported by McDonald and co-workers[68], supported by the **L1** ligand (described in Chapter 2). Further characterization of **11** was done using EPR spectroscopy collected by our collaborators at the University of Kansas. The X-band EPR spectrum of **11** exhibited an S = ½ signal at $g \approx$ 2.1 (325 mT), consistent with a d^7 Ni(III) complex (**Figure 4.4**). The results demonstrated that **11** has a much greater thermal stability compared to McDonald's Ni(III)-ONO_2 complex, indicating that our N3 ligand scaffold is capable of stabilizing high-valent states of late transition metals.
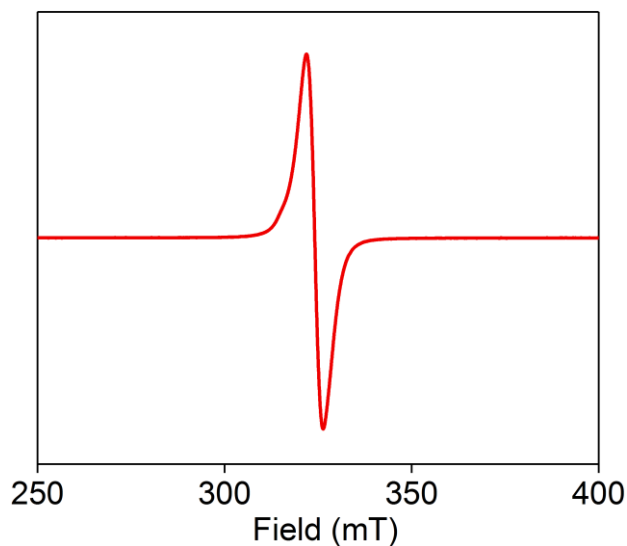
Figure 4.4. X-band EPR spectrum of a 5 mM frozen solution of **11** in acetonitrile at 10 K.

4.3.2 Generation and Characterization of a Mononuclear Ni(IV) Complex

The next step after obtaining structural information of our starting complexes, **10** and **11**, was to oxidize the Ni(III) center by one electron (**Scheme 4.3**). To a solution of **11** in CH_3CN, one equivalent of CAN in CH_3CN was added at 0 °C, resulting in a generation of a new nickel species, **12** (**Figure 4.3**). This reaction was taken at lower temperatures as the generated Ni species is unstable and more reactive at RT compared to our cobalt complexes. In the UV-Vis spectra, we can immediately see a decrease in absorption at 945 nm with the appearance of a new absorption band at 412 nm (ε = 2600 M^{-1} cm^{-1}) (**Figure 4.5**) One isosbestic point at 750 nm was observed indicating that no other intermediate was involved in the generation of **12**. The band at 412 nm exhibited by **12** resembles that of our Co(IV)-dinitrate complex (**5**) at 420 nm.[91] The stoichiometry of **11** and CAN was determined by titration experiments and was found to be 1:1 (**Figure 4.5, inset**). From these titration experiments, the addition of excess CAN did not cause a higher formation yield of **12**, indicating that **12** is indeed a Ni(IV) species. Alternatively, as this reaction

resembles what we saw from our Co complexes, **12** can be generated using **10** as the starting Ni(III) complex when reacted with one equiv. of CAN.
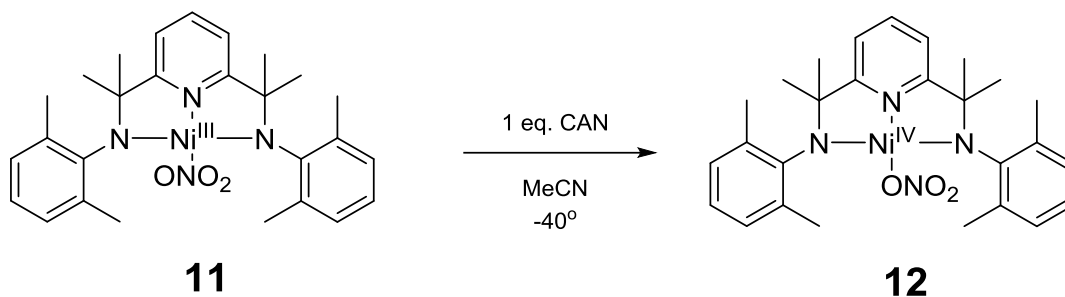
Scheme 4.3 Reaction of **11** with 1 equivalent of CAN to generate **12**
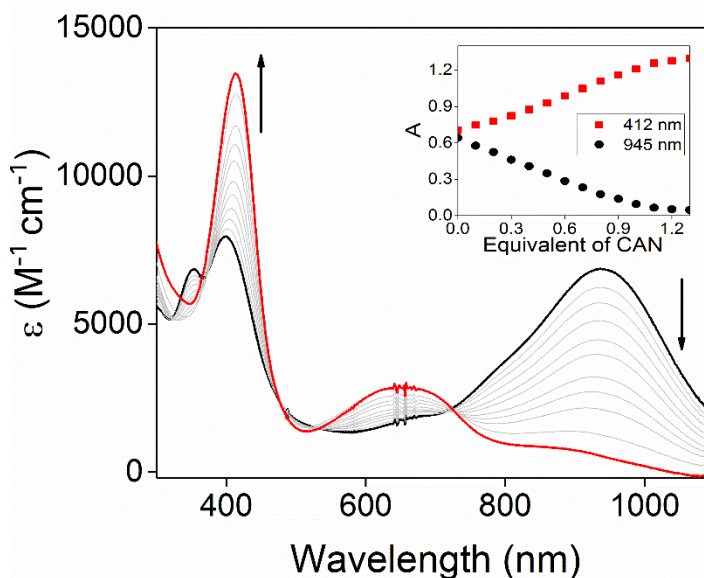
Figure 4.5. UV-Vis spectra for the conversion of **11** (black) to **12** (red) by one equivalent of CAN in acetonitrile at 0 °C. Inset: titration of CAN monitored at 945 nm (black) and 412 nm (red).

After the generation of **11**, we conducted an experiment to reduce **12** by Fc to regenerate a Ni(III) species. To a solution of **12** in CH_3CN, one equivalent of Fc in CH_3CN was added to the solution generating **11** (not **10**), suggesting that the **12** contains a coordinating nitrate ligand (**Figure 4.6**). Titration of Fc to the solution of **12** (**Figure 4.6,**

inset) revealed the formation yield of **12** to be 90 %. These observations are similar to what we observed with the cobalt complexes described in Chapter 3. At this time, we hypothesized that the coordinating anion(s) bound to Ni(IV) center is a nitrate ligand.
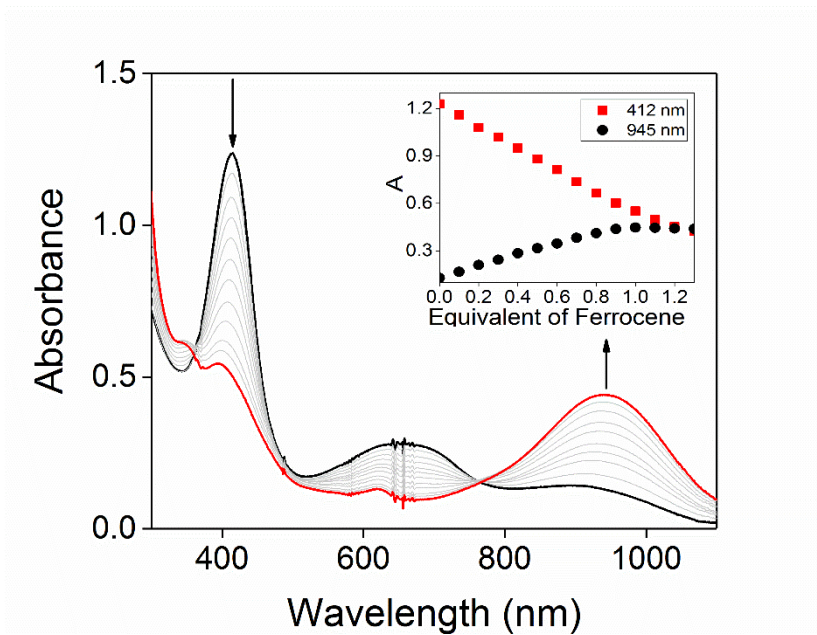
Figure 4.6. UV-Vis spectra for the reduction of 0.09 mM **12** (black) by ferrocene in acetonitrile at 0 °C, showing the formation of **11** at 945 nm. Inset: titration of ferrocene monitored at 945 nm (black) and 412 nm (red).

We ran electrochemical studies on **11.** As shown in **Figure 4.7**, the CV of **11** exhibits an anodic peak at 0.57 V vs Fc with the cathodic peak at 0.49 V. The CV showed a quasi-reversible redox couple allowing us to assign the mid-point potential (0.53 V vs. Fc) to be the Ni(IV/III) couple suggesting that **11** can be oxidized to generate its higher valent derivative, **12**.

61
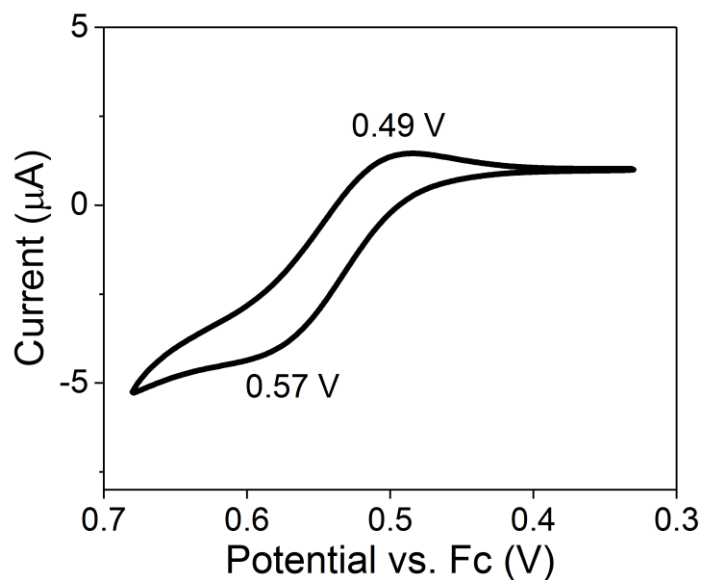
Figure 4.7. Cyclic voltammogram of **11** obtained in acetonitrile at room temperature with a scan rate of 0.1 V/s.

We found that **12** has a lifetime of ~1 hour at 0 °C, which only allowed us to characterize **12** at cryogenic temperatures. To obtain structural information of **12**, we attempted to grow crystals of **12**. After multiple attempts and change of solvents, we were unsuccessful to obtain crystals that were suitable for X-ray diffraction. Due to its short lifetime, we see a red/orange power formed indicating it's the decayed product of **12**. This decayed product can be isolated but cannot be characterized as it is not soluble in organic solvents. Due to the failed attempts of crystallizing **12**, we went an alternative direction by conducting low temperature ^{1}H NMR experiments to obtain structural information of **12**.

The ^{1}H NMR spectrum of **12** (**Figure 4.8**) was taken at -35 °C showing that **12** is a diamagnetic species. The spectrum is consistent with the assignment of $S = 0$ d^6 Ni(IV) center. The presence of two sharp singlets at 2.23 and 1.81 ppm corresponding to the benzylic and isopropyl methyl protons, respectively, suggests that complex **12** has a C_2

62

symmetry along the N_{py}-Ni bond. This gives us more evidence that **12** is likely a four-coordinated Ni(IV) complex with a square planar geometry similar to its Ni(III) derivatives, **10** and **11**. Due to the high reactivity of **12** even at low temperatures, we can see in the ^{1}H NMR that slowly over time, we see peaks that are labelled as the decay product(s).
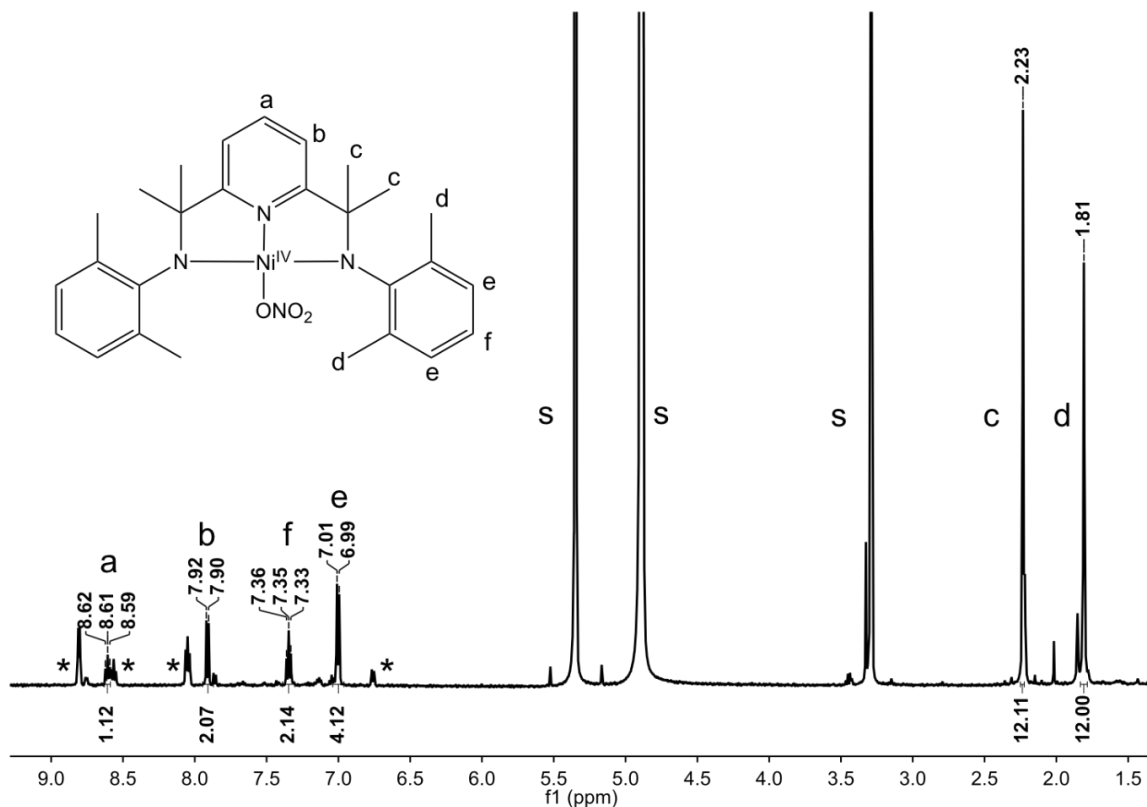
Figure 4.8. ^{1}H NMR spectrum of 1 mM **12** taken in CD_2Cl_2/CD_3OD at -35 °C. Solvent peaks are labeled at "s". Peaks labeled with * are from its decay product(s).

As CAN is both a one-electron oxidant and a good source of nitrate, we confirmed our hypothesis and assigned **12** as a Ni^{IV}-ONO_2 complex. This assignment is consistent with the chemical reversibility shown in the conversion of **11** to **12** and the quasi-reversibility observed in our electrochemical studies of **11.** This assignment is in

accordance with the Co(III)-ONO$_2$ (**6**), as **12** is isoelectronic to **6** (square planar geometry) described in Chapter 3.

As we were unsuccessful in obtaining crystals of **12** suitable for X-ray diffraction, we recently received preliminary computational studies of the electronic structure of **11** and **12** using DFT from our collaborators at the University of Kansas. The computational results found showed the DFT-optimized structure (**Figure 4.9**) of **12** contains a square planar Ni(IV) center. DFT structures of **11** and **12** have similar features (**Figure 4.9**). The Ni-N$_{py}$ bond length in **12** is similar to that for **11**, but the Ni-N$_{amido}$ bond distances are contracted by 0.02 Å in **12**. The Ni-ONO$_2$ bond distances in both **11** and **12** are the same.

Ni–N1	1.82 Å
Ni–N2	1.82 Å
Ni–N3	1.82 Å
Ni–O	1.90 Å

11

Ni–N1	1.83 Å
Ni–N2	1.80 Å
Ni–N3	1.80 Å
Ni–O	1.90 Å

12
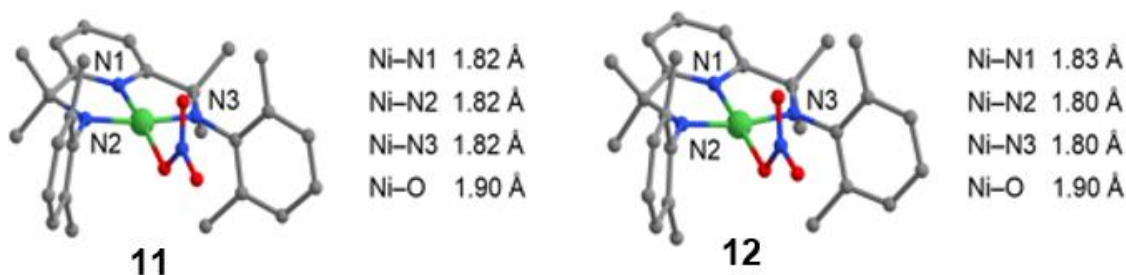
Figure 4.9. DFT-optimized structure of **11** and **12**. Green, red, blue and gray represent Ni, oxygen, nitrogen, and carbon atoms, respectively. Selected bond distances are shown next to each structure.

From the preliminary DFT calculations, the d-orbital splitting pattern for **11** and **12** are very similar and reflects the interaction between the Ni center and the N3 ligand (**Figure 4.10**). Following the conventional coordinate system, the x and y axes lie along the equatorial Ni-ligand bonds. The d$_{xy}$, d$_{xz}$, and d$_{yz}$ orbitals are of π-type and the d$_{z2}$ and d$_{x2-y2}$ orbitals are of σ-type. The molecular orbitals (MOs) of both **11** and **12** show the d$_{xy}$ orbital is of lowest energy where the d$_{x2-y2}$ orbital is of highest energy due to the strong σ

Ni-ligand antibonding interactions. For **11**, d_{yz} orbital represents the SOMO as there is π-antibonding interaction between the Ni d_{yz} orbital and the *N*-amide donors of the ligand $2p_z$ orbitals. This interaction shows greater ligand character implying there is inverted bonding. This feature of inverted bonding was able to identify that the d_{yz} orbital is of higher energy to d_{z2} and d_{xz} MOs. For **12**, the splitting pattern resemble **11**, where also the d_{yz} orbital lies below the d_{x2-y2} orbital where the calculations showed that there was predominant ligand character implying that it is of lower energy and doubly occupied. The Ni-ligand π-interactions in the d_{yz} orbital also showed inverted bonding that was observed for **11**. Due to the ligand-dominated character, the d_{yz} orbital is unoccupied in **Figure 4.10**, making this MO redox-active in the conversion of **11** to **12**. Calculations are still underway, but overall the DFT computations for **12** shows interesting results where there are four doubly-occupied MOs which is consistent with a Ni^{II} (d^8) description but the Ni character in the unoccupied d_{yz} MO does indicate there is some Ni^{IV} (d^6) character. These calculations are still in progress.
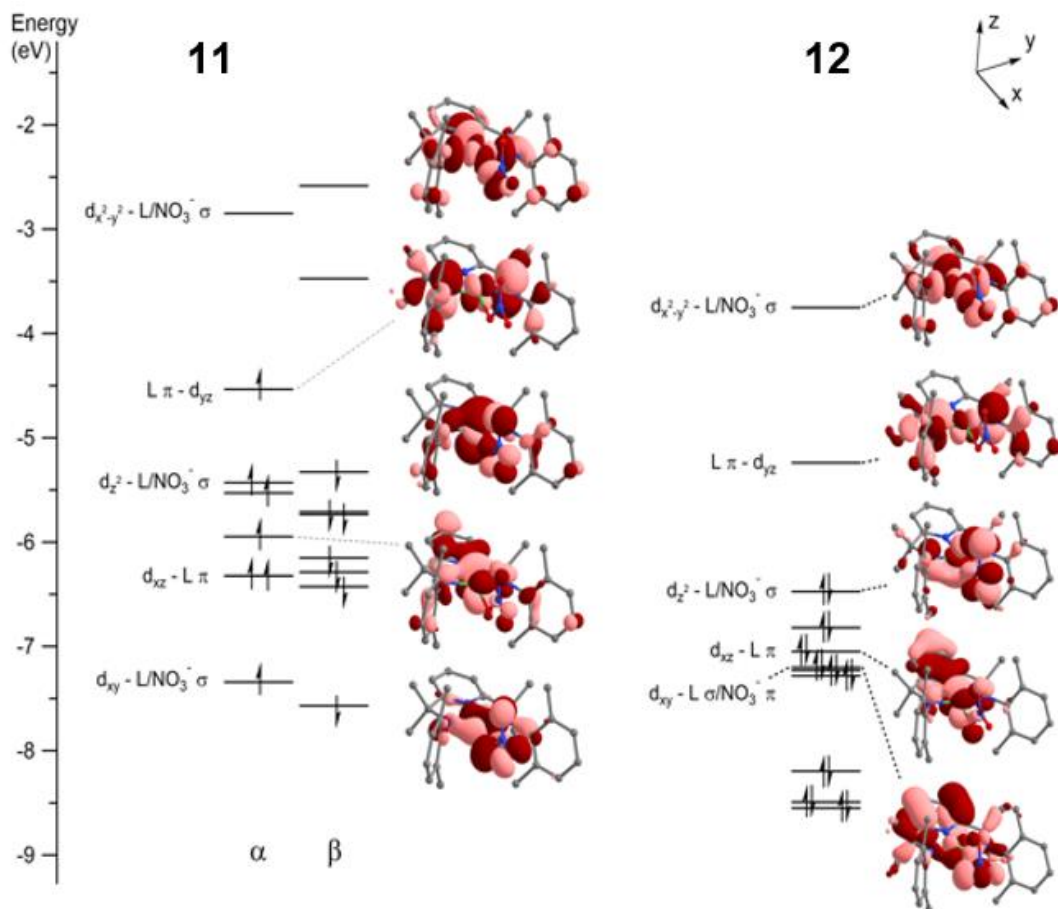
Figure 4.10. D-orbital splitting pattern for **11** and **12** from DFT computations. Surface contour plots of selected orbitals are shown (contour value = 0.03). Hydrogen atoms are omitted for clarity in (A) and (B).

Further characterization of **12** was done by X-ray absorption spectroscopy. At the time of writing this dissertation, XAS data collection was completed, and data analysis for both XAS and DFT is currently underway by our collaborators at the University of Kansas.

4.3.3 C-H Bond Cleavage Reactivity of Ni(IV)-ONO$_2$ Complex

Reactivity studies involving Ni(IV)-ONO$_2$ (**12**) with substrates was investigated. The first substrate that we studied was DHA. To a solution of 0.06 mM **12** in MeCN, 200 mM DHA in DCM was added resulting in the disappearance of the absorption band at 412 nm within a few minutes shown in **Figure 4.11**. Simultaneously, the appearance of the 945

nm absorption band indicates the reaction product is Ni(III)-ONO$_2$, **11**. Another observation seen is the optical feature from 300-400 nm indicating the formation of anthracene. The formation yield of anthracene is 50% determined by GC-analysis, suggesting that the use of the oxidizing equivalent is near quantitative, however, the recovery yield of **11** is ~42%. The low yield that we calculated could be due to the decomposition of **11** caused by the protons produced after hydrogen atom transfer. These results suggest that **12** is a one-electron oxidant.
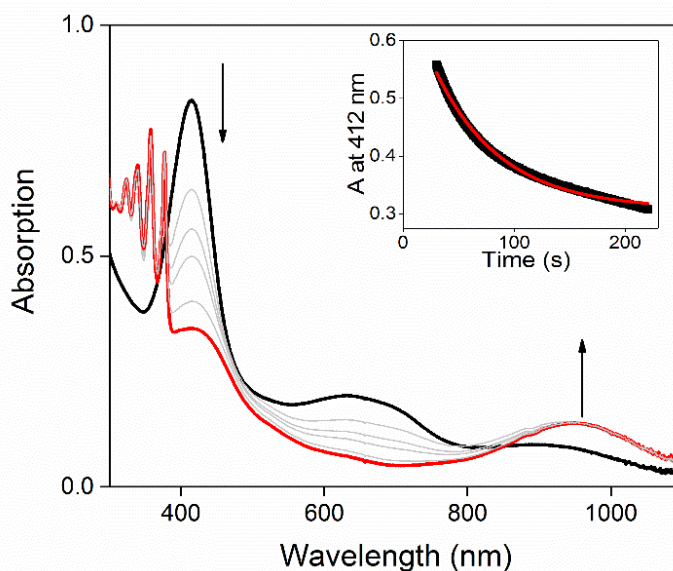
Figure 4.11. UV-Vis spectra of 0.06 mM **12** (black) in the reaction with 200 mM DHA at 0 °C. Inset: time trace of the absorption maximum at 412 nm, best fitted to a first-order exponential decay (red curve).

The kinetic trace of 412 nm for DHA oxidation was monitored and fitted using the first-order mode to obtain the k_{obs} at 0 °C (**Figure 4.11, inset**). We conducted more oxidation experiments to obtain k_{obs} values at different concentrations. The k_{obs} values obtained correlated linearly with the concentration of DHA to define k_2 of 0.12(8) M^{-1} s^{-1} at 20 °C and 0.057(8) M^{-1} s^{-1} at 0 °C. A slower reaction was observed with DHA-d_4 used as

a substrate, affording a k_2 of 0.012(7) M^{-1} s^{-1} at 0 °C (**Figure 4.12**). The H/D KIE of 4.6 indicates that the cleavage of C-H bond by **12** is the rate determining step for DHA oxidation.

Eyring experiments (**Figure 4.13**) were conducted for DHA and ethylbenzene. DHA oxidation has a small activation enthalpy $\Delta H^{\neq}$ = 5.1 kcal/mol but a large activation entropy $\Delta S^{\neq}$ = -45.2 cal/mol●K (**Figure 4.13, left**) and for ethylbenzene oxidation has a big activation enthalpy $\Delta H^{\neq}$ = 11.7 kcal/mol but a small activation entropy $\Delta S^{\neq}$ = -31.6 cal/mol●K (**Figure 4.13, right**). From the oxidation experiments and Eyring analyses, we see a similar behavior between both the Co(IV)-dinitrate complex (**5**) and the Ni(IV)-nitrate complex (**12**).
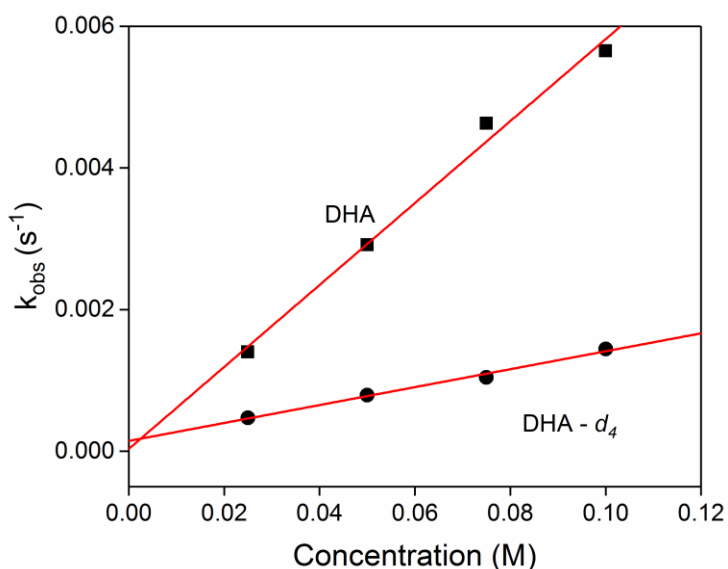
Figure 4.12. Plots of k_{obs} as a function of the concentration concentration of (■) DHA and (●) DHA-d_4 obtained in MeCN/DCM at 0 °C, fitted linearly.
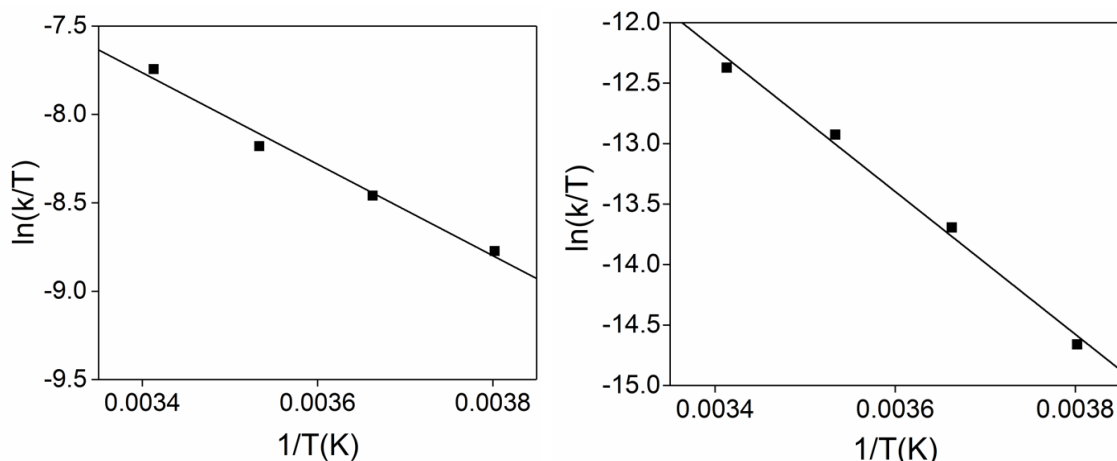
Figure 4.13. Left: Eyring plot of the reaction of **12** with DHA. **Right**: Eyring plot of the reaction of **12** with PhEt. The black line shows the linear fit of the data.

We extended our reactivity studies with other substrates with BDE values ranging from 76-92 kcal/mol. The substrates include xanthene, cyclohexene, PhET, toluene (PhMe), and tetrahydrofuran (THF) (**Table 3.1**). We conducted these oxidation experiments under similar conditions that we did for DHA and determined the k_2 values (**Figure 4.14**, **Table 4.1**). A similar observation is seen that the rate constant becomes slower as the C-H bond being cleaved becomes stronger.

Additional experiments were conducted to determine the KIE for xanthene, ethylbenzene, toluene, and THF. For this group of substrates, the H/D KIE values fall in the range of 3.8-9.2. Compared to Co^{IV}-dinitrate complex (**5**) where it could cleave a C-H bond up to 87 kcal/mol, the C-H bond of THF (BDE = 92 kcal/mol) represents the strongest one that **12** can cleave affording a k_2 = 0.0033(7) $M^{-1} s^{-1}$ and a KIE of 6.5. Oxidation products were determined through GC-analysis of ethylbenzene and toluene include acetophenone and THF include furanol and butyroactone. Unfortunately, no unsaturated products were determined.
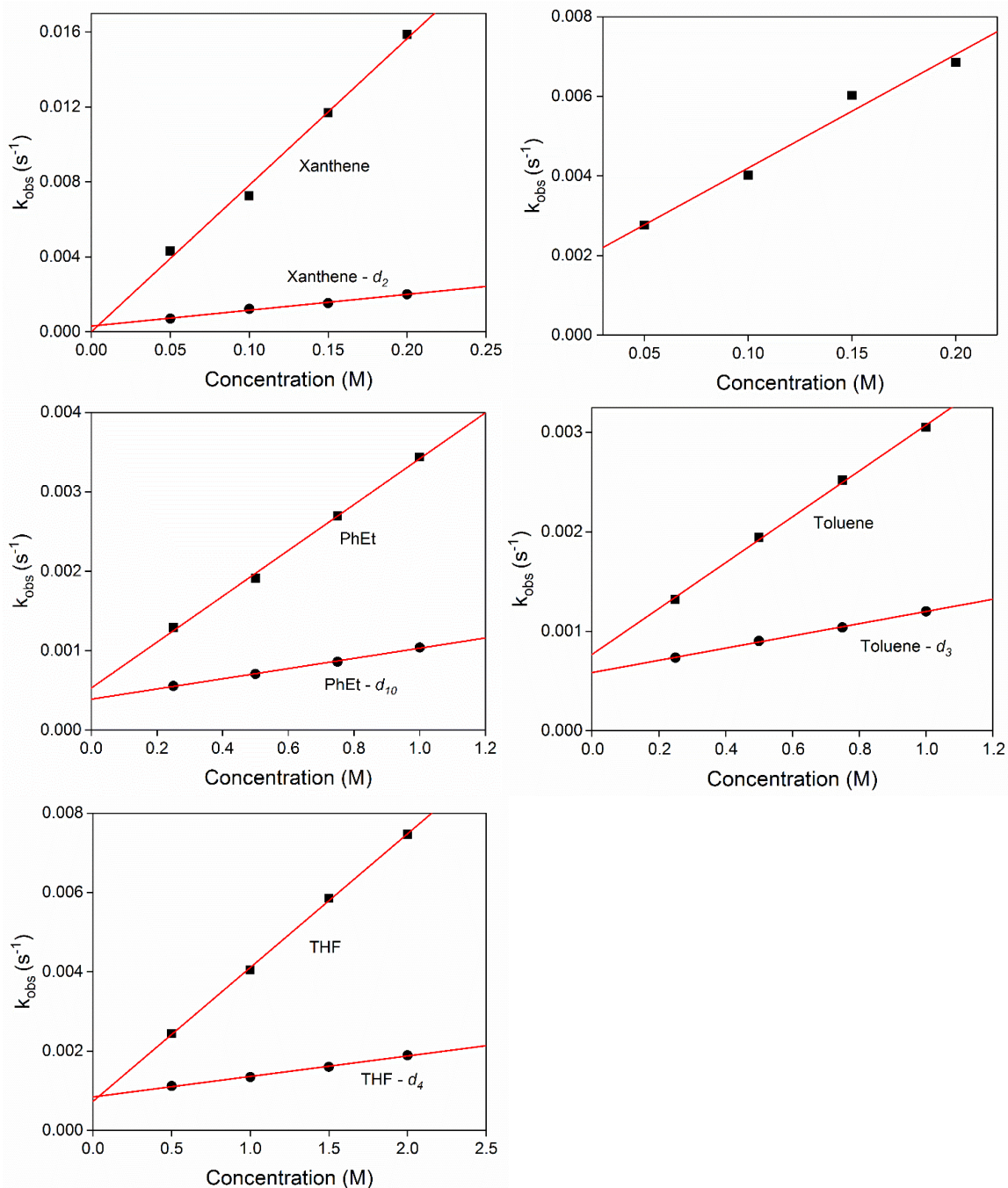
Figure 4.14. **Top Left:** Plots of k_{obs} as a function of the concentration concentration of (■) xanthene and (●) xanthene-d_2 obtained in MeCN/DCM at 0 °C, fitted linearly. **Top Right:** Plot of k_{obs} as a function of the concentration of cyclohexene obtained in MeCN at 0 °C, fitted linearly. **Center left:** Plots of k_{obs} as a function of the concentration of (■) PhET and (●) PhEt-d_2 obtained in MeCN at 0 °C, fitted linearly. **Center Right:** Plots of k_{obs} as a function of the concentration concentration of (■) PhMe and (●) PhMe-d_3 obtained in MeCN at 0 °C, fitted linearly. **Bottom:** Plots of k_{obs} as a function of the concentration concentration of (■) THF and (●) THF-d_4 obtained in MeCN 0 °C, fitted linearly.

Table 4.1 Kinetic results for the reaction of **12** with substrates

Substrate	k_2 (M^{-1} s^{-1})	KIE	T (°C)
Xanthene	0.078(2)	9.2	0
Xanthene-d_2	0.0084(6)		0
DHA	0.053(5)	4.6	-10
	0.057(8)		0
	0.079(4)		10
	0.12(8)		20
DHA-d_4	0.012(7)		0
Cyclohexene	0.028(8)	Not determined	0
PhEt	0.0083(9)	6.9	0
PhEt-d_2	0.0012(1)		0
PhMe	0.0023(1)	3.8	0
PhMe-d_3	0.00061(4)		0
THF	0.0033(7)	6.5	0
THF-d_4	0.00051(7)		0

After all oxidation experiments with substrates were completed, the log $k_2{'}$

correlates linearly with the strength of the C-H bond being cleaved with a slope of -0.10

(**Figure 4.15**). This shallow slope reveals that **12** is less sensitive to the C-H bond strength

of the substrate, which is similar to the Co(IV)-dinitrate complex that we reported (slope

= -0.13) in Chapter 3.
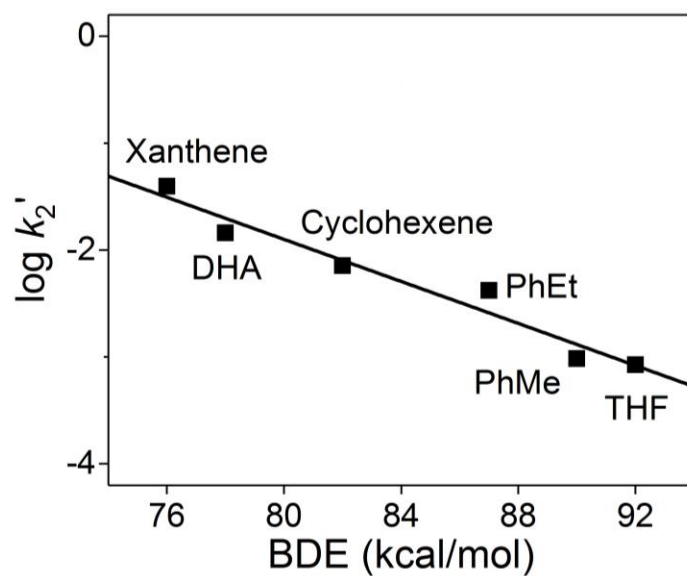
Figure 4.15. Plots of log k_2' as a function of C-H bond strength for substrate oxidation by **12** in acetonitrile at 0 °C, fitted linearly.

Even though the slope of **12** is similar to the slope of **5** from the C-H bond oxidation reaction, the slope is even less steep, but a consensus regarding the origin for these shallow slopes is lacking.[121,122] This is an indication that the C-H bond is not fully broken, but instead the reaction proceeds through an early transition state. We are hoping to receive some more insight from the computational studies done by our collaborators to design a pathway for a mechanism similar to the Cobalt species described in Chapter 3.

4.4 Conclusions

This chapter presented a rare, mononuclear Ni(IV)-nitrate complex supported by a tridentate, di-anionic ligand upon one-electron oxidation of the Ni^{III} precursor. Compared to the Co(IV)-dinitrate analogue supported by the same N3 ligand, our Ni(IV)-nitrate complex is only slightly faster and cleaves stronger C-H bonds up to 92 kcal/mol. As Ni^{IV} is isoelectronic to Co^{III} of the same four-coordinate geometry, it is expected that the thermodynamic driving force of cleaving C-H bonds is similar shown from

72

electrochemical and oxidation reactivity studies. Unfortunately, we could not obtain the crystal structure of the Ni(IV) species, but we have strong evidence from preliminary XAS and computational studies confirming our hypothesis that we have obtained a high-valent four coordinate Ni(IV) species. Even though our Ni(IV)-nitrate complex demonstrated less reactivity to oxidize DHA about 1-2 orders of magnitude than the Ni(III) complexes reported[67,68,74], this shows that our di-anionic tridentate N3 ligand (**L3**) is an outstanding ligand scaffold to stabilize the high-valent state of late transition metals. We plan to submit our recent findings soon for manuscript publication after XAS and computational studies are fully analyzed by our collaborators.

Chapter 5: Concluding Remarks and Future Work

In conclusion, after the decision to modify the ligand scaffold by replacing the electron-withdrawing carbonyl groups with aliphatic saturated methyl groups, our group presented two novel, mononuclear high-valent Co(IV)-dinitrate (**5**) and Ni(IV)-nitrate complexes (**12**). Throughout the development of both of these complexes, we have found that our di-anionic tridentate ligand scaffold is an excellent candidate to support the high-valent state of +4 of late transition metals.

We have fully characterized Co complexes having oxidation states of +3 and +4 using spectroscopic and computation methods including X-ray crystallography, UV-Vis, EPR, and computational studies. In efforts of investigating this conversion, we unexpectedly grew crystals providing us the structural information of **5,** specifically a five-coordinate complex with distorted square pyramidal geometry with an axial nitrate ligand ~0.17 Å longer than the equatorial nitrate ligand. It is important to note that the bond lengths of the ligands of our Co(III) and Co(IV) complexes remain the same and do not change upon an one-electron oxidation. This was a clear indication that the conversion of the Co(III) starting complex (**4** or **6**) to **5** is a metal-centered oxidation and not a ligand-based process. Therefore, our recently published Co(IV)-dinitrate complex is a *bona-fide* Co(IV) complex.

Similar applications were conducted to afford Ni complexes. We successfully grew crystals of the Ni(III) analogues (**10** and **11**). The bond lengths of the Co(III) and Ni(III) complexes are similar and the coordinating anion showed a similar pattern where the nitrate ligand is longer than the hydroxide ligand due to its higher basicity. Upon an one-

electron oxidation, we see similar observations from the UV-Vis spectra. After multiple failed attempts of obtaining crystals, we used ^{1}H NMR to provide us with structural information that delivered strong evidence that we have a four coordinate Ni(IV)-nitrate complex, **12**.

After the synthesis and characterization of these complexes, we put efforts into investigating the reactivity of **5** and **12** with strong sp^3 C-H bonds. To our knowledge, this is the first high-valent Co(IV) species both structurally characterized by X-ray crystallography and is capable of cleaving strong C-H bonds up to 87 kcal/mol in the condensed phase. As well as our soon to be published Ni(IV)-nitrate complex will be a rare example that is capable of cleaving strong C-H bonds up to 92 kcal/mol. Reactivity studies from both Co(IV)-dinitrate and Ni(IV)-nitrate complexes showed similar patterns of activating strong C-H bonds. From these observations, we have also provided preliminary data of another high-valent Co(IV) species, **7**, that was found to be more reactive towards cleaving C-H bonds when replacing the coordinating ligands with more basic anion(s) (in this case, azide).

These results obtained in this dissertation were a gateway that opened many doors for the future of this project. Even though the beginning of my doctorate journey was difficult, being patient can lead to a miraculous outcome such as changing our ligand scaffold from **L1** to **L3** led to these exciting results discussed. Throughout the development of these two complexes of both Co and Ni, we still question and hypothesize that the results obtained could potentially help us obtain a high-valent terminal metal-oxo complex. The results obtained generated two Co(IV) and one Ni(IV) complexes that

are capable of cleaving strong C-H bonds. This research will inspire the generation of more reactive high-valent metal-oxo and non-oxo complexes that will provide more insight into the chemistry behind C-H bond activation and high-valent metal oxo chemistry.

Future work includes investigating the reactivity of the high-valent Co(IV)-diazide with other substrates and fully obtaining structural and electronic properties. We would also like to extend this chemistry by substituting out azide with other basic coordinating anions to promote a radical rebound in the mechanism and design a catalytic cycle for these complexes. To further the usefulness of our ligand scaffold (**L3**), as we found out that it is robust and prevents oxidation of the ligand. This finding will allow us to apply modifications to the N3 ligand to reduce the electron donating ability of the anionic amine *N*-donors by incorporating electron-withdrawing substituents to generate more reactive high-valent late transition metal (Co, Ni, and Cu) complexes and study their structure-reactivity relationship.

Experimental Section
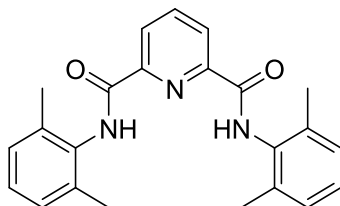
Synthesis of *N, N'*-Bis(2,6-dimethylphenyl)-2,6-pyridinedicarboxamide (H$_2$pyN$_2$^{Me2}) (L1).
To a 500 mL Erlenmeyer flask containing a stir bar was added, pyridine-2, 6 -dicarbonyl chloride (1.02 g, 5.00 mmol) and it was dissolved in THF (200 mL) at 0° C. To a 20 mL scintillation vial, dimethylaniline (1.21 g, 10.00 mmol), triethylamine (1.40 mL, 10.00 mmol) containing dissolved in THF (5 mL) was added slowly to the solution in the Erlenmeyer flask. The flask was stirred for 5 h and was warmed to room temperature. The solution was filtered. The solvent was removed in vacuo and was treated with hexane. The solid was washed with a small volume of dichloromethane/ether (1:5 v/v) to give a white powder and was identified as **L1** (100 %). ^{1}H NMR (CDCl$_3$) = 2.32 (s, 12 H), 6.10 (m, 6 H), 8.17 (t, 1 H), 8.55 (d, 2H), 9.06 (s, 2 H).
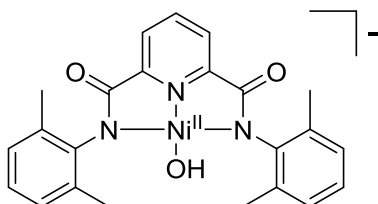
Synthesis of [Me$_4$N][Ni^{II}(H$_2$pyN$_2$^{Me2})(OH)] (1). Complex **1** was prepared following an experimental procedure reported by Holm and co-authors.[83] To a 20 mL scintillation vial equipped with a stir bar, H$_2$pyN$_2$^{Me2} (0.100 g, 0.267 mmol) and Ni(OTf)$_2$ (0.095 g, 0.267 mmol) were dissolved in CH$_3$CN (10 ml) and stirred at room temperature for 2 h. The light yellow suspension was treated with Me$_4$NOH (25% in MeOH, 0.292 g, 0.803 mmol) and was stirred overnight to afford a deep orange solution. The solvent was removed in vacuo and was re-dissolved in DCM and filtered through a filter syringe. Recrystallization from DCM and diethyl ether afforded orange crystals identified as **1** (60%). ^{1}H NMR (CD$_3$CN): 1.31 (s, 1 H), 2.46 (s, 12 H), 6.88 (m, 6 H), 7.48 (d, 2 H), 7.96 (s, 1 H).
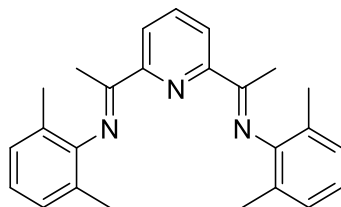
Synthesis of 2,6-bis((1-[(2,6-dimethylphenyl)imino]ethyl)pyridine) (L2). To a 250 mL round bottom flask equipped with a stir bar, 2, 6- diacetylpyridine (4.98 g, 30.5 mmol) was added. Using a graduated cylinder, 2, 6- dimethylaniline (8.50 mL, 67.1 mmol) was added to the round bottom flask. MeOH (100 mL) was added and stirred until all reactants dissolved and formic acid (~0.25 mL) was added to the flask. The solution was stirred and refluxed at 70° C for 12 h. The flask was moved to the refrigerator for 24 h. The resulting yellow solid was vacuum filtered through a funnel and washed with MeOH. The dry yellow solid was dried through the Schlenk line and identified as **L2** (90%). ^{1}H NMR (CDCl$_3$): 2.06 (s, 12 H), 2.22 (s, 6 H), 6.95 (t, 2 H), 7.09 (d, 4 H), 7.92 (t, 1 H), 8.49 (d, 2 H).
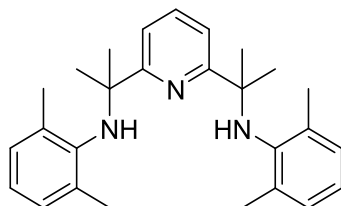
Synthesis of 2,6-bis((2-(2,6)-dimethylphenylamino))isopropyl)pyridine) (L3). To a 250 mL round bottom flask equipped with a stir bar, 2,6-bis-[1-(2,6-dimethylphenylimino)ethyl]pyridine (2.00 g, 5.19 mmol) was dissolved in toluene (50 mL) producing a yellow solution. While stirring, 1.5 eq of trimethylaluminum (2.0 M in toluene) was added producing a green solution. The solution was refluxed under Ar gas for 24 h. The solution was cooled and 3 mL of water was added slowly and stirred for 30 min at RT producing a yellow orange solution. The reaction mixture was filtered through sodium sulfate and glass wool and washed with 75 mL of diethyl either. The solvent was removed via rotary evaporation and was brought back into the glovebox. The residue was dissolved in the same amount of toluene and the above procedure was repeated. The residue was then dissolved in a slurry of silica gel, the solvent was removed via rotovap, and purified with hexane/ethyl acetate (95:5) mixture with flash chromatography. The solvent was removed and redissolved in MeOH (10 mL) and placed in the -30°C freezer overnight for the formation of **L3** (50%). ^{1}H NMR (500 mHz, CDCl3): δ = 1.55 (s, 12 H), 2.12 (s, 12 H), 4.20 (s, 2 H), 6.89 (t, 2 H), 7.01 (d, 4 H), 7.52 (d, 2 H), 7.68 (t, 1 H).
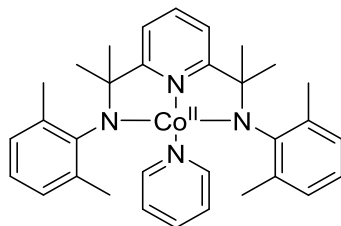
Synthesis of L3Co^{II}-py (2). Complex **2** was prepared following an experimental procedure reported by Lavoie and co-authors.[90] To a 100 mL Schlenk flask equipped with a stir bar, 2,6-bis((2-(2,6-dimethylphenylamino))isopropyl)pyridine) (0.200 g, 0.498 mmol) and CoCl$_2$py$_4$ (0.222 g, 0.498 mmol) was dissolved in toluene (20 mL) producing a yellow green solution. While stirring, the solution was cooled to -90°C under Ar gas for 30 min. A solution of 2 eq. of (Trimethylsilyl)-methyllithium (1.0 M in pentane) dissolved in 2 mL of toluene was syringed into the Schlenk flask and was warmed to RT under Ar gas overnight producing a red brown solution. The solvent was removed *in vacuo* and was brought back into the glove box to be redissolved in 3 mL of toluene. The solution was filtered through a syringe filter and solvent was removed *in vacuo*, yielding a red brown solid identified as **2**. **2** was used immediately to generate **3**.
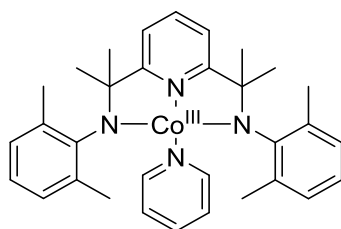
Synthesis of L3Co^{III}-(py)[BF$_4$] (3). Complex **3** was prepared following an experimental procedure reported by Lavoie and co-authors.[90] To a 20 mL scintillation vial equipped with a stir bar, [NNNMe$_8$(Co^{II}(py))] (0.200 g, 0.372 mmol) was dissolved in 8 mL of toluene. While stirring, a solution of 1.5 eq. of silver tetrafluoroborate was syringed into the vial and was stirred for 3 hr. The solution was filtered through a filter syringe and washed with 5 mL of toluene. The toluene solution was discarded. The product was extracted with the addition of dichloromethane and filtered through a filter syringe yielding a blue solution. The solvent was removed *in vacuo*, yielding a blue solid and identified as **3**.
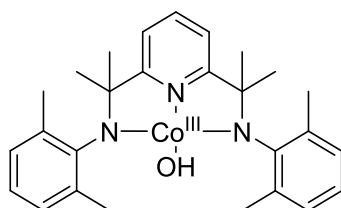
Synthesis of L3Co^{III}-OH (4). Complex **4** was prepared following an experimental procedure reported by Lavoie and co-authors.[90] To a 20 ml scintillation vial equipped with a stir bar,

L3Co^{III}-(py)[BF$_4$] (0.200 g, 0.320 mmol) and 5 equivalent of sodium hydroxide (0.064g, 1.60 mmol) was added in 10 ml of CH$_2$Cl$_2$ and stirred for 3 hours producing a purple solution. The solvent was removed in vacuum, yielding a purple solid. The solid was re-dissolved in 5 ml CH$_2$Cl$_2$ and then filtered using a syringe filter into a scintillation vial. The filtrate was layered with pentane and the vial was set aside overnight, after which dark crystals of **4** were isolated (75% yield). ^{1}H NMR (500 MHz, CDCl$_3$): δ = 8.23 (t, 1H), 7.53 (d, 2H), 7.45 (d, 4H), 7.11 (t, 2H), 1.57 (s, 12H), 1.14 (s, 12H), -0.09 (s, 1H). Elemental Analysis for C$_{27}$H$_{34}$CoN$_3$O•0.5(C$_5$H$_{12}$), calculated: C, 69.26; H, 7.88; N, 8.21, found: C, 68.12; H, 7.61; N, 7.91.
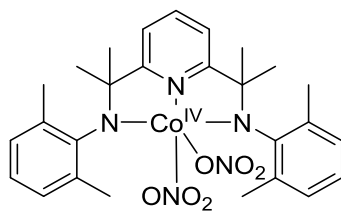
Generation of L3Co^{IV}-(NO$_3$)$_2$ (5). In a typical synthesis of **5**, to a 5 ml screw cap vial equipped with a stir bar, **4** (0.010 g, 0.021 mmol) was dissolved in MeCN. While stirring, CAN (0.017g, 0.031 mmol) pre-dissolved in MeCN was added to the solution of **4**, producing a green solution. The solution was filtered through a syringe filter into a vial and diethyl ether was added to the solution to precipitate **5**. **5** was filtered, dried, and re-dissolved in 1 ml CH$_2$Cl$_2$ and layered with pentane. The vial was placed in a -30°C freezer for a week, after which dark green crystals of **5** were isolated (82% yield).
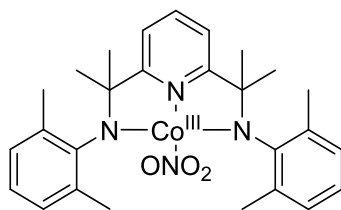
Generation of L3Co^{III}-ONO$_2$ (6). To a UV-cuvette containing a freshly prepared MeCN solution of **4**, 6 eq. of tetrabutylammonium nitrate (pre-dissolved in MeCN to make a stock solution) was added using a micro-syringe at room temperature. The formation of **6** was observed due to change of the absorption from 570 nm to 585 nm. For a larger scale synthesis, to a 20 ml scintillation vial equipped with a stir bar, **4** (0.100 g, 0.210 mmol) and 5 eq. of sodium nitrate (0.089g, 1.05 mmol) was dissolved in 10 ml of MeCN and stirred for 2 h producing a blue solution. The solution was filtered using a syringe filter into a scintillation vial. The solvent was removed in vacuum, yielding a blue solid. The solid was re-dissolved in 5 ml of toluene and then filtered using a syringe filter into a scintillation vial. The filtrate was removed in vacuum and was re-dissolved in CH2Cl2. The solution was layered with pentane and the vial was placed in the 0 °C refrigerator for a week, after which blue crystals of **6** were isolated (65% yield).
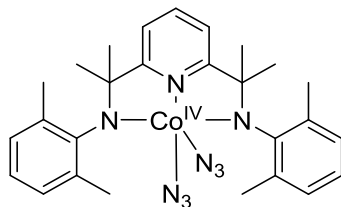
Generation of L3Co^{IV}-(N$_3$)$_2$ (7). To a UV-cuvette containing a freshly prepared MeCN solution of **6**, 3 eq. of TBAN$_3$ (pre-dissolved in MeCN to make a stock solution) was added using a micro-syringe at -40°C. The formation of 7 was observed due to the change of the absorption from 750 nm to 635 nm.
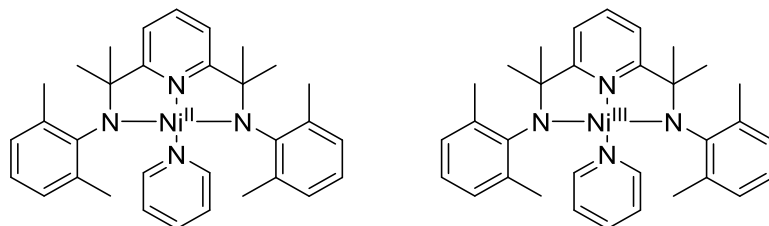
Synthesis of L3Ni^{II}-py (8) & L3Ni^{III}-py[BF$_4$] (9). Complexes **8** and **9** was prepared following the experimental procedure of complexes 2 and 3 using NiCl$_2$py$_4$.
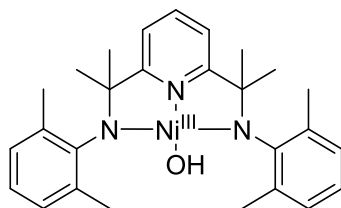
Synthesis of L3Ni^{III}-OH (10). To a 20 ml scintillation vial equipped with a stir bar, **9** (0.200 g, 0.320 mmol) and 5 equivalent of sodium hydroxide (0.064g, 1.60 mmol) was added in 10 ml of CH$_2$Cl$_2$ and stirred for 3 hours producing a green solution. The solvent was removed in vacuum, yielding a green solid. The solid was re-dissolved in 5 ml CH$_2$Cl$_2$ and then filtered using a syringe filter into a scintillation vial. The filtrate was layered with pentane and the vial was set aside overnight at room temperature, after which dark crystals of **10** were isolated in a yield of 65%. Elemental Analysis for C$_{27}$H$_{34}$NiN$_3$O calculated: C, 68.23; H, 7.21; N, 8.84, found: C, 68.15; H, 7.22; N, 8.77.
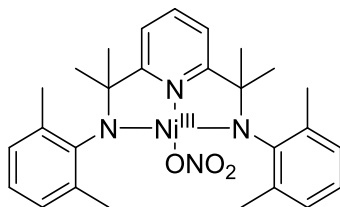
Synthesis of L3Ni^III-ONO₂ (11). To a 20 mL scintillation vial with a stir bar, **9** (0.200 g, 0.420 mmol) and 5 eq. of sodium nitrate (0.0178 g, 2.10 mmol) was dissolved in MeCN and stirred for 3 hours. The solution was filtered using a syringe filter into a scintillation vial. The solvent was removed in vacuum, yielding a green solid. The solid was re-dissolved in 5 ml CH_2Cl_2. The solution was layered with pentane and the vial was placed in the 0 °C refrigerator for a week, after which green crystals of **11** were isolated (50% yield).
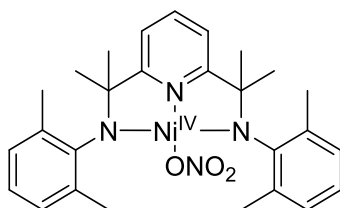
Generation of L3Ni^IV-ONO₂ (12). To a UV-cuvette containing a freshly prepared MeCN solution of 12, 1 eq. of CAN (pre-dissolved in MeCN to make a stock solution) was added using a micro-syringe at 0°C. The formation of 12 was observed due to the change of the absorption from 945 nm to 412 nm.

Chapter 3 Methods

General Materials and Procedures. All manipulations were performed using standard Schlenk techniques and/or utilizing a VAC glovebox (N_2). All reagents were purchased from commercial sources and are of the highest commercially available purity and used as received, unless noted otherwise. DHA-d_4 and xanthene-d_2 were prepared according to the previous procedure reported.[1] Ceric ammonium nitrate (CAN), xanthene, 9, 10-dihydroanthracene (DHA), cyclohexene, tetralin, ethylbenzene, ethylbenzene-d_{10}, naphthalene, ferrocene, tetrabutylammonium nitrate, acetonitrile (MeCN), pentane, diethyl ether, and dichloromethane (CH_2Cl_2) were purchased from Aldrich. DHA was recrystallized twice from ethanol before use.

Physical Methods. ^{1}H NMR spectra were obtained with a Varian VNMRS 500 MHz spectrometer at room temperature. UV-Vis spectra were recorded on an Agilent Technologies Cary 8454 spectrometer equipped with a Unisoku USP-203-A cryostat for temperature control. GC-MS analysis was carried out on an Agilent Technologies 6890N GC system with a 5973 Mass selective detector. Cyclic voltammetry was performed on a CH Instrument 730E electrochemical workstation in acetonitrile at 25 °C using a Ag/AgCl

reference electrode, a glassy carbon working electrode, and a Pt auxiliary electrode. 0.1 M KPF_6 was used as the supporting electrolyte. EPR spectra were collected using an X-band Bruker EMXPlus spectrometer with a Bruker ER4116DM dual-mode cavity. An Oxford ESR900 continuous-flow liquid helium cryostat was used to monitor applied temperature. Experimental temperatures were controlled with an Oxford ITC503 cryostat controller. Parameters used in collecting spectra are provided in the caption of Figure 3.8.

Substrate oxidation by complex 5 and 7. Unless otherwise stated, all kinetic measurements were performed in acetonitrile at room temperature. CH_2Cl_2 was used to increase the solubility of substrates such as xanthene and DHA. In a typical experiment, an excess amount of substrate (pre-dissolved in CH_2Cl_2/MeCN to make a stock solution) was added to a UV cuvette containing a freshly prepared MeCN solution of 4 using a micro-syringe. Under fast stirring, the change of the optical spectrum was monitored and recorded as a function of time. The time trace of the 420 nm band for each reaction was fitted using pseudo-first-order model to obtain the rate constant k_{obs}. For each substrate, a concentration dependence experiment was carried out to measure k_{obs} under each substrate concentration. The plot of k_{obs} vs. substrate concentration was then fitted linearly to obtain the second order rate constant k_2.

Chapter 4 Methods

General Materials and Procedures. All manipulations were performed using standard Schlenk techniques and/or utilizing a VAC glovebox (N_2). All reagents were purchased from commercial sources and are of the highest commercially available purity and used as received, unless noted otherwise. DHA-d_4 and xanthene-d_2 were prepared according to the previous procedure reported.[1] Cerium ammonium nitrate (CAN), xanthene, 9, 10-dihydroanthracene (DHA), cyclohexene, tetralin, ethylbenzene, ethylbenzene-d_{10}, toluene, toluene-d_8, naphthalene, ferrocene, acetonitrile (MeCN), pentane, diethyl ether, and dichloromethane (CH_2Cl_2) were purchased from Aldrich. DHA was recrystallized twice from ethanol before use.

Physical Methods. ^{1}H NMR spectra were obtained with a Varian VNMRS 500 MHz spectrometer at -35 °C. UV-Vis spectra were recorded on an Agilent Technologies Cary 8454 spectrometer equipped with a Unisoku USP-203-A cryostat for temperature control. GC-MS analysis was carried out on an Agilent Technologies 6890N GC system with a 5973 Mass selective detector. Cyclic voltammetry was performed on a CH Instrument 730E electrochemical workstation in acetonitrile at -40 °C using a Ag/AgCl reference electrode, a glassy carbon working electrode, and a Pt auxiliary electrode. 0.1 M KPF_6 was used as the supporting electrolyte. EPR spectra were collected using an X-band Bruker EMXPlus spectrometer with a Bruker ER4116DM dual-mode cavity. An Oxford ESR900 continuous-flow liquid helium cryostat was used to monitor applied temperature. Experimental temperatures were controlled with an Oxford ITC503 cryostat controller. Parameters used in collecting spectra are provided in the caption of Figure 4.4.

Substrate oxidation by complex 12. Unless otherwise stated, all kinetic measurements were performed in acetonitrile at 0° C. CH_2Cl_2 was used to increase the solubility of substrates such as xanthene and DHA. In a typical experiment, an excess amount of substrate (pre-dissolved in CH_2Cl_2/MeCN to make a stock solution) was added to a UV cuvette containing a freshly prepared MeCN solution of **2** using a micro-syringe. Under fast stirring, the change of the optical spectrum was monitored and recorded as a function of time. The time trace of the 412 nm band for each reaction was fitted using pseudo-first-order model to obtain the rate constant k_{obs}. For each substrate, a concentration dependence experiment was carried out to measure k_{obs} under each substrate concentration. The plot of k_{obs} vs. substrate concentration was then fitted linearly to obtain the second order rate constant k_2.

X-ray Crystallography

X-ray diffraction data for **4**, **5**, and **6** were collected at 100 K on a Bruker D8 Venture using MoKα-radiation (λ = 0.71073 Å). Data have been corrected for absorption using SADABS[123] area detector absorption correction program. Using Olex2,[124] the structure was solved with the SHELXT[125] structure solution program using Direct Methods and refined with the SHELXL[126] refinement package using least squares minimization. All non-hydrogen atoms were refined with anisotropic thermal parameters. All hydrogen atoms of the investigated structure were located from difference Fourier maps but finally their positions were placed in geometrically calculated positions and refined using a riding model. Isotropic thermal parameters of the placed hydrogen atoms were fixed to 1.2 times the *U* value of the atoms they are linked to (1.5 times for methyl groups). Calculations and refinement of the structure were carried out using APEX3,[127] SHELXTL,[128] and Olex2 software.

X-ray diffraction data for **10** were collected at 100 K on a Bruker D8 Venture using MoKα-radiation (λ=0.71073 Å). Data have been corrected for absorption using SADABS[123] area detector absorption correction program. Using Olex2[124], the structure was solved with the SHELXT[125] structure solution program using Direct Methods and refined with the SHELXL[126] refinement package using least squares minimization. All non-hydrogen atoms were refined with anisotropic thermal parameters. Hydrogen atoms attached to heteroatoms were found from the residual density maps, placed, and refined with isotropic thermal parameters. All other hydrogen atoms in the investigated structure were located from difference Fourier maps but finally their positions were placed in geometrically calculated positions, and refined using a riding model. Isotropic thermal parameters of the placed hydrogen atoms were fixed to 1.2 times the *U* value of the atoms they are linked to (1.5 times for methyl groups). The dichloromethane in the structure is disordered, necessitating the use of bond length similarity restraints, one thermal ellipsoid similarity restraint and one thermal ellipsoid similarity constraint. Calculations and refinement of structures were carried out using APEX3[127], SHELXTL[128], and Olex2 software.

X-ray diffraction data for **11** were collected at 100 K on a Bruker D8 Venture using MoKα-radiation (λ=0.71073 Å). Data have been corrected for absorption using SADABS[123] area detector absorption correction program. Using Olex2[124], the structure was solved with the SHELXT[125] structure solution program using Direct Methods and refined with the SHELXL[126] refinement package using least squares minimization. All non-hydrogen atoms were refined with anisotropic thermal parameters. The hydrogen atoms of the investigated structure were located from difference Fourier maps but finally their positions were placed in geometrically calculated positions and refined using a riding model. Isotropic thermal parameters of the placed hydrogen atoms were fixed to 1.2 times the U value of the atoms they are linked to (1.5 times for methyl groups). Calculations and refinement of structures were carried out using APEX3[127], SHELXTL[128], and Olex2 software.

Crystallographic Data for 4: $C_{27}H_{34}CoN_3O$ (M =475.50 g/mol): triclinic, space group P-1 (no. 2), $a =$ 8.7684(5) Å, $b =$ 11.8623(7) Å, $c =$ 12.2989(7) Å, $\alpha =$ 89.239(3)°, $\beta =$ 77.878(2)°, $\gamma =$ 77.626(2)°, $V =$ 1221.00(12) Å^3, $Z =$ 2, $T =$ 100 K, μ(MoKα) = 0.726 mm^{-1}, $Dcalc$ = 1.293 g/cm^3, 2Θmax = 52.876°, 9549 reflections measured, 9549 unique (R_{int} = 0.0208, R$_{sigma}$ = 0.0554), R_1 was 0.0484 (I > 2σ(I)), wR_2 was 0.1481 (all data).

Crystallographic Data for 5: $C_{27}H_{33}CoN_5O_6$ (M =582.51 g/mol): monoclinic, space group P21/n (no. 14), a = 7.9985(5) Å, b = 19.2252(11) Å, c = 17.3541(9) Å, β = 99.346(2)°, V = 2633.2(3) Å3, Z = 4, T = 100 K, μ(MoKα) = 0.704 mm-1, Dcalc = 1.469 g/cm3, 2Θmax = 50.154°, 36303 reflections measured, 4668 unique (Rint = 0.0969, Rsigma = 0.0514), R1 = 0.0422 (I > 2σ(I)), wR2 = 0.0862 (all data).

Crystallographic Data for 6: $C_{27.5}H_{34}ClCoN_4O_3$ (M =562.96 g/mol): monoclinic, space group C2/c (no. 15), a = 36.2527(18) Å, b = 10.9071(5) Å, c = 30.0533(15) Å, β = 116.4340(10)°, V = 10641.0(9) Å3, Z = 16, T = 100 K, μ(MoKα) = 0.782 mm-1, Dcalc = 1.406 g/cm3, 2Θmax = 50.882°, 153636 reflections measured, 9826 unique (Rint = 0.0737, Rsigma = 0.0330), R1 = 0.0463 (I > 2σ(I)), wR2 = 0.1201 (all data).

Crystallographic Data 10: $C_{28}H_{36}Cl_2N_3NiO$ (M =560.21 g/mol): monoclinic, space group P2$_1$/n (no. 14), $a =$ 8.7226(4) Å, $b =$ 14.1205(6) Å, $c =$ 22.4103(11) Å, $\beta =$ 96.428(2)°, $V =$ 2742.9(2) Å^3, $Z =$ 4, $T =$ 100 K, μ(MoKα) = 0.928 mm^{-1}, $Dcalc =$ 1.357 g/cm^3, 2Θmax = 55.1°, 38537 reflections collected, 6332 unique (R_{int} = 0.0568, R$_{sigma}$ = 0.0467), R_1 = 0.0420 (I > 2σ(I)), wR_2 = 0.0905 (all data).

Crystallographic Data for 11: $C_{27}H_{33}N_4NiO_3$ (M =520.28 g/mol): tetragonal, space group P4$_2$/n (no. 86), $a =$ 21.7371(11) Å, $c =$ 10.6624(6) Å, $V =$ 5038.0(6) Å^3, $Z =$ 8, $T =$ 100 K, μ(MoKα) = 0.806 mm^{-1}, $Dcalc =$ 1.372 g/cm^3, 2Θmax = 51.478°, 87611 reflections measured, 4799 unique (R_{int} = 0.0912, R$_{sigma}$ = 0.0286), R_1 = 0.0339 (I > 2σ(I)), wR_2 = 0.0822 (all data).

Appendix: Supplementary Figures and Tables
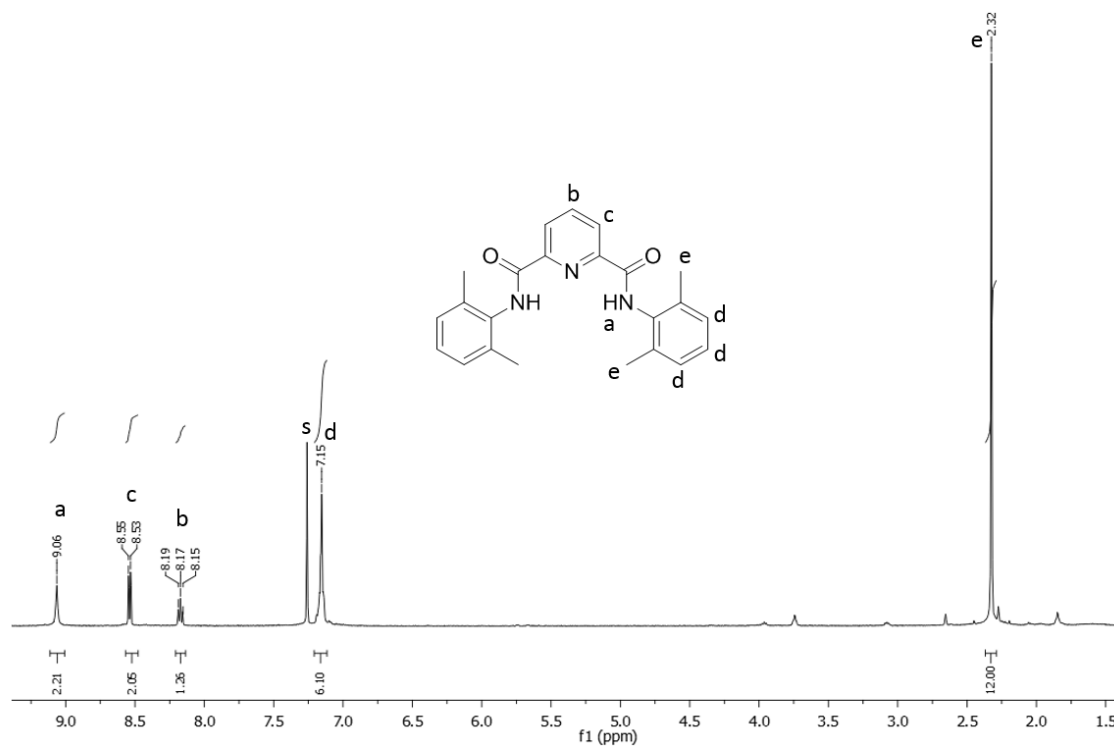
Figure S1. ^{1}H NMR of **L1**, with the signals assigned to the corresponding protons on the ligand. Signals labeled "s" represent the solvent residuals.
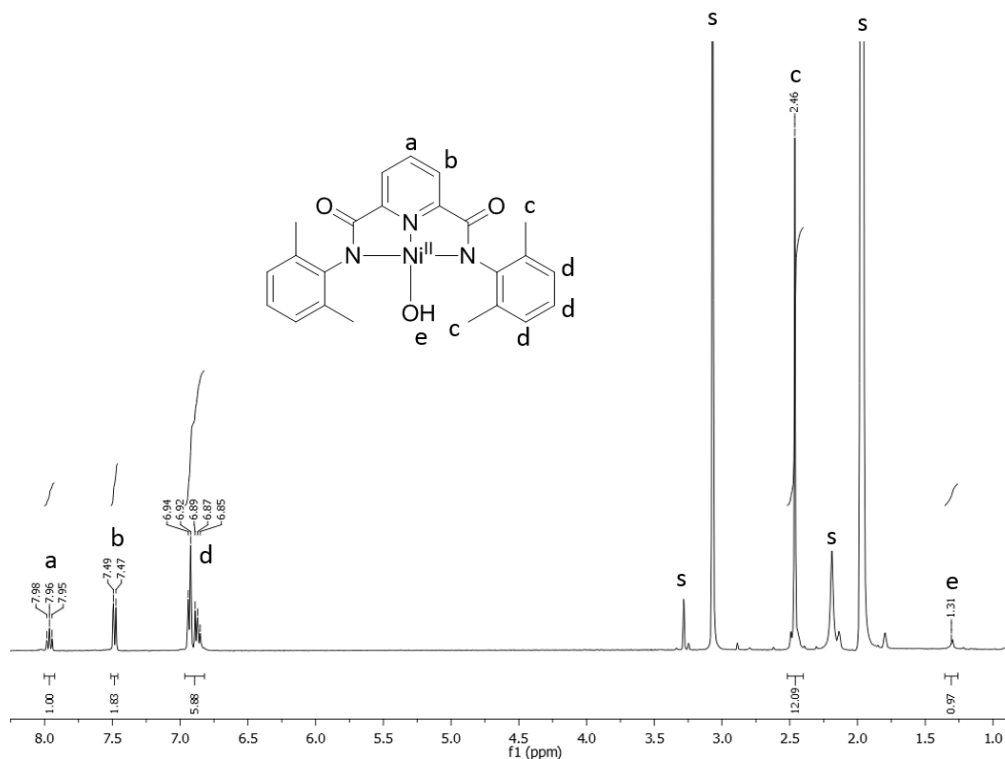
Figure S2. ^{1}H NMR of **1**, with the signals assigned to the corresponding protons on the ligand. Signals labeled "s" represent the solvent residuals.
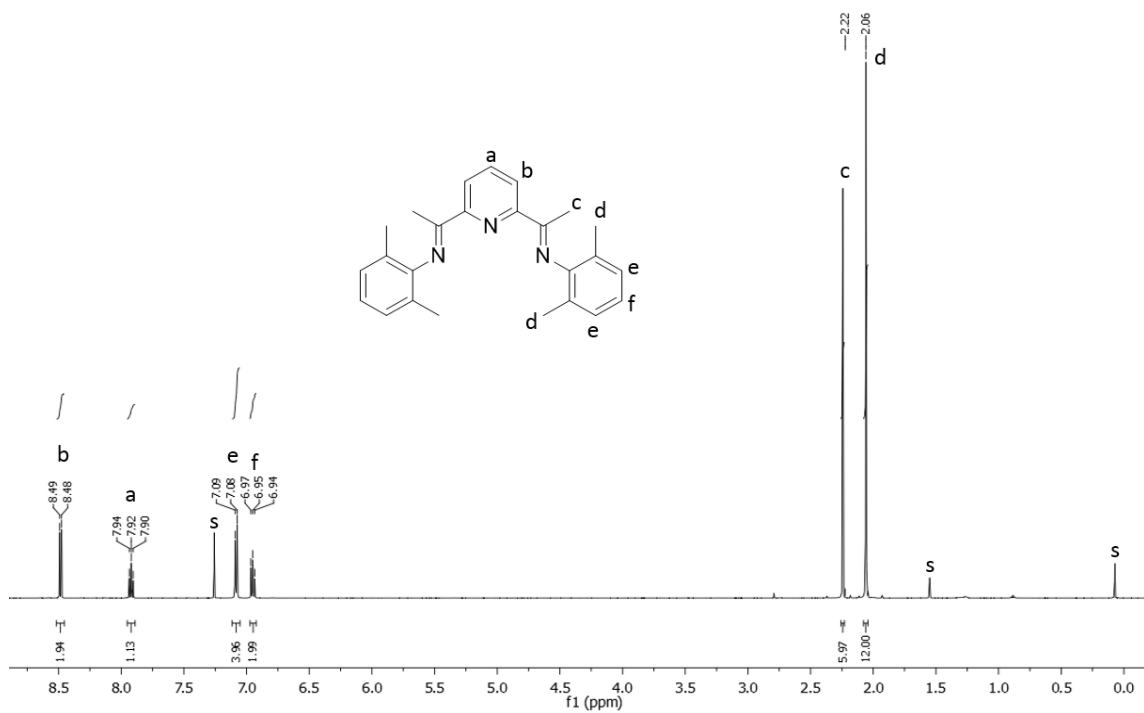
Figure S3. ^{1}H NMR of **L2**, with the signals assigned to the corresponding protons on the ligand. Signals labeled "s" represent the solvent residuals.
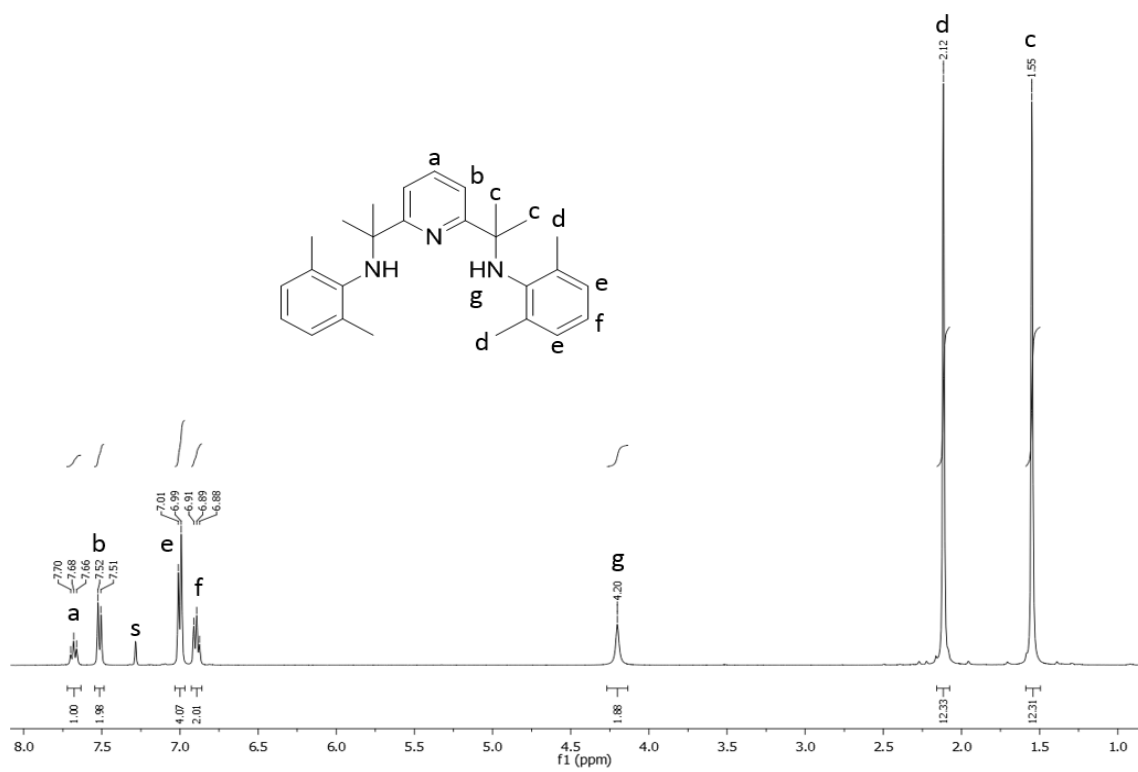
Figure S4. ^{1}H NMR of **L3**, with the signals assigned to the corresponding protons on the ligand. Signals labeled "s" represent the solvent residuals.
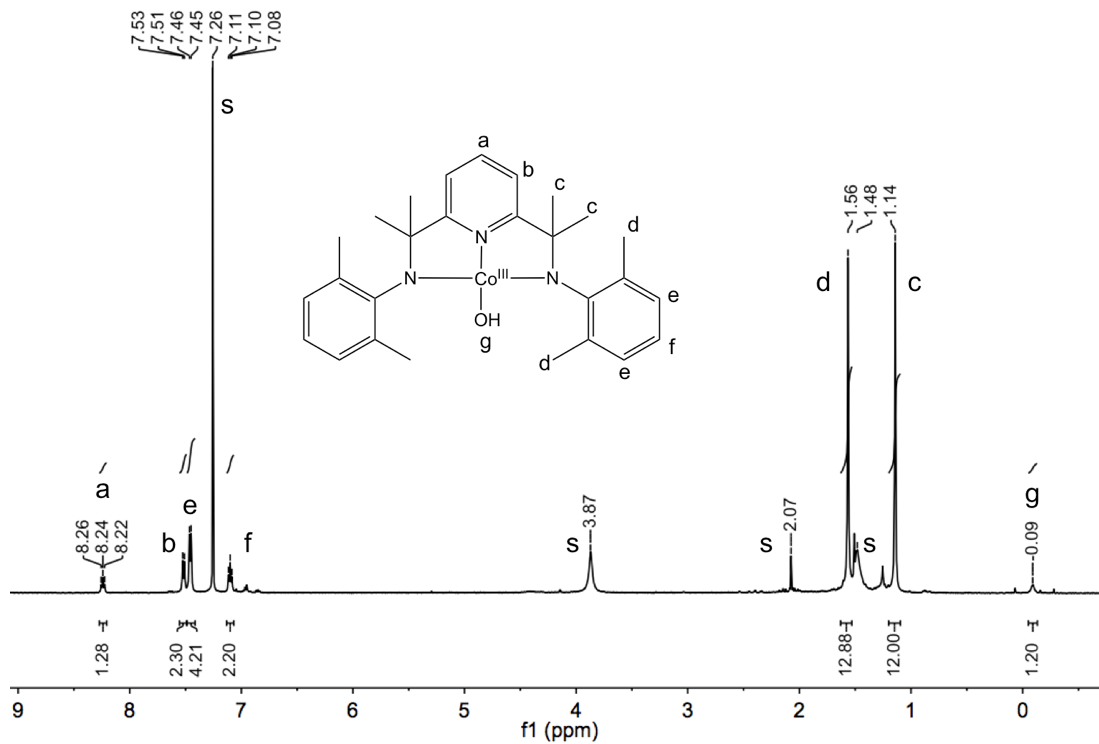
Figure S5. ^{1}H NMR of **4**, with the signals assigned to the corresponding protons on the ligand. Signals labeled "s" represent the solvent residuals.

Table S1. Pseudo first-order constants (k_{obs}) for the reaction of **5** with various substrates at different concentration.

Concentration (M)	Substrate			
	k_{obs} (s^{-1})			
	Xanthene	Xanthene-d_2	DHA	DHA-d_4
0.025	0.00480	0.00145	1.51E-4	-
0.050	0.00681	0.00205	0.00188	0.00187
0.075	0.0107	0.00345	0.00427	-
0.100	0.0164	0.00495	0.00752	0.00289
0.150	-	-	0.00943	0.00488
0.200	-	-	0.0139	0.00685
0.250	-	-	0.0182	0.00833
Concentration (M)	c-C$_6$H$_{10}$	Tetralin	PhEt	PhEt-d_2
0.100	0.00493	-	-	-
0.150	0.00769	-	-	-
0.200	0.00952	-	-	-
0.250	0.0122	0.00471	-	-
0.500	-	0.00967	-	-
0.750	-	0.0118	-	-
1.0	-	0.0191	0.00411	7.93E-4
2.0	-	-	0.00615	9.59E-4
3.0	-	-	0.00844	0.00211
4.0	-	-	0.0144	0.00245

Table S2. Pseudo first-order constants (k_{obs}) for the reaction of **12** with various substrates at different concentration.

	Substrate					
	k_{obs} (s^{-1})					
Concentration (M)	Xanthene	Xanthene-d_2	DHA	DHA-d_4	c-C$_6$H$_{10}$	
0.025	-	-	0.00140	4.73E-4	-	
0.050	0.00314	7.00E-4	0.00292	7.91E-4	0.00276	
0.075	-	-	0.00463	0.00104	-	
0.100	0.00610	0.00122	0.00565	0.00144	0.00402	
0.150	0.0105	0.00153	-	-	0.00602	
0.200	0.0147	0.00201	-	-	0.00685	
Concentration (M)	PhEt	PhEt-d_2	PhMe	PhMe-d_3	THF	THF-d_4
0.025	0.00368	6.39E-4	0.00132	7.34E-4	-	-
0.050	0.00546	8.47E-4	0.00194	9.02E-4	-	-
0.075	0.00746	0.00120	0.00252	0.00104	-	-
0.100	0.0100	0.00153	0.00305	0.00120	-	-
0.500	-	-	-	-	0.00244	0.00112
0.750	-	-	-	-	-	-
1.0	-	-	-	-	0.00405	0.00134
1.5	-	-	-	-	0.00585	0.00161
2.0	-	-	-	-	0.00746	0.00189

Table S3. Crystal data and structure refinement for **4**.

Identification code	Co^{III}-OH
Identification code	**Co^{III}-OH**
Empirical formula	$C_{27}H_{34}CoN_3O$
Formula weight	475.50
Temperature/K	100
Crystal system	triclinic
Space group	P-1
a/Å	8.7684(5)
b/Å	11.8623(7)
c/Å	12.2989(7)
α/°	89.239(3)
β/°	77.878(2)
γ/°	77.626(2)
Volume/Å^3	1221.00(12)
Z	2
ρ_{calc}g/cm^3	1.293
μ/mm^{-1}	0.726
F(000)	504.0
Crystal size/mm^3	0.38 × 0.12 × 0.07
Radiation	MoKα (λ = 0.71073)
2Θ range for data collection/°	5.308 to 52.876
Index ranges	-10 ≤ h ≤ 10, -14 ≤ k ≤ 14, -15 ≤ l ≤ 15
Reflections collected	9549
Independent reflections	9549 [R$_{int}$ = 0.0208, R$_{sigma}$ = 0.0554]
Data/restraints/parameters	9549/0/298
Goodness-of-fit on F^2	1.041
Final R indexes [I>=2σ (I)]	R$_1$ = 0.0484, wR$_2$ = 0.1376
Final R indexes [all data]	R$_1$ = 0.0650, wR$_2$ = 0.1481
Largest diff. peak/hole / e Å^{-3}	0.61/-0.34

Table S4. Crystal data and structure refinement for **5**.

Identification code	Co^{IV}-$(ONO_2)_2$
Empirical formula	$C_{27}H_{33}CoN_5O_6$
Formula weight	582.51
Temperature/K	100
Crystal system	monoclinic
Space group	$P2_1/n$
a/Å	7.9985(5)
b/Å	19.2252(11)
c/Å	17.3541(9)
α/°	90
β/°	99.346(2)
γ/°	90
Volume/Å^3	2633.2(3)
Z	4
ρ_{calc}g/cm^3	1.469
μ/mm^{-1}	0.704
F(000)	1220.0
Crystal size/mm^3	0.55 × 0.08 × 0.01
Radiation	$MoK\alpha$ (λ = 0.71073)
2Θ range for data collection/°	5.208 to 50.154
Index ranges	-8 ≤ h ≤ 9, -22 ≤ k ≤ 22, -20 ≤ l ≤ 20
Reflections collected	36303
Independent reflections	4668 [R_{int} = 0.0969, R_{sigma} = 0.0514]
Data/restraints/parameters	4668/0/360
Goodness-of-fit on F^2	1.043
Final R indexes [I>=2σ (I)]	R_1 = 0.0422, wR_2 = 0.0798
Final R indexes [all data]	R_1 = 0.0654, wR_2 = 0.0862
Largest diff. peak/hole / e Å^{-3}	0.46/-0.34

Table S5. Crystal data and structure refinement for **6**.

Identification code	**Co^{III}-ONO₂**
Empirical formula	$C_{27.5}H_{34}ClCoN_4O_3$
Formula weight	562.96
Temperature/K	100
Crystal system	monoclinic
Space group	C2/c
a/Å	36.2527(18)
b/Å	10.9071(5)
c/Å	30.0533(15)
α/°	90
β/°	116.4340(10)
γ/°	90
Volume/Å^3	10641.0(9)
Z	16
ρ_{calc}g/cm^3	1.406
μ/mm^{-1}	0.782
F(000)	4720.0
Crystal size/mm^3	0.27 × 0.11 × 0.02
Radiation	MoKα (λ = 0.71073)
2Θ range for data collection/°	5.02 to 50.882
Index ranges	-43 ≤ h ≤ 43, -13 ≤ k ≤ 13, -36 ≤ l ≤ 36
Reflections collected	153636
Independent reflections	9826 [R$_{int}$ = 0.0737, R$_{sigma}$ = 0.0330]
Data/restraints/parameters	9826/0/674
Goodness-of-fit on F^2	1.087
Final R indexes [I>=2σ (I)]	R$_1$ = 0.0463, wR$_2$ = 0.1099
Final R indexes [all data]	R$_1$ = 0.0689, wR$_2$ = 0.1201
Largest diff. peak/hole / e Å^{-3}	0.78/-0.96

Table S6. Crystal data and structure refinement for **10**.

Identification code	**Ni^{III}-OH**
Empirical formula	$C_{28}H_{36}Cl_2N_3NiO$
Formula weight	560.21
Temperature/K	100
Crystal system	monoclinic
Space group	$P2_1/n$
a/Å	8.7226(4)
b/Å	14.1205(6)
c/Å	22.4103(11)
α/°	90
β/°	96.428(2)
γ/°	90
Volume/Å^3	2742.9(2)
Z	4
ρ_{calc}g/cm^3	1.357
μ/mm^{-1}	0.928
F(000)	1180.0
Crystal size/mm^3	0.2 × 0.14 × 0.07
Radiation	MoKα (λ = 0.71073)
2Θ range for data collection/°	5.23 to 55.1
Index ranges	-10 ≤ h ≤ 11, -18 ≤ k ≤ 18, -29 ≤ l ≤ 29
Reflections collected	38537
Independent reflections	6332 [R_{int} = 0.0568, R_{sigma} = 0.0467]
Data/restraints/parameters	6332/12/341
Goodness-of-fit on F^2	1.030
Final R indexes [I>=2σ (I)]	R_1 = 0.0420, wR_2 = 0.0817
Final R indexes [all data]	R_1 = 0.0689, wR_2 = 0.0905
Largest diff. peak/hole / e Å^{-3}	0.44/-0.57

Table S7. Crystal data and structure refinement for **11**.

Identification code	**Ni^{III}-ONO$_2$**
Empirical formula	C$_{27}$H$_{33}$N$_4$NiO$_3$
Formula weight	520.28
Temperature/K	100
Crystal system	tetragonal
Space group	P4$_2$/n
a/Å	21.7371(11)
b/Å	21.7371(11)
c/Å	10.6624(6)
α/°	90
β/°	90
γ/°	90
Volume/Å^3	5038.0(6)
Z	8
ρ$_{calc}$g/cm^3	1.372
μ/mm^{-1}	0.806
F(000)	2200.0
Crystal size/mm^3	0.14 × 0.12 × 0.06
Radiation	MoKα (λ = 0.71073)
2Θ range for data collection/°	5.3 to 51.478
Index ranges	-26 ≤ h ≤ 26, -26 ≤ k ≤ 26, -13 ≤ l ≤ 12
Reflections collected	87611
Independent reflections	4799 [R$_{int}$ = 0.0912, R$_{sigma}$ = 0.0286]
Data/restraints/parameters	4799/0/324
Goodness-of-fit on F^2	1.041
Final R indexes [I>=2σ (I)]	R$_1$ = 0.0339, wR$_2$ = 0.0724
Final R indexes [all data]	R$_1$ = 0.0559, wR$_2$ = 0.0822
Largest diff. peak/hole / e Å^{-3}	0.44/-0.21

Table S8. Selected bond lengths (Å) of the N3 ligand in complexes **4**, **5**, **6, 10** and **11**.
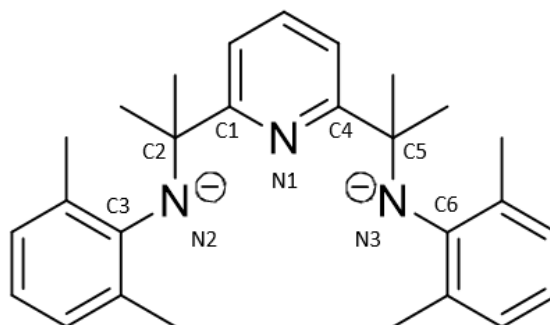
Bond	Complex				
	4	**5**	**6**	**10**	**11**
N1-C1	1.349	1.341	1.343	1.343	1.346
N1-C4	1.345	1.345	1.340	1.341	1.346
N2-C2	1.494	1.509	1.510	1.492	1.490
N2-C3	1.426	1.430	1.431	1.430	1.430
N3-C5	1.497	1.504	1.511	1.488	1.497
N3-C6	1.431	1.440	1.429	1.424	1.434
C1-C2	1.510	1.510	1.512	1.513	1.510
C4-C5	1.507	1.512	1.511	1.513	1.506

Table S9. Slopes of the BDE plot for selected oxo-metal and non-oxo-metal complexes.

Complex	Slope of BDE plot	Temperature	Reference
Oxo-metal			
MnO_4^-	-0.5	25 °C	98
$[Mn^{IV}(O)(N4Py)]^{2+}$	-0.36	25 °C	99
$[Mn^{IV}(O)(Bn\text{-}TPEN)]^{2+}$	-0.14	25 °C	100
$[Mn^{IV}(O)(2pyN2Q)]^{2+}$	-0.17	25 °C	101
$[Mn^{IV}(O)(BQCN)]^{2+}$	-0.23	0 °C	102
$[Fe^{IV}(O)(N4Py)]^{2+}$	-0.22	25 °C	103
$[Fe^{IV}(O)(Bn\text{-}TPEN)]^{2+}$	-0.25	25 °C	103
$[Fe^{IV}(O)(Me_3NTB)]^{2+}$	-0.22	-40 °C	104
$[Ru^{IV}(O)(bpy)_2(py)]^{2+}$	-0.37	25 °C	105
$[Co^{IV}(O)(13\text{-}TMC)]^{2+}$	-0.31	-40 °C	55
Non-oxo-metal			
$[Mn^{IV}(OH)_2(Me_2EBC)]^{2+}$	-0.38	25 °C	106
$[Mn^{III}(OH)(PY5)]^{2+}$	-0.1	50 °C	107
$[Fe^{III}(OH)(PY5)]^{2+}$	-0.2	50 °C	108
$[Fe^{III}(OMe)(PY5)]^{2+}$	-0.2	50 °C	97
$[Co^{IV}(OM^{n+})(TAML)]^{n-2}$	-0.15	5 °C	82
$Ni^{III}(OAc)L$	-0.23	25 °C	69
$Ni^{III}(OCl)L'$	-0.3	-30 °C	109
$Ni^{III}(pyalk)_2^+$	-0.15	25 °C	66
$Cu^{III}(OAc)L$	-0.28	25 °C	110
$Cu^{III}(OH)L$	-0.27	-25 °C	76

N4Py: N,N-bis(2-pyridylmethyl)-N-bis(2-pyridyl)methylamine
Bn-TPEN: N-benzyl-N,N',N'-tris(2-pyridyl-methyl)-1,2-diaminoethane
2pyN2Q: N,N-bis(2-quinolylmethyl)-N-bis(2-pyridyl)methylamine
BQCN: N,N'-dimethyl-N,N'-bis(8-quinolyl)cyclohexanediamine
Me$_3$NTB: tris((N-methyl- benzimidazol-2-yl)methyl)amine
13-TMC: 1,4,7,10-tetramethyl-1,4,7,10-tetraazacyclotridecane
Me$_2$EBC: 4,11-dimethyl-1,4,8,11-tetraazabicyclo[6.6.2]hexadecane
PY5: 2,6-bis(bis(2-pyridyl)methoxymethane)pyridine
TAML: tetraamido macrocyclic ligand
L: N,N'-(2,6-dialkylphenyl)-2,6-pyridinedicarboxamidate
L': tetradentate macrocyclic ligand bearing a 2,6-pyridinedicarboxamidate unit
pyalk: 2-pyridyl-2-propanoate

References

1. Appling, Anthony-Cahill, Mathews. *Biochemistry: Concepts and Connections*. **2014**.
2. Ulmer, D. D.; Vallee, B. L. Structure and Function of Metalloenzymes. **1971**.
3. Dawson, J. Probin structure-function relations in heme-containing oxygenases and peroxidases. *Science*. **1988**, 240, 433–439.
4. Capaldi, R. A. Structure and Function of Cycochrome c Oxidase. *Annu. Rev. Biochem*. **1990**, 59, 569–596.
5. Labinger, J. A.; Bercaw, J. Understanding and exploiting C-H bond activation. *Nature*. **2002**, 417, 507-514.
6. Crabtree, R. H. Alkane C-H activation and functionalization with homogeneous transition metal catalyst: a century of progress-a new millennium in prospect. *J. Chem. Soc., Dalton Trans.*, **2001**, 2437-2450.
7. Gandeepan, P.; Muller, T.; Zell, D.; Cera, G.; Warratz, S.; Ackermann, L. 3d Transition Metals for C-H Activation. *Chem. Rev.* **2019**, 119, 2192-2452.
8. Wei, Y.; Hu, P.; Zhang, M.; Su, W. Metal-Catalyzed Decarboxylative C–H Functionalization. Chem. Rev. 2017, 117, 8864-8907.
9. Borovik, A. S. Role of metal-oxo complexes in the cleavage of C-H bonds. *Chem. Soc. Rev*. **2011**, 40, 1870-1874.
10. Stone, K. L.; Borovik, A. S. Lessons from nature: unraveling biological C-H bond activation. *Curr. Op. Chem. Biol.* **2009**, 13, 114-118.
11. Gunay, A.; Theopold, K. H. C-H Bond Activations by Metal-Oxo Complexes. Chem. Rev. 2010, 110, 1060-1081.
12. Hayaishi, O.; Katagirl, M.; Rothberg, S. Mechanism of the Pyrocatchase Reaction. *J. Am. Chem. Soc.* **1955**, 77, 20, 5450-5451.
13. Ghosh, A. High-valent iron intermediates in biology. *J. Inorg. Biochem*. **2006**, 100, 419-880.
14. Groves, J. T.; Puy, M. V. D. Stereospecific Aliphatic Hydroxylation by an Iron-Based Oxidant. *J. Am. Chem. Soc.* **1974**, 96, 5274-5275.
15. Shaik, S.; Hirao, H.; Kumar, D. Reactivity of high-valent iron-oxo species in enzymes and synthetic reagents: a tale of many states. *Acc. Chem. Res.* **2007**, 40, 532-542.
16. Nam, W. high-Valent Iron(IV)-Oxo Complexes of Heme and Non-Heme Ligands in Oxygenation Reactions. *Acc. Chem. Res.* **2007**, 40, 7, 522-531.
17. Ray, K.; Pfaff, F. F.; Wang, B.; Nam, W. Status of Reactive Non-Heme Metal-Oxygen Intermediates in Chemical and Enzymatic Reactions. *J. Am. Chem. Soc.* **2014**, 136, 13942-13958.
18. Rittle, J.; Green, M. T. Cytochrome P450 Compound I: Capture, Characterization, and C-H Bond Activation Kinetics. *Science*. **2010**, 330, 933–937
19. Krebs, C.; Fujimori, D. G.; Walsh, C. T.; Bollinger, J. M. Non-Heme Fe(IV)-Oxo Intermediates. *Acc. Chem. Res*. **2007**, 40, 484-492.
20. Groves, J. T.; McClusky, G. A. Aliphatic Hydroxylation via Oxygen Rebound. Oxygen Transfer Catalyzed by Iron. *J. Am. Chem. Soc.* **1976**, 98, 859-861.
21. Huang, X.; Groves, J. T. Beyond Ferryl-mediated Hydroxylation: 40 Years of the Rebound Mechanism and C–H Activation. *J. Biol. Inorg. Chem.* **2017**, 22, 185-207.
22. Kal, S.; Que, L. Dioxygen activation by nonheme iron enzymes with the 2-His-1-carboxylate facial triad that generate high-valent oxoiron oxidants. *JBIC J. Biol. Inorg. Chem.* **2017**, 22, 339-365.

23. Wong, S. D.; Srnec, M.; Matthews, M. L.; Liu, L. V.; Kwak, Y.; Park, K.; Bell III, C. B.; Alp, E. E.; Zhao, J.; Yoda, Y.; Kitao, S.; Seto, M.; Krebs, C.; Bollinger, J. M.; Solomon, E. I. Elucidaion of the Fe(IV)=O intermediate in the catalytic cycle of the halogenase SyrB2. *Nature*. **2013**, 499, 320-324.

24. Price, J. C.; Barr, E. W.; Tirupati, B.; Bollinger, J. M., Jr.; Krebs, C. The First Direct Characterization of a High-Valent Iron Intermediate in the Reaction of an α-Ketoglutarate-Dependent Dioxygenase: A High-Spin Fe(IV) Complex in Taurine/α-Ketoglutarate Dioxygenase (TauD) from Escherichia coli. *Biochemistry.* **2003**, 42, 7497-7508.

25. Hoffart, L. M.; Barr, E. W.; Guyer, R. B.; Bollinger, J. M., Jr.; Krebs, C. Direct Spectroscopic Detection of a C–H Cleaving High-spin Fe(IV) Complex in a Prolyl-4-hydroxylase. *Proc. Natl. Acad. Sci. USA.* **2006**, 103, 14738-14743.

26. Galonic, D. P.; Barr, E. W.; Walsh, C. T.; Bollinger, J. M., Jr.; Krebs, C. Two Interconverting Fe(IV) Intermediates in Aliphatic Chlorination by the Halogenase CytC3. *Nat. Chem. Bio*. **2007**, 3, 113-116.

27. Matthews, M. L.; Chang, W.-c.; Layne, A. P.; Miles, L. A.; Krebs, C.; Bollinger, J. M., Jr. Direct Nitration and Azidation of Aliphatic Carbons by an Iron-dependent Halogenase. *Nat. Chem. Bio.* **2014**, 10, 209-217.

28. Vaillancourt, F. H.; Yeh, E.; Vosburg, D. A.; Garneau-Tsodikova, S.; Walsh, C. T. Nature's Inventory of Halogenation Catalysts: Oxidative Strategies Predominate. *Chem. Rev*. **2006**, 106, 3364- 3378.

29. Karlin, K.D. Metalloenzymes, Structural Motifs, and Inorganic Models. *Science*. **1993**, 261, 701-708.

30. Que, L., Jr. 60 Years of Dioxygen Activation. *J. Biol. Inorg. Chem*. **2017**, 22, 171–173.

31. Sahu, S.; Goldberg, D. P. Activation of Dioxygen by Iron and Manganese Complexes: A Heme and Nonheme Perspective. *J. Am. Chem. Soc*. **2016**, 138, 11410–11428.

32. Nam, W. Dioxygen Activation by Metalloenzymes and Models. *Acc. Chem. Res*. **2007**, 40, 465–465.

33. Guo, M.; Corona, T.; Ray, K.; Nam, W. Heme and Nonheme High-Valent Iron and Manganese Oxo Cores in Biological and Abiological Oxidation Reactions. *ACS Cent. Sci.* **2019**, 5, 13-28.

34. Groves, J. T.; Haushalter, R. C.; Nakamura, M.; Nemo, T. E.; Evans, B. J. High-Valent Iron-Porphyrin Complexes related to Peroxidase and Cytochrome P-450. *J. Am. Chem. Soc.* **1981**, 103, 2884–2886

35. Penner-Hahn, J. E.; Eble, K. S.; McMurry, T. J.; Renner, M.; Balch, A. L.; Groves, J. T.; Dawson, J. H.; Hodgson, K. O., Structural Characterization of Horseradish Peroxidase Using EXAFS Spectroscopy. Evidence for Fe=O Ligation in Compounds I and II. *J. Am. Chem. Soc*. **1986**, 108, 7819-7825.

36. Penner-Hahn, J. E.; McMurry, T.; Renner, M.; Latos-Grazynski, L.; Eble, K. S.; Davis, I. M.; Balch, A.; Groves, J. T.; Dawson, J. H.; Hodgson, K. O., X-ray Absorption Spectroscopic Studies of High Valent Iron Porphyrins. *J. Biol. Chem*. **1983**, 258, 12761-12764.

37. Chance, M.; Powers, L.; Poulos, T.; Chance, B., Cytochrome c Peroxidase Compound ES Is Identical with Horseradish Peroxidase Compound I in Iron-Ligand Distances. *Biochemistry.* **1986**, 25, 1266-1270.

38. Borovik, A. S. Bioinspired Hydrogen Bond Motifs in Ligand Design: The Role of Noncovalent Interactions in Metal Ion Mediated Activation of Dioxygen. *Acc. Chem. Res.* **2005**, 38, 54-61.

39. Shook, R. L.; Borovik, A. S. Role of the Secondary Coordination Sphere in Metal-Mediated Dioxygen Activation. *Inorg. Chem*. **2010**, 49, 3646-3660.

40. Pandey, B.; Ansari, A.; Vyas, N.; Rajarmaman, G. Structures, bonding, and reactivity of iron and manganese high-valent metal-oxo complexes: A computational investigation. *J. Chem. Sci.* **2015**, 127, 2, 343-352.

41. Shirin, Z.; Hammes, B. S.; Young, V. G.; Borovik, A. S. Hydrogen Bonding in Metal Oxo Complexes: Synthesis and Structure of a Monomeric Manganese (III)-Oxo Complex and Its Hydroxo Analogue. *J. Am. Chem. Soc.* **2000**. 122, 8, 1836-1837.

42. MacBeth, C. E.; Golombek, A. P.; Young, V. G.; Jr.; Yang, C.; Kuczera, K.; Hendrich, M. P.; Borovik, A. S. O_2 Activation by Nonheme Iron Complexes: A Monomeric Fe (III)-Oxo Complex Derived from O_2. *Science*, **2000**, 289, 938-941.

43. Gupta, R.; Borovik, A. S. Monomeric $Mn^{III/II}$ and $Fe^{III/II}$ Complexes with Hydroxo and Oxo Ligands: Probing Reactivity via O-H Bond Dissociation Energies. *J. Am. Chem. Soc*. **2003**, 125, 13234-13242.

44. Matson, E. M.; Park, Y. J.; Fout, A. R. Facile Nitrite Reduction in a Non-heme Iron System: Formation of an Iron (III)-Oxo. *J. Am. Chem. Soc.* **2014**, 136, 17398-17401.

45. Gordon, Z.; Miller, T. J.; Leahy, C. A.; Matson, E. M.; Burgess, M.; Drummond, M. J.; Popescu, C. V.; Smith, C. M.; Lord, R. L.; Rodriguez-Lopez, J.; Fout, A. R. Characterization of Terminal Iron (III)-Oxo and Iron(III)-Hydroxo Complexes Derived from O_2 Activation. *Inorg. Chem.* **2019**, 15801-15811.

46. Lee, J. L.; Ross, D. L.; Barman, S. K.; Ziller, J. W.; Borovik, A. S. C-H Bond Cleavage by Bioinspired Metal Complexes. *Inorg. Chem*. **2021**, 60, 13759-13783.

47. Ray, K.; Heims, F.; Pfaff, F. F. Terminal Oxo and Imido Transition-Metal Complexes of Groups 9-11. *Eur. J. Inorg. Chem.* **2013**, 3784-3807.

48. Vansek, P. In CRC Handbook of Chemistry & Physics. Taylor & Francis: **2010**.

49. Surendranath, Y.; Kanan, M. W.; Nocera, D. G. Mechanistic Studies of the Oxygen Evolution Reaction by a Cobalt-Phosphate Catalyst at Neutral pH. *J. Am. Chem. Soc*. **2010**, 132,16501-16509.

50. Bediako, D. K.; Lassalle-Kaiser, B.; Surendranath, Y.; Yano, J.; Yachandra, V. K.; Nocera, D. G. Structure-Activity Correlations in a Nickel-Borate Oxygen Evolution Catalyst. *J. Am. Chem. Soc*. **2012**, 134, 6801-6809.

51. Nguyen, A. I.; Ziegler, M. S.; Oña-Burgos, P.; Sturzbecher-Hohne, M.; Kim, W.; Bellone, D. E. Mechanistic Investigations of Water Oxidation by a Molecular Cobalt Oxide Analogue: Evidence for a Highly Oxidized Intermediate and Exclusive Terminal Oxo Participation. *J. Am. Chem. Soc*. **2015**, 137, 12865-12872.

52. Pierpont, A. W.; Cundari, T. R. Computational Study of Methane C-H Activation by First-Row Late Transition Metal $L_nM=E$ (M: Fe, Co, Ni) Complexes. *Inorg. Chem*. **2010**, 49, 2038-2046.

53. Yao, S.; Driess, M. Lessons from Isolable Nickel(I) Precursor Complexes for Small Molecule Activation. *Acc. Chem. Res*. **2012**, 45, 276-287.

54. Poverenov, E.; Efremenko, I.; Frenkel, A. I.; Ben-David, Y.; Shimon, L. J.; W.; Leitus, G.; Konstantinovski, L.; Martin, J. M. L.; Milstein, D. Evidence for a Terminal Pt (IV)-oxo Complex Exhibiting Diverse Reactivity. *Nature*. **2008**, 455, 1093-1097.

55. Wang, B.; Lee, Y. -M; Tcho, W.-Y.; Tussupbayev, S.; Kim, S.-T.; Kim, Y.; Seo, M. S.; Cho, K.-B.; Dede, Y.; Keegan, B. C.; Ogura, T.; Kim, S. H.; Ohta, T.; Baik, M.-H.; Ray, K.; Shearer, J.; Nam, W. Synthesis and Reactivity of a Mononuclear Non-haem Cobalt (IV)-oxo Complex. *Nat. Commun*. **2017**, 8, 14839.

56. Goertz, M. K.; Hill, E. A.; Filatov, A. S.; Anderson, J. S. Isolation of a Terminal Co (III)-Oxo Complex. *J. Am. Chem. Soc*. **2018**, 140, 13176-13180.

57. Reed, C. J.; Agapie, T. A Terminal Fe^{III}-Oxo in a Tetranuclear Cluster: Effects of Distal Metal Centers on Structure and Reactivity. *J. Am. Chem. Soc.* **2019**, 141, 24, 9479-9484.

58. Larson, V. A.; Battistella, B.; Ray, K.; Lehnert, N.; Nam, W. Iron and manganese oxo complexes, oxo wall and beyond. *Nat. Rev. Chem*. **2020**, 4, 404-419.

59. Yang, J.; Dong, H. T.; Seo, M. S.; Larson, V. A. Lee, Y.-M, Shearer, J.; Lehnert, N.; Nam, W. The Oxo-Wall Remains Intact: A Tetrahedrally Distorted Co(IV)-Oxo Complex. *J. Am. Chem. Soc.* **2021**, 143, 41, 16943-16959.

60. O'Halloran, K. P.; Zhao, C.; Ando, N. S.; Schultz, A. J.; Koetzle, T. F.; Piccoli, P. M. B.; Hedman, B.; Hodgson, K. O.; Bobyr, E.; Kirk, M. L.; Knottenbelt, S.; Depperman, E. C.; Stein, B.; Anderson, T. M.; Cao, R.; Geletii, Y. V.; Hardcastle, K. I.; Musaev, D. G.; Neiwert, W. A.; Fang, X.; Morokuma, K.; Wu, S.; Kogerler, P.; Hill, C. L. Revisting the Polyoxometalate-Based Late-Transition-Metal-Oxo Complexes: The "Oxo Wall" Stands. *Inorg. Chem.* **2012**, 51, 7025-7031.

61. Ballhausen, C. J.; Gray, H. B. The Electronic Structure of the Vanadyl Ion. *Inorg. Chem.* **1962**, 1, 111-122.

62. Winkler, J. R.; Gray, H. B. Electronic Structures of Oxo-Metal Ions. *Struc. Bond*. **2012**, 142, 17-28.

63. Gray, H. B.; Winkler, J. R. Living with Oxygen. *Acc. Chem. Res.* **2018**, 51,8, 1850-1857.

64. Efremenko, I.; Poverenov, E.; Martin, J. M. L.; Milstein, D. DFT Study of the Structure and Reactivity of the Terminal Pt (IV)-Oxo Complex Bearing No Electron-Withdrawing Ligands. J. *Am. Chem. Soc*. **2010**, 132,14886-14900.

65. Goetz, M. K.; Anderson, J. S. Experimental Evidence for pKa-Driven Asynchronicity in C–H Activation by a Terminal Co (III)–Oxo Complex. *J. Am. Chem. Soc*. **2019**, 141, 4051-4062.

66. Fisher, K. J.; Feuer, M. L.; Lant, H. M. C.; Mercado, B. Q.; Crabtree, R. H.; Brudvig, G. W. Concerted Proton-electron Transfer Oxidation of Phenols and Hydrocarbons by a High-valent Nickel Complex. *Chem. Sci*. **2020**, 11, 1683-1690.

67. Corona, T.; Draksharapu, A.; Padamati, S. K.; Gamba, I.; Martin-Diaconescu, V.; Acuña-Pareś, F.; Browne, W. R.; Company, A. Rapid Hydrogen and Oxygen Atom Transfer by a High-Valent Nickel–Oxygen Species. *J. Am. Chem. Soc.* **2016**, 138, 12987-12996.

68. Pirovano, P.; Farquhar, E. R.; Swart, M.; Fitzpatrick, A. J.; Morgan, G. G.; McDonald, A. R. Characterizaton and Reactivity of a Terminal Nickel (III)-Oxygen Adduct. *Chem. Eur. J.* **2015**, 21, 3785-3790.

69. Pirovano, P.; Farquhar, E. R.; Swart, M.; McDonald, A. R. Tuning the Reactivity of Terminal Nickel(III)-Oxygen Adducts for C-H Bond Activation. *J. Am. Chem. Soc*. **2016**, 138, 14362-14370.

70. Pirovano, P.; Twamley, B.; McDonald, A. R. Modulation of Nickel Pyridinedicarboxamidate Complexes to Explore the Properties of High-valent Oxidants. *Chem. Eur. J.* **2018**, 24, 20, 5238-5245.

71. Mondal, P.; Pirovano, P.; Das, A.; Farquhar, E. R.; McDonald, A. R. Hydrogen Atom Transfer by a High-Valent Nickel-Chloride Complex. *J. Am. Chem. Soc*. **2018**, 140, 1834-1841.

72. Mondal, P.; Lovisar, M.; Twamley, B.; McDonald, A. R. Fast Hydrogen Atom Transfer by a High-Valent Nickel-Chloride Complex *Angew. Chem. Int. Ed.* **2020**, 59, 13044-13050.

73. Mondal, P.; Lovisari, M.; Twamley, D.; McDonald. A. R. Fast Hydrocarbon Oxidation by a High-Valent Nickel-Fluoride Complex. *Angew. Chem. Int. Ed.* **2020**, 59, 31, 13144-13150.

74. Unjaroen, D.l Gericke, R.; Lovisari, M.; Nelis, D.; Mondal, P.; Pirovano, P.; Twamley, B.; Farquhar, E. R.; McDonald, A. R. High Valent d^7 Ni^{III} versus d^8 Cu^{III} Oxidants in PCET. *Inorg. Chem.* **2019**, 58, 16838-16848.

75. Donoghue, P. J.; Tehranchi, K.; Cramer, C. J.; Sarangi, R.; Solomon, E. I.; Tolman, W. B. Rapid C-H Bond Activation by a Monocopper(III)-Hydroxide Complex. *J. Am. Chem. Soc*. **2011**, 133, 17602-17605.

76. Dhar, D.; Yee, G. M.; Spaeth, A. D.; Boyce, D. W.; Zhang, H.; Dereli, B.; Cramer, C. J.; Tolman, W. B. Perturbing the Copper(III)-Hydroxide Unit through Ligand Structural Variation. *J. Am. Chem. Soc.* **2016**, 138, 356-368.

77. Dhar, D.; Tolman, W. B. Hydrogen Atom Abstraction from Hydrocarbons by a Copper(III)-Hydroxide Complex. *J. Am. Chem. Soc.* **2015**, 137, 1322-1329.

78. Bower, J. K.; Cypcar, A. D.; Henriquez, B.; Stieber, S. C. E.; Zhang, S. C(sp^3)-H Fluorination with Copper(II)/(III) Redox Couple. *J. Am. Chem. Soc.* **2020**, 142, 8514-8521.

79. Krishnan, V. M.; Shopov, Bouchey, C. J.; Bailey, W. D.; Parveen, R.; Vlaisavljevich, B.; Tolman, W. B. Structural Characterization of the [CuOR]$^{2+}$ Core. *J. Am. Chem. Soc.* **2021**, 143, 3295-3299.

80. Wu, T.; MacMillan, S. N.; Rajabimoghadam, K. ; Siegler, M. A.; Lancaster, K. M.; Garcia-Bosch, I.; Structure, Spectroscopy, and Reactivity of a Mononuclear Copper Hydroxide Complex, in Three Molecular Oxidation States. *J. Am. Chem. Soc.* **2020**, 142, 12265-12276.

81. Andris, E.; Navratil, R.; Jasik, J.; Srnec, M.; Rodriguez, M. Costas, M, Roithova, J.; M-O Bonding Beyond the Oxo Wall: Spectroscopy and Reactivity of Cobalt(III)-Oxyl and Cobalt(III)-Oxo Complexes. *Angew. Chem. Int. Ed.* **2019**, 58, 9619-9624.

82. Hong, S.; Pfaff, F. F.; Kwon, E.; Wang, Y.; Seo, M.-S.; Bill, E.; Ray, K.; Nam, W. Spectroscopic Capture and Reactivity of a Low-Spin Cobalt(IV)-Oxo Complex Stabilized by Binding Redox-Inactive Metal Ions. *Angew. Chem., Int. Ed*. **2014**, 53, 10403–10407.

83. Huang, D.; Holm, R. H. Reactions of the Terminal Ni^{II}-OH Group in Substitution and Electrophilic Reactions with Carbon Dioxide and Other Substrates: Structural Definition of fgoldb4693-4701.

84. Huang, D.; Makhlynets, O. V.; Tan, L. L.; Lee, S. C.; Rybak-Akimova, E. V.; Holm, R. H., Fast Carbon Dioxide Fixation by 2,6-Pyridinedicarboxamidatonickel(II)-hydroxide Complexes: Influence of Changes in Reactive Site Environment on Reaction Rates. *Inorg. Chem*. **2011**, 50, 10070-10081.

85. DiFranco, S. A.; Maciulis, N. A. ; Staples, R. J. ; Batric, R. J. ; Odom, A. L. Evaluation of Donor and Steric Properties of Anionic Ligands on High Valent Transition Metals. *Inorg. Chem.* **2012**, 51, 2, 1187-1200.

86. Lacy, D. C.; Gupta, R.; Stone, K. L.; Greaves, J.; Ziller, J. W.; Hendrich, M. P.; Borovik, A. S., Formation, Structure, and EPR Detection of a High Spin FeIV-Oxo Species Derived from Either an FeIII-Oxo or FeIII-OH Complex. *J. Am. Chem. Soc*. **2010**, 132, 12188-12190.

87. Bigi, J. P.; Harman, W. H.; Lassalle-Kaiser, B.; Robles, D. M.; Stich, T. A.; Yano, J.; Britt, R. D.; Chang, C. J., A High-Spin Iron(IV)-Oxo Complex Supported by a Trigonal Nonheme Pyrrolide Platform. *J. Am. Chem. Soc*. **2012**, 134, 1536-1542.

88. England, J.; Guo, Y.; Farquhar, E. R.; Young Jr., V. G.; Münck, E.; Que, L., Jr., The Crystal Structure of a High-Spin Oxoiron(IV) Complex and Characterization of Its Self-Decay Pathway. *J. Am. Chem. Soc*. **2010**, 132, 8635-8644.

89. Tehranchi, J.; Donoghue, P. J. ; Cramer, C. J. ; Tolman, W. B. Reactivity of (Dicarboxamid)M^{II}-OH (M = Cu, Ni) Complexes – Reaction with Acetonitrile to Yield M^{II}-Cyanomethides. *Eur. J. Inorg. Chem*. **2013**, 4077-4084.

90. Hana, F.; Lough, A. J.; Lavoie, G. G. Coordinately- and electronically- unsaturated square plane cobalt(III) complexes of a pyridine dianionic pincer ligand. *Dalton Trans*. **2017**, 46, 16228-16235.

91. Kwon, Y.M.; Lee, Y.; Evenson, G. E.; Jackson, T. A.; Wang, D. "Crystal Structure and C-H Bond Cleaving Reactivity of a Mononuclear Co^{IV}-dinitrate Complex." *J. Am. Chem. Soc*. **2020**, 142, 31, 13435-13441. ***Featured in JACS Spotlights*** (*J. Am. Chem. Soc.* **2020**, 142, 33, 14005–14006).

92. Small, B. L.; Brookhart, M. Polymerization of Proplene by a New Generation of Iron Catalysts: Mechanisms of Chain Initiation, Propagation, and Termination. *Macromolecules*, **1999**, 32,7, 2120-2130.

93. Will, S.; Lex, J.; Vogel, E.; Adamian, V. A.; Caemelbecke, E. V.; Kadish, K. M. Synthesis, Characterization, and Electrochemistry of σ-Bonded Cobalt Corroles in High Oxidation States. *Inorg. Chem*. **1996**, 35, 5577-5583.

94. Carpenter, G. B.; Clark, G. S.; Rieger, A. L.; Rieger, P. H.; Sweigart, D. A. Dithiolenes Revisited: An Electron Spin Resonance Study of some Five-coordinate Cobalt Complexes and the Crystal-Structures of [Co{S2C2(CF3)2}2{P(OPh)3}] and [Co{S2C2(CF3)2}2(PPh3)]. *J. Chem. Soc. Dalton Trans.* **1994**, 20, 2903-2910.

95. Adamian, V. A.; D'Souza, F.; Licoccia, S.; Di Vona, M. L.; Tassoni, E.; Paolesse, R.; Boschi, T.; Kadish, K. M. Synthesis, Characterization, and Electrochemical Behavior of (5,10,15-Tri-X-phenyl-2,3,7,8, l2,13,17,18-octamethylcorrolato)cobalt(III) Triphenylphosphine Complexes, Where X = p-OCH3, p-CH3, p-Cl, m-Cl, o-Cl, m-F, o-F, or H. *Inorg. Chem*. **1995**, 34, 532–540.

96. Harmer, J.; Van Doorslaer, S.; Gromov, I.; Broring, M.; Jeschke, G.; Schweiger, A. A Pulse EPR and ENDOR Investigation of the Electronic Structure of a c-Carbon-Bonded Cobalt(IV) Corrole. *J. Phys. Chem. B*. **2002**, 106, 2801–2811.

97. Goldsmith, C. R.; Jonas, R. T.; Stack, T. D. P. C-H Bond Activation by a Ferric Methoxide Complex: Modeling the Rate-Determining Step in the Mechanism of Lipoxygenase. *J. Am. Chem. Soc.* **2002**, *124*, 83-96.

98. Gardner, K. A.; Kuehnert, L. L.; Mayer, J. M. Hydrogen Atom Abstraction by Permanganate: Oxidations of Arylalkanes in Organic Solvents. *Inorg. Chem.* **1997**, *36*, 2069-2078.

99. Leto, D. F.; Ingram, R.; Day, V. W.; Jackson, T. A. Spectroscopic Properties and Reactivity of a Mononuclear Oxomanganese(IV) Complex. *Chem. Commun.* **2013**, *49*, 5378-5380.

100. Wu, X.; Seo, M. S.; Davis, K. M.; Lee, Y.-M.; Chen, J.; Cho, K.-B.; Pushkar, Y. N.; Nam, W. A Highly Reactive Mononuclear Non-Heme Manganese(IV)-Oxo Complex That Can Activate the Strong C-H Bonds of Alkanes. *J. Am. Chem. Soc.* **2011**, *133*, 20088-20091.

101. Massie, A. A.; Sinha, A.; Parham, J. D.; Nordlander, E.; Jackson, T. A. Relationship between Hydrogen-Atom Transfer Driving Force and Reaction Rates for an Oxomanganese(IV) Adduct. *Inorg. Chem.* **2018**, *57*, 8253-8263.

102. Sawant, S. C.; Wu, X.; Cho, J.; Cho, K.-B.; Kim, S. H.; Seo, M. S.; Lee, Y.-M.; Kubo, M.; Ogura, T.; Shaik, S.; Nam, W. Water as an Oxygen Source: Synthesis, Characterization, and Reactivity Studies of a Mononuclear Nonheme Manganese(IV) Oxo Complex. *Angew. Chem. Int. Ed.* **2010**, *49*, 8190-8194.

103. Kaizer, J.; Klinker, E. J.; Oh, N. Y.; Rohde, J.-U.; Song, W. J.; Stubna, A.; Kim, J.; Münck, E.; Nam, W.; Que, L., Jr. Nonheme Fe[IV]O Complexes That Can Oxidize the C-H Bonds of Cyclohexane at Room Temperature. *J. Am. Chem. Soc.* **2004**, *126*, 472-473.

104. Seo, M. S.; Kim, N. H.; Cho, K.-B.; So, J. E.; Park, S. K.; Clemancey, M.; Garcia-Serres, R.; Latour, J.-M.; Shaik, S.; Nam, W. A Mononuclear Nonheme Iron(IV)-oxo Complex which is More Reactive than Cytochrome P450 Model Compound I. *Chem. Sci.* **2011**, *2*, 1039-1045.

105. Bryant, J. R.; Mayer, J. M. Oxidation of C-H Bonds by [(bpy)$_2$(py)Ru[IV]O]$^{2+}$ Occurs by Hydrogen Atom Abstraction. *J. Am. Chem. Soc.* **2003**, *125*, 10351-10361.

106. Yin, G.; Danby, A. M.; Kitko, D.; Carter, J. D.; Scheper, W. M.; Busch, D. H. Understanding the Selectivity of a Moderate Oxidation Catalyst: Hydrogen Abstraction by a Fully Characterized, Activated Catalyst, the Robust Dihydroxo Manganese(IV) Complex of a Bridged Cyclam. *J. Am. Chem. Soc.* **2007**, *129*, 1512-1513.

107. Goldsmith, C. R.; Cole, A. P.; Stack, T. D. P. C-H Activation by a Mononuclear Manganese(III) Hydroxide Complex: Synthesis and Characterization of a Manganese-Lipoxygenase Mimic? *J. Am. Chem. Soc.* **2005**, *127*, 9904-9912.

108. Goldsmith, C. R.; Stack, T. D. P. Hydrogen Atom Abstraction by a Mononuclear Ferric Hydroxide Complex: Insights into the Reactivity of Lipoxygenase. *Inorg. Chem.* **2006**, *45*, 6048-6055.

109. Corona, T.; Draksharapu, A.; Padamati, S. K.; Gamba, I.; Martin-Diaconescu, V.; Acuña-Pareś, F.; Browne, W. R.; Company, A. Rapid Hydrogen and Oxygen Atom Transfer by a High-Valent Nickel–Oxygen Species. *J. Am. Chem. Soc.* **2016**, *138*, 12987-12996.

110. Unjaroen, D.; Gericke, R.; Lovisari, M.; Nelis, D.; Mondal, P.; Pirovano, P.; Twamley, B.; Farquhar, E. R.; McDonald, A. R. High-Valent d^7 Ni^{III} versus d^8 Cu^{III} Oxidants in PCET. *Inorg. Chem.* **2019**, *58*, 16838-16848.

111. Eckert, F.; Leito, I.; Kaljurand, I.; Kutt, A.; Klamt, A.; Diedenhofen, M. Prediction of Acidity in Acetonitrile Solution with COSMO-RS. J. Comput. Chem. **2009**, 30, 799–810.

112. Muckerman, J. T.; Skone, J. H.; Ning, M.; Wasada-Tsutsui, Y. Toward the Accurate Calculation of pKa Values in Water and Acetonitrile. Biochim. Biophys. Acta, Bioenerg. **2013**, 1827, 882–891.

113. Mayer, J. M. Understanding Hydrogen Atom Transfer: From Bond Strengths to Marcus Theory. *Acc. Chem. Res.* **2011**, 44, 36–46.

114. Roth, J. P.; Yoder, J. C.; Won, T.-J.; Mayer, J. M. Application of the Marcus Cross Relation to Hydrogen Atom Transfer Reactions. *Science*. **2001**, 294, 2524–2526.

115. Huang, X.; Bergsten, T. M.; Groves, J. T. Manganese-Catalyzed Late-Stage Aliphatic C–H Azidation. *J. Am. Chem. Soc.* **2015**, 137, 5300-5303.

116. Liu, W.; Huang, X.; Cheng, M.-J.; Nielsen, R. J.; Goddard, W. A., III; Groves, J. T. Oxidative Aliphatic C-H Fluorination with Fluoride Ion Catalyzed by a Manganese Porphyrin. *Science* **2012**, 337, 1322-1325

117. Camasso, N. M; Sanford, M. S. Design, Synthesis, and Carbon-heteroatom Coupling Reactions of Organometallic Nickel(IV) Complexes. *Science*. **2015**, 347, 1218-1220.

118. Bour, J. R.; Ferguson, D. M.; McClain, E. J.; Kampf, J. W.; Sanford, M. S. Connecting organometallic Ni(III) and Ni(IV): Reactions of Carbon-Centered Radicals with High-Valent Organonickel Complexes. *J. Am. Chem. Soc.* **2019**, 141, 22, 8914-8920.

119. Meucci, E. A.; Nguyen, S. N. ; Camasso, N. M. ; Chong, E. ; Ariafard, A. ; Canty, A. J.; Sanford, M. S. Nickel(IV)-Catalyzed C-H Trifluoromethylation of (Hetero)arenes. *J. Am. Chem. Soc.* **2019**, 141, 32, 12872-12879.

120. Nebra, N. High-Valent Ni^{III} and Ni^{IV} Species Relevant to C-C and C-Heteroatom Cross-Coupling Reactions: State of the Art. *Molecules*, **2020**, 25, 5, 1141-1172.

121. Darcy, J. W.; Kolmar, S. S.; Mayer, J. M. Transition State Asymmetry in C–H Bond Cleavage by Proton- Coupled Electron Transfer. *J. Am. Chem. Soc*. **2019**, 141, 10777-10787.

122. Costentin, C.; Savéant, J.-M. Hydrogen and Proton Exchange at Carbon. Imbalanced Transition State and Mechanism Crossover. *Chem. Sci*. **2020**, 11, 1006-1010

123. Sheldrick, G. M. (1996). SADABS: Area Detector Absorption Correction; University of Göttingen, Germany.

124. Dolomanov, O.V.; Bourhis, L.J.; Gildea, R.J.; Howard, J.A.K.; Puschmann, H., (2009). J. Appl. Cryst., 42, 339-341.

125. Sheldrick, G. M. (2015). *Acta Cryst.* A71, 3-8.

126. Sheldrick, G. M. (2015). *Acta Cryst.* C71, 3-8.

127. Bruker (2016). APEX3. Bruker AXS Inc., Madison, Wisconsin, USA.

128. Sheldrick, G.M. (2008). Acta Cryst. A64, 112-122.